Parameter estimation and the statistics of nonlinear cosmic fields

Peter I R Watts

Doctor of Philosophy
The University of Edinburgh
2000

This thesis is my own composition except where indicated in the text.

March 27, 2001

Acknowledgements

There's no question that my time in Edinburgh has been among the most enjoyable and interesting of my life. This is in no small part due to all the wonderful people I've had the pleasure of working, learning and playing with during these past three years. I owe everyone a huge debt of thanks.

Firstly endless thanks go to my supervisor, Andy Taylor – a man of no small brain. In some ways mere thanks seem strangely inappropriate after all the time and energy Andy has given to me over the years. His boundless enthusiasm and heroic sense of humor always made everything seem ok – no matter how messy the sums got. To always be there for every problem, to always have a ready answer, and to never once make me feel like I should have known better takes a special kind of talent and patience.

Of the permanent members of staff at the IfA special thanks must also go to my second supervisor Alan Heavens and to Peter Brand and John Peacock for much support, encouragement and inspiration as and where frequently needed. An extra thank-you also to Peter and co-conspirator Sabino Mattarrese for reading through this thesis, grilling me until well done during my viva and *still* passing me.

A veritable mountain of gratitude is also owed to Liz Gibson, the departmental guardian angel. Without Liz I'm sure my PhD, if not the entire IfA, would have collapsed in a heap of disorder and chaos. Liz, I salute you.

A host of people have contributed in their own unique ways to the special atmosphere at the IfA. Notably the postdocs: Eelco (eater of the worlds pinkest sandwiches), Omar, Phil, Marak, Will (S) and Will (P); and the students (old and new): Pauli, Knoxy, Matt, Ross, Elese, Sujata, James, Ali, Michael, Susie, Rachel, Andy and Chris. You're all stars and I'm going to miss you.

There are a few folks who deserve an extra mention for services above and beyond

the call of duty: my three computer gurus – Helen, Elspeth and Meg – without whom I would undoubtedly still be stuck in an infinite *DO* loop; Simon Dye, one time flatmate, academic elder brother and pressure cooker virtuoso; and Alex Adam who, shortly after completion of my thesis and scarce minutes before the closure of faculty office, found me wrestling hopelessly with a binding machine far more complicated than I. Alex's steady hand and cool head saved the day.

Finally at the IfA are the Famous Four – Rob, Kenny, Scog and Lou – without whom it would have all been so very different. You're the best, guys, what more can I say?

Outside of work a huge thank-you goes to my Dad for his continual support – both financial and moral. From selflessly driving me and my broken foot around Edinburgh looking for flats, to the endless bailings out when the money got tight, he has always been there – thanks.

Lastly, but by no means leastly, I'd like to thank Jo for more than I could ever possibly write...

Abstract

The large scale distribution of matter in the universe contains valuable information about fundamental cosmological parameters, the properties of dark matter and the formation processes of galaxies. The best hope of retrieving this information lies in providing a statistical description of the matter distribution that may be used for comparing models with observation. Unfortunately much of the important information lies on scales below which nonlinear gravitational effects have taken hold, complicating both models and statistics considerably. This thesis deals with the distribution of matter – mass and galaxies – on such scales. The aim is to develop new statistical tools that make use of the nonlinear evolution for the purposes of constraining cosmological models.

A new derivation for the 1-point probability distribution function (PDF) for density inhomogeneities is presented first. The calculation is based upon an exact statistical treatment, using the Chapman-Kolmogorov equation and second order Eulerian perturbation theory to propagate the initial density field into the nonlinear regime. The analysis yields the generating function for moments, allowing for a straightforward derivation of the skewness. A new dependance upon the perturbation spectrum is found for the skewness at second order. The results of the analysis are compared against other methods for deriving the 1-point PDF and against data from numerical N-body simulations. Good agreement is found in both cases.

The 1-point PDF for galaxies is derived next, taking into account nonlinear biasing of the density field and the distorting effects associated with working in redshift space. Once again perturbation theory is used to evolve the density field into the nonlinear regime and the Chapman-Kolmogorov equation to propagate the initial probabilities. Transformation of the dark matter density to a biased galaxy distribution is done through an Eulerian biasing prescription, expanding the nonlinear bias function to second order. An advantage of the Chapman-

Kolmogorov approach is the natural way that different initial conditions and biasing models may be incorporated. It is shown that the method is general enough to allow a non-deterministic (hidden variable) bias. The dependance on cosmological parameters of the evolution of the galaxy 1-point PDF is demonstrated and a method for differentiating between degenerate models in linear theory is presented. A new derivation of the skewness for a biased density field in redshift space is also given and shown to depend significantly on the density and bias parameters. The results are compared favourably with those of numerical simulations.

Finally a new, general formalism for analysing parameter information from non-Gaussian cosmic fields is developed. The method is general enough for application to a range of problems including the measurement of parameters from galaxy redshift surveys, weak lensing surveys and velocity field surveys. It may also be used to test for non-Gaussianity in the Cosmic Microwave Background. Generalising maximum likelihood analysis to second order, the non-Gaussian Fisher information matrix is derived and the detailed shapes of likelihood surfaces in parameter space are explored via a parameter entropy function. Concentrating on non-Gaussianity due to nonlinear evolution under gravity, the generalised Fisher analysis is applied to a model of a Galaxy redshift survey, including the effects of biasing, redshift space distortions and shot noise. Incorporating second order moments into the parameter estimation is found to have a large effect, breaking all of the degeneracies between parameters. The results indicate that using nonlinear likelihood analysis may yield parameter uncertainties around the few percent level from forthcoming large galaxy redshift surveys.

Contents

List of Figures

Chapter 1

Introduction

1.1 Big Bang cosmology

What has become known as the standard model of cosmology derives largely from two fundamental observations: that most galaxies appear to be receding from us and that the distribution of distant objects on the sky is isotropic.

The first observation was made following the work of Slipher and Hubble in 1929, radically changing the notion of a static universe beloved of 19th and early 20th century cosmologists. The bold connection between the velocity of galaxies and their distance was made by Hubble (1929). Using the Doppler shifting of lines in the spectra of distant galaxies in conjunction with distance estimates based on the observation of Cephied variable stars in the galaxies themselves, Hubble noted that the most distant galaxies were receding from us with velocities that were linearly related to their distance,

$$v = H_0 \, d. \tag{1.1}$$

This fundamental discovery is discussed in more detail later on. For now we note that Hubble's linear relationship fitted in precisely with the concept of a uniformly expanding universe which had been proposed by Lemaître (1927). From the early 1930s the expanding universe model had become widely accepted.

The second observation brings us to the starting point for the development of physical cosmology in the modern sense of the word. The isotropy of the universe at large has now been verified by numerous observations at a variety of wavelengths. Perhaps the most remarkable measurement comes from the Cosmic Microwave Background (CMB) radiation, discovered by Penzias & Wilson (1965)

and discussed in more detail in §1.1.9. Once the effects of local motion and foreground sources are taken into account, the microwave sky is seen to be isotropic to better than 1 part in 10^5 over all angular scales.

1.1.1 The cosmological principle

The observation that the universe, as viewed from earth, appears isotropic, can be combined with a rather common-sense philosophical statement in order to set the foundations upon which we will construct a consistent cosmological picture. The philosophy goes that we, as observers, do not reside in a special part of the Universe; all observers must see the universe much as we see it, leaving aside local irregularities. This reasoning is a natural extension of the Copernican Principle that states that the Earth does not lie at the centre of the Solar system. The result is a simplicity principle termed the Cosmological Principle:

> The Universe is homogeneous throughout space and isotropic about every point.

Obviously this cannot be true on every scale; gravitation and other processes make the universe look clumpy on scales up to the size of galaxy clusters and beyond. What is meant in the Cosmological Principle is that the global properties of the Universe must be described within the geometrical confines of a homogeneous and isotropic space.

1.1.2 The Robertson-Walker metric

The tools we use to construct a cosmological model are those of general relativity. The workplace is a Riemannian manifold whose metric $g_{\nu\mu}$ defines the infinitesimal line element by

$$ds^2 = g_{\nu\mu} dx^\nu dx^\mu. \tag{1.2}$$

The x^ν are 4-vectors $x^\nu = x(t, x^\alpha)$, where the x^α are 3-dimensional space coordinates and t labels time.

For a universe in which the Cosmological Principle applies, we are able to use simple geometrical arguments to deduce the form of the metric. Events in the

universe are witnessed by a set of *fundamental observers*. The fundamental observers see local isotropy and record *cosmic time*. They are said to be *comoving* with the expansion. Cosmic time labels a set of space-like hypersurfaces for which the 3-dimensional spatial metric $\gamma_{\alpha\beta}$, is identical at all points. In this way we look for a metric that gives a line element of the form

$$ds^2 = c^2dt^2 - \gamma_{\alpha\beta}dx^\alpha dx^\beta. \tag{1.3}$$

One finds that the Robertson-Walker (RW) metric is the most general that satisfies the Einstein field equations in a homogeneous expanding universe, see for example Weinberg (1972). The line element for the RW metric is

$$ds^2 = c^2dt^2 - R^2(t)\left[\frac{dx^2}{1-Kx^2} + x^2(d\theta^2 + \sin^2\theta d\phi^2)\right]. \tag{1.4}$$

The spatial terms arise from isotropy on the 3-dimensional space-like hypersurfaces. The hypersurfaces may possess either positive, negative or zero curvature. The curvature is quantified through K, which may take the values $+1$, -1 or 0 accordingly. The spherical coordinates x, θ and ϕ are dimensionless, comoving quantities, physical scale and dimension are put in by the time dependant factor $R(t)$. The x coordinate is related to the comoving scale of objects perpendicular to great circles on the 3-surfaces. The RW can be written in terms of the comoving, dimensionless geodesic distance r, *i.e.* the distance along a great circle on the 3-surface from observer to source

$$ds^2 = c^2dt^2 - R^2(t)\left[dr^2 + S_k^2(r)(d\theta^2 + \sin^2\theta d\phi^2)\right]. \tag{1.5}$$

In this case the curvature is parameterised by the function $S_k(r)$ which takes the form

$$\begin{aligned} S_{+1}(r) &= \sin r \\ S_{-1}(r) &= \sinh r \\ S_0(r) &= r. \end{aligned} \tag{1.6}$$

The geodesic displacement is related to x via $x = S_k(r)$. Of final note in this section is the definition of the RW metric in terms of the dimensionless scale factor which we shall refer to later,

$$a(t) = \frac{R(t)}{R(t_0)}, \tag{1.7}$$

where t_0 labels the present epoch and $a(t_0) = 1$. With this parameter

$$ds^2 = c^2dt^2 - a^2(t)\left[\frac{dx^2}{1-Kx^2} + x^2(d\theta^2 + \sin^2\theta d\phi^2)\right] \tag{1.8}$$

in analogy with equation (1.4).

1.1.3 Expansion & redshift

Expansion

The proper distance d, between two points O and A can be calculated from the RW metric. We assume that the distance is measured by a set of linked rulers between O and A so that an instantaneous measurement may be made at time t. Considering only the radial displacement ($d\theta = d\phi = 0$), one obtains from equation (1.4)

$$d = \int_0^x R(t)\frac{dx'}{\sqrt{1-Kx'^2}} = R(t)f_k(x), \tag{1.9}$$

where $f_k(x)$ is a simple function of x that will depend upon the curvature.

Due to the expansion of the universe, the object at A will appear to have a velocity v, according to a fundamental observer at O, and vice versa. The velocity can be calculated simply by

$$v = \frac{d}{dt}R(t)\, f_k(x) = \frac{\dot{R}}{R}d \tag{1.10}$$

where a dot denotes differentiation with respect to time. This result is Hubble's Law, where the *Hubble parameter* quantifies the expansion and is defined by

$$H(t) = \frac{\dot{R}}{R} \equiv \frac{\dot{a}}{a}. \tag{1.11}$$

The present day value of the Hubble Parameter, $H(t_0) \equiv H_0$, has still not been measured consistently to high precision, its determination remains one of the central goals in cosmology. Hubble's original estimate was $500\,\mathrm{km\,s^{-1}\,Mpc^{-1}}$, in typical astronomer's units, although modern day observations put the value down at more like $50-100\,\mathrm{km\,s^{-1}\,Mpc^{-1}}$. For a recent compilation of measurements see Mould *et al.* (2000) and references therein, who quote $H_0 = 71 \pm 6\,\mathrm{km\,s^{-1}\,Mpc^{-1}}$. Uncertainty in the Hubble parameter is parameterised by a quantity h, such that

$$H_0 = 100\,h\,\mathrm{km\,s^{-1}\,Mpc^{-1}}. \tag{1.12}$$

Redshift

Waves emitted from objects in motion will be compressed or expanded by the Doppler shift. The degree of shifting is denoted by

$$z = \frac{\lambda_o}{\lambda_e} - 1, \tag{1.13}$$

where the subscripts o and e label the wavelength in the observer and emitter's rest frame respectively. A positive z denotes redshift (broadening of waves) and a negative z denotes blueshift (compressing of waves). Due to the Hubble expansion, waves sent out by fundamental observers and measured by other fundamental observers will be Doppler redshifted. This *cosmological* redshift is readily measurable in galaxies from the positions of transition lines in their spectra, it subsequently provides a deep connection between observation and the expansion history of the Universe. The relationship can be calculated from the RW metric.

Consider a pulse of light of duration Δt_e emitted from a fundamental observer at time t_e. The pulse is recorded at a time t_o by another fundamental observer who measures its duration to be Δt_o. Since photons travel along null geodesics ($ds^2 = 0$), we can write down an expression for the photon's path length for the start and end of the pulse respectively

$$\begin{aligned} \int_{t_e}^{t_o} \frac{c\,dt}{R(t)} &= \int_0^x \frac{dx'}{\sqrt{1 - Kx'^2}} \\ \int_{t_e+\Delta t_e}^{t_o+\Delta t_o} \frac{c\,dt}{R(t)} &= \int_0^x \frac{dx'}{\sqrt{1 - Kx'^2}}. \end{aligned} \tag{1.14}$$

Since the RHS of equation (1.14) is a comoving displacement, it will be the same for photons at both the start and end of the pulse. If the pulse is quite short in duration, equations (1.14) indicate

$$\frac{\Delta t_o}{R(t_o)} = \frac{\Delta t_e}{R(t_e)}. \tag{1.15}$$

Hence the redshifting of the light pulse from t_e to t_o will be

$$z = \frac{R(t_e)}{R(t_o)} - 1, \tag{1.16}$$

where we have let $\Delta t = 1/\nu$, with ν the frequency of the light. To put this in a more useful way, the dimensionless expansion factor at the epoch of redshift z is

$$a(t_e) = (1 + z)^{-1}. \tag{1.17}$$

Cosmological horizons

The particle horizon R_{PH}, defines the scale over which causal processes can occur in the Universe. Causal contact is established by the exchange of light signals. The proper distance travelled by a light ray since $t = 0$ is given by

$$R_{PH} = a(t) \int_0^t \frac{c\, dt'}{a(t')}. \tag{1.18}$$

The Hubble radius (or horizon) is defined as the proper distance at which fundamental observers see other fundamental observers recede at the speed of light

$$R_H = \frac{c}{H(t)}. \tag{1.19}$$

The Hubble radius defines the extent of the visible universe at a given time. For most cases this corresponds roughly to the particle horizon. However, the crucial difference is that the particle horizon takes account of the past history of the expansion. Once inside the particle horizon it is not possible to leave; even if two points currently lie at a distance $r > R_H$, if they were somehow once in causal contact then they will still remain within each others particle horizon.

1.1.4 The Friedmann equations

The Friedmann equations make a remarkable link between the geometry of the universe and its energy content. They were discovered by Friedmann (1922), although were not widely recognised until the expansion of the universe was deduced by the work of Slipher and Hubble (1929). The formal accreditation of the expanding universe model was Lemaître (1927), though this was probably largely due to the endorsements of Eddington (1930), de Sitter (1930) and Eddington (1931). The equations follow from Einstein's field equations

$$R_{\nu\mu} - \frac{1}{2} g_{\nu\mu} R = \frac{8\pi G}{c^4} T_{\nu\mu}, \tag{1.20}$$

which make the deep connection between space time curvature and energy density. Here $R_{\nu\mu}$ and R are the Ricci tensor and scalar and $T_{\nu\mu}$ is the energy-momentum tensor. For cosmological applications the most suitable form for $T_{\nu\mu}$ is that for a perfect fluid

$$T_{\nu\mu} = (p + \rho c^2) U_\nu U_\mu - p g_{\nu\mu}, \tag{1.21}$$

where p is the pressure, ρ is the density and U_μ is the fluid 4-velocity. Substitution of this into equations (1.20) with the RW metric, eventually yields the Friedmann equations for the scale factor (these are written in terms of the dimensionless scale factor, $a(t)$ – equation (1.7) – though using $R(t)$ would be equivalent)

$$\frac{\ddot{a}}{a} = -\frac{4\pi G}{3}\left(\rho + 3\frac{p}{c^2}\right) \tag{1.22}$$

$$\left(\frac{\dot{a}}{a}\right)^2 = H^2 = \frac{8\pi G}{3}\rho - \frac{Kc^2}{a^2}. \tag{1.23}$$

These equations are not independent; (1.23) can be derived from (1.22) given that the expansion of the universe is adiabatic. This is implied from homogeneity since the the amount of heat flowing into any volume da^3 must be equal to that flowing out.

The relation between the geometry and energy content of the universe is nicely quantified by equation (1.23). We note that there must be a critical density ρ_c, such that the curvature term K, is identically zero,

$$\rho_c = \frac{3H^2}{8\pi G}. \tag{1.24}$$

This is of such fundamental importance that we are led to define the density parameter Ω, as the ratio of the actual density to ρ_c

$$\Omega = \frac{\rho}{\rho_c} = \frac{8\pi G\rho}{3H^2}. \tag{1.25}$$

If $\Omega < 1$ then the curvature term is negative, whereas if $\Omega > 1$ the curvature is positive. The zero curvature case obviously comes when $\Omega = 1$. Determination of the present day value of the density parameter and its components (see §1.1.5) is one of the classic problems in cosmology.

1.1.5 Energy content

The energy density ρ has three dominant components: non-relativistic matter or dust, which contributes ρ_m; radiation and relativistic matter, giving ρ_r; and a vacuum energy, which provides ρ_v. The first two components are an obvious inclusion, the third has become a popular inclusion of recent years.

The vacuum contribution originated from the so called cosmological constant term in Einstein's field equations, circa 1917. Einstein modified his original equations

in order to admit a static solution for the evolution of the scale factor. The cosmological constant was manifest as an extra curvature term on the LHS of equation (1.20), $\Lambda g_{\nu\mu}$. The term was quickly dropped when Hubble's measurement of the recession of galaxies proved the expansion of the universe beyond reasonable doubt (although see Bondi & Gold, 1948; Hoyle, 1948). But once awakened, the cosmological constant proved to be remarkably difficult to put down, rearing up at several points in the past 60 years to (wrongly) explain various unexpected observations.

Most significantly, particle theorists noted that the effect of the Λ term in the field equations of general relativity was similar to the effect of a vacuum energy. The existence of such an entity, associated with the zero-point energy of quantum fields, was experimentally verified by Casimir (1948). From a cosmologists point of view, the vacuum term can theoretically play an important role in the dynamics of the expanding universe (see §1.1.6). Indeed something with very similar properties is a requirement of inflationary models, which have become an indispensible part of the modern paradigm (§1.2.1).

The current trend for including a significant vacuum contribution to the energy density has been observationally motivated by a number of remarkable recent results, most notable are the high-z supernovae results of Aldering *et al.* (1998) and Riess *et al.* (1998). Although cosmologically justifiable the cosmological constant/vacuum energy component remains something of a conundrum: consider that the standard model of particle physics currently predicts a value for the cosmological constant that is some 120 orders of magnitude below that required by cosmologists to explain their observations. If the constant is here to stay then clearly there is much by way of unknown physics yet to discover.

The equation of state for all three contributions to the total energy density can be conveniently parameterised by

$$p = w\rho c^2, \tag{1.26}$$

where w takes the values

$$\begin{array}{ll} w = 0 & \text{dust} \\ w = 1/3 & \text{radiation} \\ w = -1 & \text{vacuum.} \end{array} \tag{1.27}$$

The conservation of energy implies a relationship

$$d(\rho a^3) = -\frac{3p}{c^2} a^2 da, \tag{1.28}$$

from which it follows that the energy density grows with scale factor like

$$\begin{array}{lcll} \rho_m(a) & = & \rho_m(a_0)a^{-3} & \text{dust} \\ \rho_r(a) & = & \rho_r(a_0)a^{-4} & \text{radiation} \\ \rho_v(a) & = & \text{constant} & \text{vacuum.} \end{array} \tag{1.29}$$

This is an important result. It states that in the past the universe was dominated by the radiation component. At some point in time matter and radiation became equivalent and from then onwards the universe was dominated by its matter content. The unusual evolution of the vacuum energy indicates that, even if the vacuum contribution were initially quite small, there will eventually come a time when its presence becomes significant. The repercussion of this are discussed in §1.1.6 and §1.2.1.

Equations (1.29) can be readily understood as follows. The density of ordinary matter goes like 1/volume. Since lengths scale with a the first result is obvious. The additional factor of $1/a$ for the radiation comes from the fact that the energy of photons is also redshifted away with the expansion of the universe. The constant value of ρ_v follows because the universal expansion is continually generating more vacuum, the energy is thus never "thinned out".

Defining the quantities Ω_m, Ω_r and Ω_v in analogy with equation (1.25), we can cast equation (1.23) as

$$\frac{Kc^2}{H^2a^2} = \Omega_m(a) + \Omega_r(a) + \Omega_v(a) - 1, \tag{1.30}$$

in other words, the condition for spatial flatness is

$$\Omega_m(a) + \Omega_r(a) + \Omega_v(a) = 1. \tag{1.31}$$

The total density parameter can then be written as

$$\Omega(a) = \Omega_m(a) + \Omega_r(a) + \Omega_v(a). \tag{1.32}$$

1.1.6 Cosmological models

We can obtain a solution for the dependance of the scale factor on time by integrating Friedmann equation (1.23). Solutions are most easily found by re-writing in terms of a new time parameter $\tau = H_0 t$, *i.e.* in numbers of Hubble times, $1/H_0$. In terms of observables at the present epoch we obtain

$$\left(\frac{da}{d\tau}\right)^2 = \Omega_m\left(a^{-1} - 1\right) + \Omega_r\left(a^{-2} - 1\right) + \Omega_v\left(a^2 - 1\right), \tag{1.33}$$

where the effective density parameter for curvature has been defined by

$$\Omega_K(a) = -\frac{Kc^2}{H^2} = \Omega(a) - 1. \tag{1.34}$$

Details of the solutions to this equation can be found in Felten & Isaacman (1986) and the excellent review by Carroll *et al.* (1992). The behavior for a range of Ω_m and Ω_v are summarised in figure 1.1 and for five specific models in figure 1.2. The figures are discussed below.

An important result can actually be obtained from the Friedmann equations without the need to integrate. It is worth mentioning this first. Equation (1.22) implies that $\ddot{a} < 0$ provided $\rho > pc^2/3$, in other words the graph of a vs. t is concave. This means that if $a > 0$ at some time, then an inevitability of the past history was a point at which $a = 0$. At this singularity both the matter and radiation density components diverge ($\rho_m \propto a^{-3}, \rho_v \propto a^{-4}$) creating an environment of unimaginable hostility. The singularity was famously dubbed the Big Bang by Fred Hoyle, ironically a leading advocate of steady state cosmologies. In fact just prior to the point at which $a = 0$, the classical theory of general relativity breaks down. In reality therefore, one cannot infer much about the evolution of the universe at *very* early times without a quantum theory of gravity, something that is currently beyond our understanding.

Quantitatively the effect of Ω on the evolution of the scale factor for $\Omega_v \geq 0$ is as follows: when $\Omega > 1$ (closed universe) the scale factor has cycloid solutions, expanding to a maximum and re-collapsing in a finite time (the Big Crunch); if $\Omega < 1$ (open universe) the expansion continues unbounded for all times; for $\Omega = 1$ (flat or critical universe) the universe expands forever but $\dot{a} \to 0$ as $t \to \infty$.

The flat universe is one beloved of theorists due to its simplicity. Three useful limiting approximations for the flat case are $\Omega_m = 1$, $\Omega_r = 1$ and $\Omega_v = 1$. Analytical expressions for $a(t)$ can be obtained easily for each. For the matter dominated (Einstein-de Sitter) universe we have

$$a(t) \propto t^{2/3}. \tag{1.35}$$

When the universe is radiation dominated the evolution is similar, though with a different power law

$$a(t) \propto t^{1/2}. \tag{1.36}$$

For a universe dominated by the vacuum energy, the scale factor grows rapidly

as

$$a(t) \propto \exp[Ht]. \tag{1.37}$$

where H is the Hubble parameter $H = \sqrt{8\pi G\rho_v/3}$, which remains constant for all times. This expansion is known as a de Sitter phase and has an important application in inflationary cosmology, see §1.2.1.

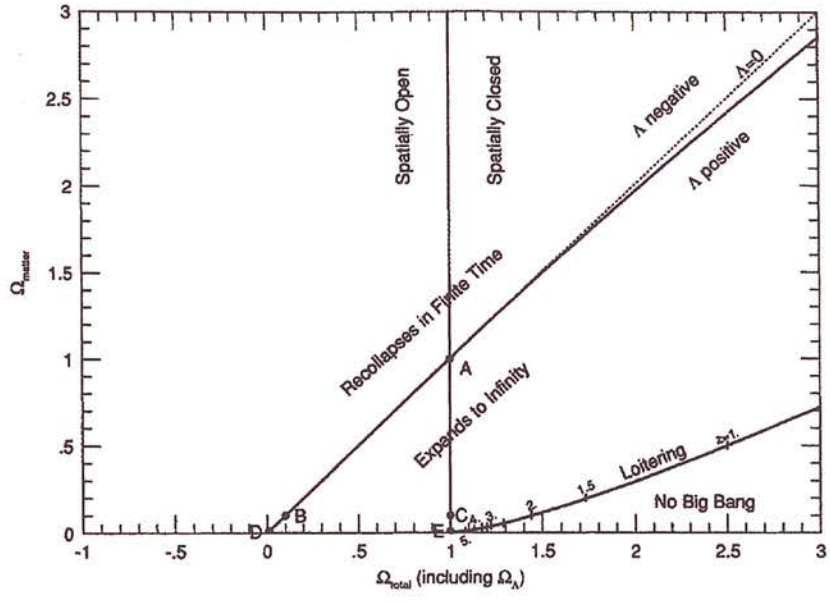

Figure 1.1: Schematic illustrating the fate of the universe as a function of the matter density Ω_m and total density $\Omega = \Omega_m + \Omega_v$. The letters label the current value of the density parameter for the five models discussed in the text. Taken from Carroll *et al.* (1992).

Figure 1.1 summarises in detail the behaviour of $a(t)$ for the case where Ω_r is negligible. The most physically interesting portion of the figure, given today's measurements (see, for example Primack, 2000) is the region bounded by $0 < \Omega < 1$ and $0 < \Omega_m < 1$ and by the line of positive vacuum energy (designated positive Λ in the figure). For the small region where Ω is large and dominated by the vacuum term, the Friedmann equations do not predict a big bang. This is because of the $p = -\rho$ equation of state for the vacuum which gives $\ddot{a} > 0$ in equation (1.22).

The points A to E label five plausible cosmological models. Their evolution according to equation (1.33) is plotted in figure 1.2. The scale factors in each case have been normalised to give $a = 1$ at the present day. Model A is the

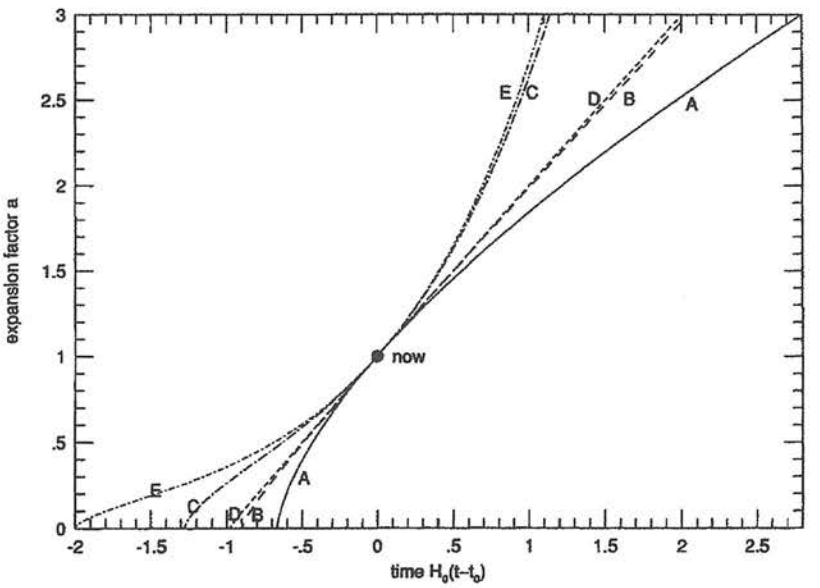

Figure 1.2: The evolution of the scale factor a for five different Friedmann models. The scale factor is normalised to be 1 in the present day. The labels A to E identify the models on figure 1.1. Taken from Carroll *et al.* (1992)

Einstein-de Sitter universe, showing a characteristic $t^{2/3}$ expansion. The open, non-Ω_v, models, B and D, illustrate nearly identical behavior down to very early times when the mass content of B becomes important and affects the evolution. Both E and C are Ω_v-dominated flat models. The behaviour of E is pure de Sitter, showing a drawn out exponential tail to the past. The mass content of C ensures a big bang. Models C and E have both entered an exponential phase by t_0. Note that the youngest model is the Einstein-de Sitter universe and the oldest are those with a vacuum term.

What is not shown clearly in figure 1.2 is the similarity of the low t evolution of the non-empty models. This is a generic predication of the Friedmann equations which can be demonstrated by re-writing equation (1.23) in the form

$$\Omega(a) - 1 = \frac{\Omega - 1}{\Omega_v a^2 + \Omega_m a^{-1} + \Omega_r a^{-2} - \Omega + 1}, \tag{1.38}$$

where $\Omega(a)$ is the density parameter at the epoch a and all other Ω_x terms are evaluated at the present day. Equation (1.38) is illustrated in figure 1.3 for four different cosmologies. One sees that the low a behaviour of the matter (or equivalently radiation) dominated models is identical – all tend towards the Einstein-de Sitter case as $a \to 0$. Open models become "more open" as a grows

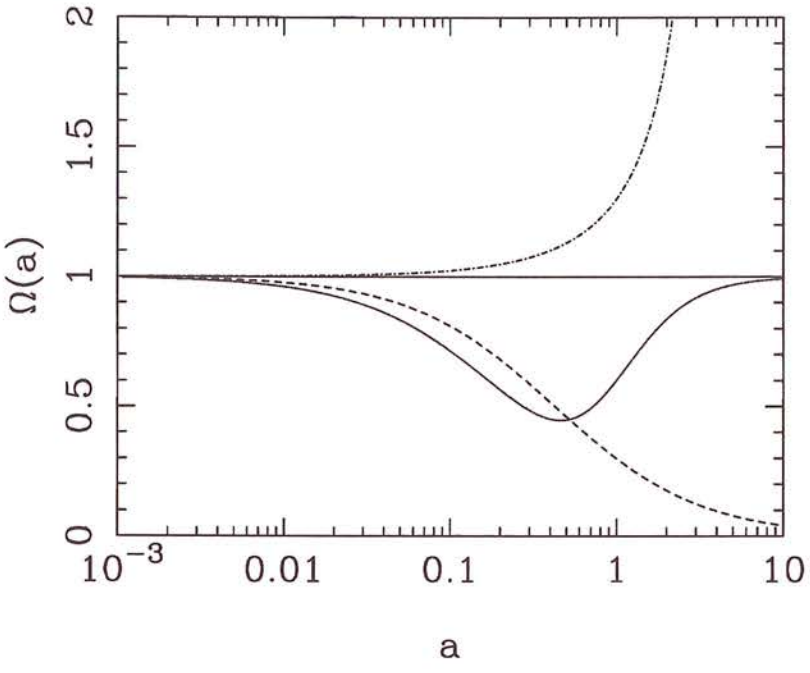

Figure 1.3: Evolution of the density parameter Ω as a function of scale factor a. Lines shown are for an open ($\Omega(a_0) = 0.3$; dashed) and closed ($\Omega(a_0) = 1.3$; dot-dashed), matter dominated universe and a universe with a significant vacuum contribution ($\Omega_m(a_0) = 0.1$, $\Omega_m(a_0) = 0.5$; dotted). The Einstein-de Sitter universe is also shown ($\Omega(a_0) = 1$; solid)

large whereas closed models become more closed up to a limiting value of a when collapse begins. For the model with $\Omega_v \neq 0$ the universe is ultimately driven towards spatial flatness irrespective of the initial conditions. The Einstein-de Sitter universe is the only stable case for which $\Omega = 1$ for all times.

Current estimates of Ω_m lie within a factor of a few of unity. This indicates that at early times the density parameter would have been equal to one to a remarkable degree of precision. For example at the Planck time $t_p = 10^{-43}s$, where classical gravitation is known to break down, we would have $|\Omega - 1| \approx 10^{-55}$. This fine tuning of initial conditions is thought by many to be unacceptable and reason enough to assume $\Omega = 1$. This point is returned to in §1.2.1.

1.1.7 The hot big bang: a thermal history

During the early history of the Universe the dominant contribution to the energy density was from the radiation component. The average temperature of the

Universe at these times was $T \propto a^{-1}$. To a good approximation the radiation dominated Universe evolved through a sequence of states of thermal equilibrium. Before about the Planck time $t_P = 10^{-43}s$ the temperature and density were high enough that current physics is unable to provide an adequate description of events. After t_P the Universe cooled with expansion, the subsequent phase transitions of the fundamental fields and interactions between particle species left the Universe in the state that we observe today. The following is a very short summary, for (considerably) more detail see Kolb & Turner (1990).

$T \sim 10^{19} - 10^{15}$ GeV $\quad t \sim 10^{-43} - 10^{-37}$ s

GUT ERA. Quantum gravitational effects become unimportant for the first time. Particle interactions described by Grand Unified Theory (GUT). Origin of particle anti-particle asymmetry due to violation of baryon number at these energies. The GUT phase transition at $T \sim 10^{15}$ GeV decouples strong from electroweak force. Formation of topological defects. In inflationary cosmology there is a period of near exponential expansion at this stage (see §1.2.1).

$T \sim 10^{15} - 10^{2}$ GeV $\quad t \sim 10^{-37} - 10^{-11}$ s

ELECTROWEAK ERA. Electromagnetic and weak forces are united in electroweak force. Free quarks and gluons.

$T \sim 100$ GeV $-$ 300 MeV $\quad t \sim 10^{-11} - 10^{-5}$ s

QUARK ERA. Electroweak symmetry broken at $T \sim 100$ GeV. Leptons acquire mass and intermediate vector bosons give rise to massive bosons and photons. Massive bosons annihilate or decay quickly.

$T \sim 300 -$ 130MeV $\quad t \sim 10^{-5}$ s

HADRON ERA. Quark – hadron phase transition as colour-neutral quark triplets form baryons and colour neutral quark-antiquark pairs form mesons, which decay rapidly producing photons.

$T \sim 130\,(10^{12}) -$ 0.5 (5×10^{9}) MeV (K) $\quad t \sim 10^{-5} - 10$ s

LEPTON ERA. Neutrinos decouple from other fields. They subsequently free stream to the present day 1.9 K neutrino background. Leptons and antileptons annihilate. Electron-positron anihilation produces last energy input into the Universe before recombination (see below) raising temperature by a factor 11/4. At around $T \sim 10^9$ K the process of *nucleosynthesis* fuses protons and neutrons

together to create the light elements – see §1.1.8.

$T \sim 10^5$ K $\quad t \sim 10^{10}$ s

MATTER–RADIATION EQUALITY. Matter and radiation components become equal, changing the dynamics of the expanding Universe. Perturbation growth for non-baryonic matter begins on scales inside the horizon (see §1.2.2 and §1.4).

RECOMBINATION. Temperature drops below ionization energy of atomic hydrogen causing Thomson scattering cross-section to drop sharply. Matter and energy effectively decouple. Free streaming photons redshift to present day Cosmic Microwave Background, see §1.1.9

1.1.8 Nucleosynthesis

Big bang nucleosynthesis, the creation of light elements from a primordial nucleon population, was first proposed by Gamow (1946). The predictions of the theory provide strong constraints on the density of baryonic material in the Universe.

Nucleosythesis began when the Universe cooled to $T = 10^9 K$. At this point the neutrinos decoupled from other fields and the weak interactions that convert between nucleon species became slow with respect to the expansion time scale. This effectively froze the neutron to proton ratio which had previously been a decreasing function of T. By a remarkable coincidence, the temperature of neutrino decoupling coincided approximately with the binding energy for deuterium; remarkable because otherwise the frozen neutron population would have bled away by β decay. The neutrons and protons thus combined to form deuterium and subsequently ^{4}He and other light elements. The important reactions for ^{4}He production are

$$p + n \rightleftharpoons \mathrm{D} + \gamma$$

$$D + D \rightarrow {}^3\mathrm{He} + \mathrm{n}$$

$${}^3\mathrm{He} + \mathrm{d} \rightarrow {}^4\mathrm{He} + \mathrm{p}.$$

The conversion to ^{4}He is not total and traces of primordial D and ^{3}He can still be measured. The precise predictions for the primordial abundances of H, D, ^{3}He, ^{4}He and ^{7}Li are obtained by numerical solution of the coupled rate equations for all possible nuclear reactions, a feat first achieved by Wagoner *et al.* (1967). In

fact one finds that the Helium fraction

$$Y = 1 - \mathrm{H},$$

together with the abundance ratios

$$\frac{\mathrm{D} + {}^3\mathrm{He}}{\mathrm{H}}, \quad \frac{{}^3\mathrm{He}}{\mathrm{H}} \quad \text{and} \quad \frac{{}^7\mathrm{Li}}{\mathrm{H}},$$

all depend in a *different* way on the combination $\Omega_b h^2$, where Ω_b is the density parameter for baryons. The primordial abundances can be inferred from observation in a number of different ways – for example from stellar atmospheres, interstellar absorption/emission lines or from the spectra of distant galaxies and quasars. Recent measurements have yielded close agreement with abundances noted above for (Walker *et al.*, 1991; Smith *et al.*, 1993)

$$0.011 \leq \Omega_b h^2 \leq 0.019. \tag{1.39}$$

This gives an alarmingly low value for the baryon content of the Universe. Allowing for an acceptable uncertainty in h, the baryon fraction is constrained by $0.011 \leq \Omega_b \leq 0.119$, well below the critical value beloved of theorists. In fact present observations put $\Omega \geq 0.2$, which suggests that a large fraction of the energy content of the Universe is non-baryonic – see §1.2.2.

1.1.9 The Cosmic Microwave Background

The serendipitous discovery by Penzias & Wilson (1965) of an isotropic, $\sim 3\ K$ extragalactic background of microwaves, may have been one of the most important finds of the 20th century. The Cosmic Microwave Background (CMB) radiation came as a remarkable verification that the Universe had its origins in a dense, hot, nearly homogeneous plasma – exactly as the standard model predicts. Such a background, whose existence was first postulated by Gamow (1949), is virtually impossible to form from any other model, apart from in the most contrived of pictures. Since the 1960s both the theoretical and observational study of the microwave background have grown immeasurably in sophistication to the extent that the CMB now represents one of the major sources of information about cosmology and primordial physics.

The background radiation originates from a period in the Universe's history when the temperature dropped below the ionization energy of atomic hydrogen for the

first time. Before this period, the radiation component was tightly coupled to the (baryonic) matter due to Thompson scattering of photons by electrons and electromagnetic interaction of the electrons with the baryons (protons). Once below the ionization energy, the Thomson scattering cross section dropped sharply as electrons and protons combined into hydrogen atoms. The baryon–photon plasma then decoupled and the photons were left free to travel relatively unimpeded to the present day, ignoring the effects of intervening matter. This process, known rather confusingly as *recombination*, occurred around redshift $z_{rec} \sim 1500$.

The CMB radiation has been shown to be that of an almost perfect black body over the range of a few mm to a few cm in wavelength. The spectrum is fit by a Planck function with characteristic temperature

$$T = 2.728 \pm 0.004K,$$

where the errors indicate 95% confidence (Fixsen *et al.*, 1996, using COBE data).

The CMB is not completely isotropic. The most obvious effect is dipolar and originates from our velocity with respect to the comoving frame of the CMB radiation. Our net velocity is a combination of the orbital motion of the Earth, the Sun's orbit about the centre of the Galaxy, the motion of our local group of galaxies towards the centre of the local supercluster and the velocity of the supercluster with respect to the CMB. Calculation of the CMB dipole has been an area of great interest over the past few decades (see Strauss & Willick, 1995, and references therein).

After subtraction of the dipolar velocity anisotropy, the CMB is now known to possess further temperature fluctuations at around the 10^{-5} level. These fluctuations are thought to be primordial in origin. Sachs & Wolfe (1967) were the first to propose the existence of temperature anisotropies resulting from metric perturbations at the time of recombination (the Sachs–Wolfe effect). There ensued a race to detect such fluctuations observationally that lasted for 25 years. The detection was eventually made by Smoot *et al.* (1992) with the COBE satellite, another of the great experimental achievements of the last century, essentially launching one of the most active branches of research in cosmology. Recently the MAXIMA and BOOMERanG experiments (de Bernardis *et al.*, 1999; Lange *et al.*, 2000; Hanany *et al.*, 2000; Balbi *et al.*, 2000) have taken the study of CMB fluctuations to a new level of accuracy and the entire community eagerly awaits

the launch of the MAP[1] and Planck[2] satellites, which will push the boundaries of the experimental and theoretical side of this subject to the limit.

Of crucial importance is the fact that the spectrum of temperature fluctuations – broadly speaking the level of fluctuation on a given angular scale on the sky – depends sensitively on a large number of cosmological parameters. The shape of this spectrum is well understood and derives from the physical mechanisms by which primordial density perturbations are transformed into temperature fluctuations at the epoch of recombination. Also important are the various processes by which the temperature perturbations are affected during their transfer from z_{rec} to the present day. The contributions to the final temperature perturbation spectrum are classified as *primary* or *secondary* anisotropies, depending upon whether they originate at the source or along the flight path of the photons. An excellent review of these processes can be found in Hu & Sugiyama (1995) (and references therein).

The dominant primary anisotropy on large angular scales arises from the Sachs-Wolfe effect. Photons emanating from dense areas at the time of recombination will be gravitationally redshifted and time dilated as they climb out of potential wells. The net result for adiabatic perturbations (see §1.4.1) is that photons emanating from dense spots are cooled by a factor

$$\frac{\Delta T}{T} = \frac{\delta\phi}{3c^2} \tag{1.40}$$

with respect to the background. For isocurvature perturbations (again see §1.4.1) the level is a factor of six higher, a fact that has effectively ruled out many isocurvature models to high confidence. Other primary effects are the Doppler shifting of photons arising from bulk motions at the recombination epoch, and the acoustic oscillations of the baryons on scales inside the sound horizon, which is discussed in §1.4.1. The baryon oscillations are very important because they give rise to distinctive peaks in the CMB spectrum with a shape that is heavily dependant upon cosmology. For example, the angular scale of the first of these peaks on the sky is related to the Jeans length at recombination in a way dependant upon the spatial curvature.

Examples of secondary anisotropies include: the integrated Sachs–Wolfe and Rees–Sciamma effects, which give rise to further redshifting of CMB photons due

[1] see http://map.gsfc.nasa.gov/

[2] see http://astro.estec.esa.nl/SA-general/Projects/Planck/

to changes in the potential fluctuations with time over the photon trajectories (see for example the review by Refregier, 1999); the Sunyaev-Zeldovich effect, where photons scatter off the hot, ionized gas in galaxy clusters (Sunyaev & Zel'dovich, 1970, 1980); reionisation of the Universe by a significant energy influx at high redshift *e.g.* from primordial star formation and/or quasars (see, for example Hu, 2000, and references therein for a recent discussion) ; gravitational lensing by intervening objects (*e.g.* Bernardeau, 1998); and foreground contamination from unobserved sources (*e.g.* Tegmark *et al.*, 2000).

1.2 The modern paradigm

The standard model of the big bang has proved to be remarkably successful in explaining some of the general features of the observable Universe: the expansion of the galaxies; the existence of the CMB; and the origin of the light elements. There are, however, a number of outstanding issues that cannot be answered within the confines of the standard picture. The solutions to these problems have themselves now become something of a standard in modern cosmology.

1.2.1 Inflation

Inflation was originally invoked as a clever way to solve some of the classic problems associated with the standard big bang model. It has since evolved to become a rich and diverse area of theoretical research, furnishing us with an elegant picture of the early Universe that ties in extremely well with large scale structure formation and the CMB. The concept of inflation was germinated by Starobinskii (1979) and Guth (1981). It was quickly seized upon by a large number of workers, the original ideas being manipulated and recast in numerous different ways (see figure 1.4). Excellent reviews are to be found in Liddle & Lyth (1993), Kolb & Turner (1990) and Linde (1990).

The specific problems that inflation addresses are:

THE HORIZON PROBLEM. The temperature of the CMB is isotropic over scales far in excess of the particle horizon calculated within the standard model (this correspond to about 1^o on the sky today). How could regions that are apparently causally unconnected have attained thermal equilibrium?

THE FLATNESS PROBLEM. As discussed in §1.1.6, the present day density parameter is $\mathcal{O}(1)$, indicating that at early times $\Omega(a) = 1$ to very high precision. How did such a fine tuning occur?

THE STRUCTURE PROBLEM. The Universe in not locally homogeneous. The inhomogeneities are thought to have arisen as the result of gravity acting over time on small density perturbations. What is the origin of these initial fluctuations?

THE RELIC PROBLEM. Topological defects such as monopoles and unwanted relic particles are predicted to form in large numbers at very early times. Why do we not observe them in the present day Universe?

Although inflationary models vary a great deal in detail, the common prediction is that there was a period of accelerated ($\ddot{a} > 0$), expansion at an early point in the Universe's history. This period of expansion provides a neat solution to all of the above problems.

As discussed in §1.1.6, one way in which an accelerated expansion can occur within a Friedmann-Robertson-Walker Universe, is for the energy density to be dominated by a component with equation of state $\rho + 3p^2/c^2 < 0$. In inflation this is exactly what is thought to happen. The equation of state is that for a minimally coupled scalar quantum field ϕ, called the *inflaton*, moving within a potential $V(\phi)$. The (classical) equation of motion for such a field is given by

$$\ddot{\phi} + 3H\dot{\phi} + dV/d\phi = 0, \tag{1.41}$$

where the pressure and density of the field can be shown to be

$$p = -V(\phi) + \frac{1}{2}\dot{\phi}^2, \quad \rho = V(\phi) + \frac{1}{2}\dot{\phi}^2. \tag{1.42}$$

Under *slow roll* conditions $\dot{\phi}^2$ is small compared to $V(\phi)$ and $\ddot{\phi}$ negligible in equation (1.41). The equation of state for ϕ is then that required for rapid, accelerated phase of expansion.

The various means of beginning and ending inflation, and the detailed shape of the potential $V(\phi)$, loosely categorise the different models. Generally speaking inflation is initiated either via a phase transition or randomly (chaotically), and ended when scalar field comes to rest within a minimum of the potential. The process by which the energy of the inflaton is transfered to the other components is known as *reheating*. In most models this occurs when the inflaton field begins to oscillate rapidly about the minimum in $V(\phi)$ producing ϕ-particles. These

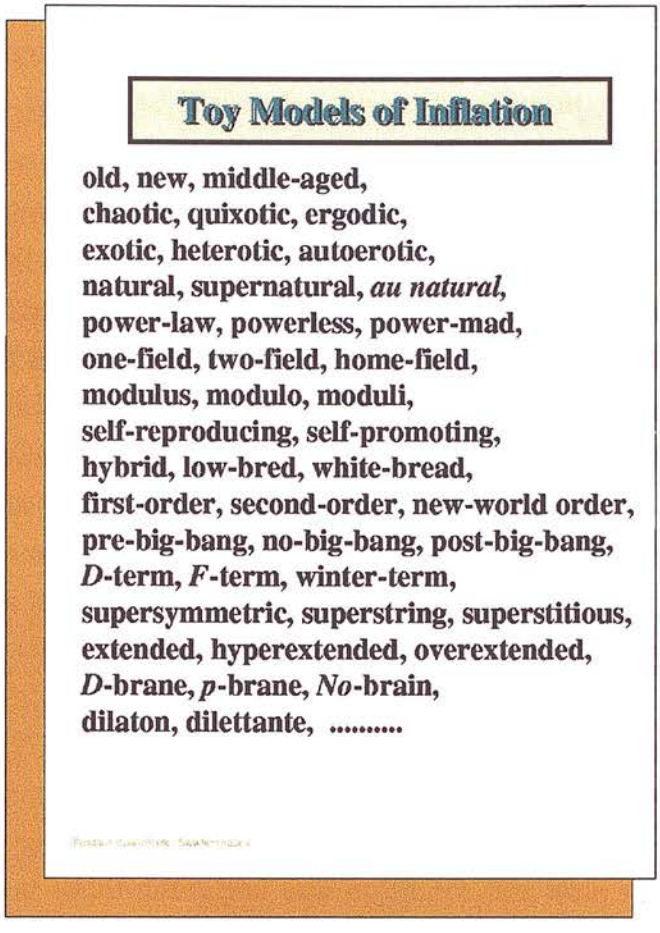

Figure 1.4: The bewildering array of inflationary models, according to "Rocky" Kolb (overhead from talk at Ettore Majorana School, Erice, Sicily 1999).

subsequently decay into a number of other fields which thermalise and reheat the radiation component to a high temperature.

In this picture the horizon and flatness problems are readily solved as follows. With a period of near exponential expansion of the scale factor, the integral for the particle horizon diverges. This means that scales before inflation over which causal connections could have been made, were stretched far outside the Hubble radius during the inflationary phase. This accounts for the isotropy of the CMB. The flatness problem is solved from the arguments of §1.1.6: a universe dominated by a component with $p \propto -\rho$ will quickly evolve towards spatial flatness whatever the initial conditions. The number of e-foldings of the scale factor that it takes to ensure $\Omega = 1$ corresponds remarkably with that required to solve the flatness problem ($\ln f \gtrsim 60$; see Peacock 1999 for example). The relic problem is also dealt

the launch of the MAP[1] and Planck[2] satellites, which will push the boundaries of the experimental and theoretical side of this subject to the limit.

Of crucial importance is the fact that the spectrum of temperature fluctuations – broadly speaking the level of fluctuation on a given angular scale on the sky – depends sensitively on a large number of cosmological parameters. The shape of this spectrum is well understood and derives from the physical mechanisms by which primordial density perturbations are transformed into temperature fluctuations at the epoch of recombination. Also important are the various processes by which the temperature perturbations are affected during their transfer from z_{rec} to the present day. The contributions to the final temperature perturbation spectrum are classified as *primary* or *secondary* anisotropies, depending upon whether they originate at the source or along the flight path of the photons. An excellent review of these processes can be found in Hu & Sugiyama (1995) (and references therein).

The dominant primary anisotropy on large angular scales arises from the Sachs-Wolfe effect. Photons emanating from dense areas at the time of recombination will be gravitationally redshifted and time dilated as they climb out of potential wells. The net result for adiabatic perturbations (see §1.4.1) is that photons emanating from dense spots are cooled by a factor

$$\frac{\Delta T}{T} = \frac{\delta\phi}{3c^2} \tag{1.40}$$

with respect to the background. For isocurvature perturbations (again see §1.4.1) the level is a factor of six higher, a fact that has effectively ruled out many isocurvature models to high confidence. Other primary effects are the Doppler shifting of photons arising from bulk motions at the recombination epoch, and the acoustic oscillations of the baryons on scales inside the sound horizon, which is discussed in §1.4.1. The baryon oscillations are very important because they give rise to distinctive peaks in the CMB spectrum with a shape that is heavily dependant upon cosmology. For example, the angular scale of the first of these peaks on the sky is related to the Jeans length at recombination in a way dependant upon the spatial curvature.

Examples of secondary anisotropies include: the integrated Sachs–Wolfe and Rees–Sciamma effects, which give rise to further redshifting of CMB photons due

[1] see http://map.gsfc.nasa.gov/

[2] see http://astro.estec.esa.nl/SA-general/Projects/Planck/

to changes in the potential fluctuations with time over the photon trajectories (see for example the review by Refregier, 1999); the Sunyaev-Zeldovich effect, where photons scatter off the hot, ionized gas in galaxy clusters (Sunyaev & Zel'dovich, 1970, 1980); reionisation of the Universe by a significant energy influx at high redshift *e.g.* from primordial star formation and/or quasars (see, for example Hu, 2000, and references therein for a recent discussion) ; gravitational lensing by intervening objects (*e.g.* Bernardeau, 1998); and foreground contamination from unobserved sources (*e.g.* Tegmark *et al.*, 2000).

1.2 The modern paradigm

The standard model of the big bang has proved to be remarkably successful in explaining some of the general features of the observable Universe: the expansion of the galaxies; the existence of the CMB; and the origin of the light elements. There are, however, a number of outstanding issues that cannot be answered within the confines of the standard picture. The solutions to these problems have themselves now become something of a standard in modern cosmology.

1.2.1 Inflation

Inflation was originally invoked as a clever way to solve some of the classic problems associated with the standard big bang model. It has since evolved to become a rich and diverse area of theoretical research, furnishing us with an elegant picture of the early Universe that ties in extremely well with large scale structure formation and the CMB. The concept of inflation was germinated by Starobinskii (1979) and Guth (1981). It was quickly seized upon by a large number of workers, the original ideas being manipulated and recast in numerous different ways (see figure 1.4). Excellent reviews are to be found in Liddle & Lyth (1993), Kolb & Turner (1990) and Linde (1990).

The specific problems that inflation addresses are:

THE HORIZON PROBLEM. The temperature of the CMB is isotropic over scales far in excess of the particle horizon calculated within the standard model (this correspond to about 1^o on the sky today). How could regions that are apparently causally unconnected have attained thermal equilibrium?

$(M/L)_{\rm LSS} > (M/L)_{\rm clusters}$.

The positions of the galaxies relative to the underlying dark matter distribution is an issue of central importance in cosmology. If the dark matter contribution dominates the mass density of the Universe then the pattern of large scale structures should be dominated by the gravitational evolution of the collisionless component; theories of structure formation must reflect this. But since what is observed is just the baryonic "foam" atop an unseen ocean of gravitating mass, there will inevitably be discrepancies when comparing theory with observation. Kaiser (1984) pointed out that galaxy clusters should be more strongly clustered than the galaxies themselves if the process of galaxy formation takes place preferentially in regions of high density. Kaiser's theoretical argument fitted in well with the longstanding observation that rich Abell clusters have different clustering properties to galaxies. This line of thought led to the idea of a galaxy–dark matter *bias*, which will be discussed further in §1.5 and chapter 3.

What form does the dark matter take? For non-baryonic dark matter the most popular explanation is in terms of Weakly Interacting Massive Particles (WIMPS). These are thought to be relic particles from the big bang that froze out or decoupled at an early point in the Universe's history. Their defining property is that they only weakly interact with normal matter except through gravitation, explaining the lack of observational evidence that points to their existence. WIMPS may seem a little contrived, however there are extensions to the standard model of particle physics (*e.g.* supersymmetry) that predict an abundance of relic particles with similar properties. The velocity of the WIMPS at the time that they decouple from normal matter splits the dark matter models into two broad classes – hot and cold.

Hot Dark Matter (HDM) particles froze out with relativistic velocities. A good example of this type of particle is the $\sim$ 1eV neutrino. HDM models (White *et al.*, 1983, 1984) run into difficulties since the high velocity of the particles has a considerable damping effect on primordial structure formation that is hard to reconcile with observation. In HDM models large scale structures grow in a "top down" fashion as large sheets and filaments collapse first and then fragment.

Cold Dark Matter (CDM) particles decouple with low velocities. Although not so strongly motivated theoretically as massive neutrinos, their effect on structure formation is more compatible with observation. In the CMD scenario there is

negligible damping of primordial perturbations. Subsequently fluctuations have a chance to coalesce and the growth of large scale structure proceeds from small scales upwards.

At the time of writing the CDM model is most highly favoured, although there are numerous concerns about its detailed predictions. One obvious failure of the model is that it predicts an overabundance of compact halo type objects on sub-galactic scales. This is a result of the hierarchical nature of CDM structure formation and has been shown in ultra high resolution numerical simulations (Moore *et al.*, 1999; Klypin *et al.*, 1999). The abundance of halos on small scales appears to be at odds with observations of our local neighbourhood and indicates that there may be properties of the dark matter that differ significantly from pure CDM. An alternative view is that the high resolution simulations are flawed in some way, not taking into account the correct dynamical effects experienced by real dark matter subhalos in larger embedding objects (see van Kampen, 2000).

Another significant issue on a related theme is the controversial observation that the cores of dwarf galaxies have density profiles that do not fit well with a pure CDM picture. For CDM the density should increase to a cusp towards the centre of the galaxy halo. Observations of the rotation curves of dwarf galaxies by, among others, Flores & Primack (1994); Moore (1994); Burkert (1995); Firmani *et al.* (2000), have indicated that in fact the density profile flattens off in the inner regions of the halos. It has been suggested that this is evidence of self interaction or some other peculiar property of the dark matter. Recently van den Bosch & Swaters (2000) re-examined the issue, suggesting that previous observations were inconclusive and rather that, while alternative dark matter models cannot be ruled out, the rotation curves of dwarf galaxies are not inconsistent with CDM.

The existence of some form of non-interacting (collisionless) dark matter is widely accepted but far from experimentally verified. Even so, its inclusion as the dominant form of *mass* density in the Universe has become part of cosmological lore, indeed on observational grounds it is almost impossible to conceive of a cosmological model that does not include a significant contribution from dark matter. The detailed nature of dark matter particles will not be settled completely until their detection in a particle accelerator, however in the mean time there is much that can be learnt by considering their effect on the formation and evolution of large scale structure.

1.3 Cosmological random fields

One does not seriously expect that a cosmological model should be able to predict in detail the *exact* configuration of the Universe at any given time. Rather we look for a statistical description in terms of a set of continuous random fields $\phi(\boldsymbol{x})$[4] . These fields are stochastic in the sense that we suppose our Universe represents one particular realisation drawn at random from an *ensemble* with probability distribution $P[\phi]$.

The infinitesimal joint probability that the field at N specified positions takes the values $\phi(x_i) \rightarrow \phi(x_i) + d\phi(x_i)$ defines the N-point probability distribution functions

$$dP = P(\phi_1, \phi_2 ..., \phi_N)\, d\phi_1 d\phi_2 ... d\phi_N, \tag{1.44}$$

where the shorthand ϕ_i denotes $\phi(x_i)$ where appropriate. The moments of these distributions are found by averaging over the ensemble so that

$$\langle \phi_1^{m_1} \phi_2^{m_2} ... \phi_r^{m_r} \rangle = \int d\phi_1 d\phi_2 ... d\phi_N\, \phi_1^{m_1} \phi_2^{m_2} ... \phi_r^{m_r}\, P(\phi_1, \phi_2, .., \phi_N), \tag{1.45}$$

where $r \leq N$ and with m_r an integer. In the limit that $N \rightarrow \infty$ the N-point distribution function becomes the functional $P[\phi]$, providing a complete statistical specification of the field.

The simplest statistical quantity that one can construct in this hierarchy is the 1-point distribution function, defined by the infinitesimal probability

$$dP = P(\phi)\, d\phi, \tag{1.46}$$

whose moments are

$$\langle \phi^m \rangle = \int d\phi\, \phi^m P(\phi). \tag{1.47}$$

In general, the moments of all the distribution functions in the hierarchy can be expanded into a series of irreducible *cumulants* or *connected* parts. The expansion follows a partitioning of the set so that

$$\begin{aligned} \langle \phi_1 \phi_2 ... \phi_N \rangle &= \langle \phi_1 \rangle_c \langle \phi_2 \rangle_c ... \langle \phi_N \rangle_c + \langle \phi_1 \rangle_c \langle \phi_2 ... \phi_N \rangle_c + \text{perms} \\ &+ \langle \phi_1 \phi_2 \rangle_c \langle \phi_3 ... \phi_N \rangle_c + \text{perms} + ... \\ &+ \langle \phi_1 ... \phi_S \rangle_c \langle \phi_{S+1} ... \phi_N \rangle_c + \text{perms} + \langle \phi_1 \phi_2 ... \phi_N \rangle_c \end{aligned} \tag{1.48}$$

[4]No (direct) connection with the inflaton field of §1.2.1 is intended, they are just represented by the same symbol.

where "perms" indicates a cyclic permutation of indices.

In practice true ensemble averages $\langle ... \rangle$ are impossible to measure since we are ultimately limited to observing only one particular realisation of the universe. Fortunately we may appeal to the *ergodic theorem* to come to our aid. The theorem states that for ergodic fields, ensemble averages are equivalent to volume averages if the number of independent regions of space is large (Adler, 1981). The theorem makes sense for cosmological fields over large separations; measurements taken in causally disconnected regions of space should be statistically independent and hence equivalent to different realisations of the ensemble.

1.3.1 Gaussian fields

Of particular importance in cosmology is the Gaussian random field. For these quantities all of the joint N-point probability distributions take the form,

$$P(\phi) = \frac{1}{[(2\pi)^N \, \mathrm{detC}]^{1/2}} \exp\Big[-\frac{1}{2} \sum_{i,j=1}^{N} \phi_i C_{ij}^{-1} \phi_j \Big], \tag{1.49}$$

where C_{ij} is the covariance matrix, the connected two-point moment of the field $C_{ij} = \langle \phi_i \phi_j \rangle_c$, which provides a measure of the coupling between different components of ϕ. In the limit that $N \to \infty$ the covariance matrix becomes the 2-point *correlation function*, discussed in the next section, §1.3.2. Of crucial analytic importance is that Gaussian random fields are fully specified by two point statistics, all higher order cumulants are zero. This means that the correlation function, and its Fourier space counterpart the power spectrum (§1.3.3), take on a highly significant role.

The existence of Gaussian fields in cosmology is partly justified by the Central Limit Theorem (Kendal & Stuart, 1969) which states that the combination of a large number of random processes results in a Gaussian distribution. The generic prediction of inflationary models is that the phases of the Fourier components of the primordial density perturbation field will be randomly distributed in the range $0 \leq \varphi \leq 2\pi$. This indicates that the superposition of a large number of such modes forms a Gaussian density field. A further important property of Gaussian fields is that their linear combination is also Gaussian. This is particularly useful since many interesting quantities can be formed from spatial derivatives of the density field (see §1.4 and §2.2), which in Fourier space just look like $\partial^n \delta \to (-i\boldsymbol{k})^n \delta_{\mathbf{k}}$.

In practice the distribution of intrinsic temperature anisotropies in the CMB does not appear to be *inconsistent* with that of a Gaussian (Banday *et al.*, 2000), however a compelling observational verification has yet to be presented. When smoothed on large scales the galaxy distribution appears well approximated by a Gaussian field (Nusser *et al.*, 1995; Stirling & Peacock, 1996) but the effects of nonlinear gravitational evolution (chapter 2), bias and redshift space distortion (chapter 3) are known to change this significantly (Taylor & Watts, 2000; Watts & Taylor, 2000). The non-Gaussian evolution of cosmological fields due to these processes is one of the central issues of this thesis.

1.3.2 The density correlation functions

Of particular interest for the statistical analysis of galaxy and mass clustering in the Universe, is the random field describing fractional variation of the local density about the mean. We thus define the dimensionless *density contrast* field as

$$\delta(\boldsymbol{x},t) = \frac{\rho(\boldsymbol{x},t) - \bar{\rho}(t)}{\bar{\rho}(t)} \tag{1.50}$$

and seek to describe its statistical properties. From henceforth we'll normally drop the explicit dependance on t except where necessary for clarity.

In the continuum limit, the irreducible moments of the probability distribution functional $P[\phi]$, for the field $\phi(\boldsymbol{x})$, are the correlation function. The most relevant of these functions are those of the first few orders. In terms of the δ field we define, in the most general sense,

$$\begin{aligned} \xi(\boldsymbol{x}_1,\boldsymbol{x}_2) &= \langle\delta(\boldsymbol{x}_1)\delta(\boldsymbol{x}_2)\rangle_c \\ \zeta(\boldsymbol{x}_1,\boldsymbol{x}_2,\boldsymbol{x}_3) &= \langle\delta(\boldsymbol{x}_1)\delta(\boldsymbol{x}_2)\delta(\boldsymbol{x}_3)\rangle_c \end{aligned} \tag{1.51}$$

and so on. These functions are a measure of the spatial clustering of the density fluctuations. For a homogeneous, isotropic random field, the correlations functions must depend only upon the distance between points *i.e.* $\xi(\boldsymbol{x}_1,\boldsymbol{x}_2) \rightarrow \xi(|\boldsymbol{x}_1 - \boldsymbol{x}_2|)$. In the limit of zero separation, the correlations functions reduce to the connected moments of the 1-point distribution function

$$\langle\delta^N\rangle_c = \xi_N(0) \equiv \langle\xi_N(\boldsymbol{x}_1,...,\boldsymbol{x}_n)\rangle_{\rm vol}. \tag{1.52}$$

An alternative, and more intuitive feel for the meaning of the correlation function comes from constructing a discrete realisation of the random field from the

continuous using the Poisson model (Peebles, 1980). The discrete field consists of a distribution of particles rather than a smoothly varying density fluctuation function. Briefly, we bin the Universe up into small volumes dV and calculate the probability that cells separated by distance x are both filled by a particle. Identifying $\bar{\rho}$ with the mean number of particles per unit volume, the *Poisson* probability for two cells to be occupied is

$$dP = \bar{\rho}^2 \, dV_1 \, dV_2. \tag{1.53}$$

When the particles are clustered the probability changes from Poisson by an amount proportional to the fluctuation, $(1 + \delta(\boldsymbol{x}_1))((1 + \delta(\boldsymbol{x}_2))$. Averaging over the ensemble, but not the Poisson process, we obtain

$$dP = \bar{\rho}^2 \, [1 + \xi(x_{12},]dV_1 \, dV_2 \tag{1.54}$$

which identifies the 2-point correlation function as the excess probability over Poisson for joint cell occupation. The 3-point, and higher, analogy is easy to write down

$$\begin{aligned} dP &= \bar{\rho}^3 \, [1 + \xi(\boldsymbol{x}_1, \boldsymbol{x}_2, \boldsymbol{x}_3]dV_1 \, dV_2 \, dV_3 \\ &= \bar{\rho}^3 \, [1 + \xi(x_{12}) + \xi(x_{13}) + \xi(x_{23}) + \zeta(\boldsymbol{x}_1, \boldsymbol{x}_2, \boldsymbol{x}_3)]dV_1 \, dV_2 \, dV_3, \end{aligned} \tag{1.55}$$

where the second equality follows by writing the three point correlation in terms of its irreducible parts, in analogy with equation (1.51).

The observed (real space) 2-point correlation function of galaxies is seen to obey a power law distribution

$$\xi(x) = \left(\frac{x_0}{x}\right)^{\gamma} \tag{1.56}$$

over a large range of scales. This has led some workers to propose a hierarchical *ansatz* in which the N-point correlation functions obey a scaling relation (see Balian & Schaeffer, 1989)

$$\xi_N(\lambda \boldsymbol{x}_1, ..., \lambda \boldsymbol{x}_N) = \lambda^{-(N-1)\gamma} \xi_N(\boldsymbol{x}_1, ..., \boldsymbol{x}_N). \tag{1.57}$$

The argument is partly motivated by the fact that gravity is scale-free, subsequently the scaling of the correlation functions in this manner does not seem to be an unreasonable proposition. However, no rigorous theoretical argument for an *anstaz* like equation (1.57) currently exists.

1.3.3 Power spectra

Gaussian random density fields are completely statistically characterised by their 2-point correlation function. Another important quantity related to $\xi(x)$, and in many ways far more useful, is its Fourier counterpart, the power spectral density of fluctuations, or power spectrum for short.

The continuous Fourier transform of the density field is given by

$$\delta(\boldsymbol{k}) = \int d^3x\, \delta(\boldsymbol{x}) e^{i\mathbf{k}\cdot\mathbf{x}} \tag{1.58}$$

with inverse

$$\delta(\boldsymbol{x}) = \int \frac{d^3k}{(2\pi)^3}\, \delta(\boldsymbol{k}) e^{-i\mathbf{k}\cdot\mathbf{x}}. \tag{1.59}$$

Using this definition with equation (1.51) for the 2-point correlation function ($\boldsymbol{x}_2 = \boldsymbol{x}_1 + \mathbf{r}$) gives the important result (the Wiener-Khintchine theorem)

$$\xi(\mathbf{r}) = \int \frac{d^3k}{(2\pi)^3}\, P(k) e^{-i\mathbf{k}\cdot\mathbf{r}}, \tag{1.60}$$

when the power spectrum $P(k)$, is defined by

$$\langle \delta(\boldsymbol{k}_1)\delta(\boldsymbol{k}_2)\rangle = (2\pi)^3\, P(k)\, \delta_D(\boldsymbol{k}_1 + \boldsymbol{k}_2). \tag{1.61}$$

Here the Dirac delta function is defined so as

$$\delta_D(\boldsymbol{k}_1 + \boldsymbol{k}_2) = \int d^3x \exp\Big[\pm i(\boldsymbol{k}_1 + \boldsymbol{k}_2)\cdot\boldsymbol{x}\Big]. \tag{1.62}$$

Equation (1.61) is essentially a statement of statistical homogeneity and isotropy. Homogeneity because of the independence of Fourier modes on different scales through the Dirac delta function, and isotropy in that $P(k)$ only depends upon the magnitude and not the direction of $\boldsymbol{k}$.

The power spectrum is a measure of the amplitude of clustering on a given scale. It can be related to the variance of fluctuations $\langle\delta^2\rangle$, by

$$\langle\delta^2\rangle \equiv \sigma^2 = \frac{1}{2\pi^2}\int dk\, k^2 P(k). \tag{1.63}$$

A useful way of writing the power spectrum is in the form

$$\Delta^2(k) = \frac{1}{2\pi^2}\, k^3\, P(k). \tag{1.64}$$

The quantity $\Delta^2(k)$ represents the contribution to the variance per logarithmic interval in the Fourier domain $d\ln k$, as can be seen by substitution into equation (1.63).

Similar expressions to equation (1.61) can also be written down for the higher order correlation functions in Fourier space. Most notable is the bispectrum $B(\boldsymbol{k}_1, \boldsymbol{k}_2, \boldsymbol{k}_3)$, which comes from

$$\langle \delta(\boldsymbol{k}_1)\delta(\boldsymbol{k}_2)\delta(\boldsymbol{k}_2)\rangle_c = (2\pi)^3\, B(\boldsymbol{k}_1, \boldsymbol{k}_2, \boldsymbol{k}_3)\, \delta_D(\boldsymbol{k}_1 + \boldsymbol{k}_2 + \boldsymbol{k}_3) \tag{1.65}$$

see chapter 4.

It may be necessary in some circumstances, to only consider the density field on scales above a particular *smoothing* length. For example, as noted above the density field of galaxies looks Gaussian on large scales but not when the full effects of gravitational evolution are taken into account. The density field is smoothed by convolution with a window function $W(kR_s)$, where R_s is the smoothing length in real space. In Fourier space the convolution just becomes a multiplication (another reason to work with the power spectrum) so that the variance of the smoothed density field looks like

$$\langle \delta^2 \rangle \equiv \sigma^2(R_s) = \frac{1}{2\pi^2} \int dk\, k^2\, W^2(kR_s)\, P(k). \tag{1.66}$$

1.4 Large-scale structure formation

The inflationary picture sets up a spectrum of fluctuations to the mean density of the Universe that eventually give rise to the structures we see today in the Universe. The most widely accepted picture for how this transformation occurs is through gravitational instability, the accretion of matter onto dense overdense regions ($\delta > 0$) via gravitational interaction. Indeed, following the COBE measurement of anisotropies (Smoot *et al.*, 1992), it is hard to conceive of any other mechanism being relevant for structure formation. The level of fluctuations in the CMB maps extremely well onto the present day galaxy power spectrum with the sole action of gravity (Wright *et al.*, 1992). If other processes were at work (*e.g.* explosions), there would almost certainly have to be some kind of structure suppression taking place as well in order to have consistency.

This section describes the various theoretical tools that one can use in order to explore the evolution of the density field. Inevitably this is an extremely complex

process and so both analytical and numerical models require a large degree of approximation and simplification.

There are two general classes of models for structure formation, defined by the relationship between the primordial perturbations in the matter and in the radiation. In *adiabatic* models, both components are perturbed equivalently so that peaks in the radiation correspond to peaks in the matter. Because of the different evolution of each of these energy densities with a, their exact relationship is

$$\delta_m = \frac{4}{3}\delta_r. \tag{1.67}$$

In *isocurvature* models the perturbations are generated in each component such that the net perturbation to the metric is zero. In this case peaks in the matter correspond to troughs in the radiation and so forth,

$$\rho_m \delta_m = -\rho_r \delta_r. \tag{1.68}$$

Adiabatic perturbations are a generic prediction of inflationary models. Isocurvature perturbations are generated from processes that conserve energy, for example in the formation of topological defects (although isocurvature inflationary models do exist, see Peebles 1999). The currently favoured picture is the adiabatic case and it is with this model that this thesis is principally concerned.

1.4.1 Growth of perturbations in the pre-recombination era

After inflation the Universe is left imprinted with a set of adiabatic density perturbations with near scale invariant power spectrum

$$P_i(k) \propto k^n, \tag{1.69}$$

(Kolb & Turner, 1990; Liddle & Lyth, 1993). Up to z_{eq} most of the energy density is in the radiation component, beyond this epoch the Universe becomes matter dominated. It is important to understand how the primordial power spectrum propagates up to z_{rec} since this is the first epoch at which it becomes measurable (in the CMB).

The following argument is qualitative and intended as a summary, most of the details follow from the analysis in §1.4.2. The arguments are represented schematically in figure 1.5

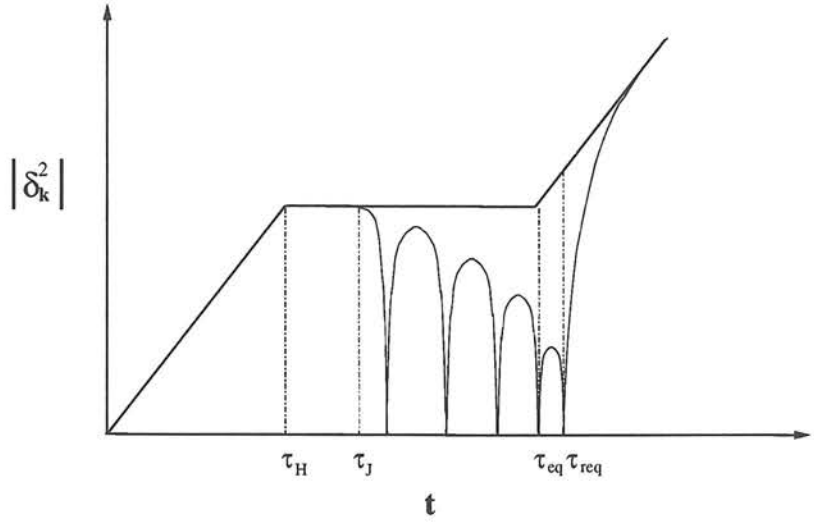

Figure 1.5: Cartoon illustrating the important points in the evolution of a perturbation of size $\lambda = 2\pi k$ (not draw to scale). The perturbation grows in amplitude until τ_H when it enters the Hubble horizon. Subsequently it is stagnated by the Meszaros effect. Baryonic perturbations begin to behave like acoustic waves once inside the Jeans scale at τ_J. They are also damped due to the random walking of the radiation component. The cold dark matter perturbations begin to grow again once $\rho_m = \rho_r$ at τ_{eq}, for the baryonic perturbation this does not happen until recombination at τ_{rec}

First consider the cold collisionless matter component and a fluctuation of scale λ. When $\lambda > R_H$, causal processes do not effect the perturbation. Subsequently it sees only its own overdensity and collapses (δ_λ grows) like a closed universe. Once λ passes inside the Hubble radius its growth becomes stagnated by the Meszaros effect (Meszaros, 1974) as long as the Universe remains radiation dominated. At z_{eq} the perturbation carries on growing once more.

For a baryonic perturbation on the same scale, the situation is more complicated. Again, as for the collisionless case, when λ is superhorizon sized the overdensity collapses. When λ enters the horizon its growth is again suspended. However, when λ becomes less than the Jeans length, λ_J, it behaves like an acoustic wave and oscillates. This is because of the pressure support in the coupled photon-baryon fluid; the natural tendency of the overdensity is to collapse under gravity, however as the baryons begin to fall into their potential wells, radiation pressure forces them back out again if the fluctuation is smaller than λ_J. A further effect acting on the baryonic perturbation is Silk damping (Silk, 1968) which acts to

diffuse the perturbation due to the random walking of photons. Eventually at z_{rec}, the photons and baryons decouple and the perturbation is left free to grow again.

These effects can be summarised in terms of the power spectrum by the *transfer function* $T(k)$. The power spectrum after the epoch of recombination is given by

$$P(k) = T^2(k)P_i(k). \tag{1.70}$$

The transfer function takes care of all the above effects and is specific to a particular energy densify component. Calculation of transfer functions is complicated in practice, although fitting formulae and computer codes are available, see Bardeen *et al.* (1986) and Seljak & Zaldarriaga (1996) for more details.

1.4.2 Eulerian perturbation theory

Cosmological perturbation theory is a simplistic, but successful attempt to describe the evolution of small density fluctuations against the background of an expanding universe. The evolutionary differential equations, whose solution we will seek via a perturbative expansion, may be obtained in two ways: firstly from a microscopic viewpoint, making use of the Vlasov equation for a system of particles; secondly from the macroscopic picture of a perfect, non-viscous, fluid. In either case we are only interested in large-scale properties of the system, ensuring that gravitation is the only relevant force at work. A full treatment of the problem requires application of general relativity (Peebles, 1980; Liddle & Lyth, 1993). However, if we restrict our attention to scales well within the Hubble radius, then we may safely work within the limiting approximation of Newtonian mechanics. We here concentrate upon the fluid description with Newtonian gravity.

The fluid equations

In the Newtonian picture (Peebles, 1980), the fluid responds to a gravitational potential Φ, related to the density through Poisson's equation

$$\nabla^2_{\mathbf{r}}\Phi(\mathbf{r},t) = 4\pi G\, a(t)^2 \rho(\mathbf{r},t), \tag{1.71}$$

where a is the scale factor and G is the universal gravitational constant. We can adapt Poisson's equation to include a pressure term by "borrowing" a result from

the full relativistic treatment. In a sense then, the following should strictly be regarded as a *quasi*-Newtonian derivation. The Poisson equation becomes

$$\nabla_{\mathbf{r}}^2\Phi(\mathbf{r},t) = 4\pi G\, a(t)^2\Big(\rho(\mathbf{r},t) + 3p(\mathbf{r},t)/c^2\Big), \tag{1.72}$$

with p the pressure. The derivatives are with respect to the proper distance $\mathbf{r}$. In an expanding universe, the proper separation of two fundamental observers grows with time like

$$\mathbf{r} = a(t)\boldsymbol{x}, \tag{1.73}$$

where $\boldsymbol{x}$ is the comoving distance. Under the influence of the gravitational potential the fluid behaves according to Euler's equation,

$$\left(\frac{\partial \mathbf{u}(\mathbf{r},t)}{\partial t}\right)_{\mathbf{r}} + \Big(\mathbf{u}(\mathbf{r},t)\cdot\boldsymbol{\nabla}_{\mathbf{r}}\Big)\mathbf{u}(\mathbf{r},t) = -\frac{1}{\rho(\mathbf{r},t)}\boldsymbol{\nabla}_{\mathbf{r}}p(\mathbf{r},t) - \boldsymbol{\nabla}_{\mathbf{r}}\Phi(\mathbf{r},t), \tag{1.74}$$

and the continuity equation

$$\left(\frac{\partial \rho(\mathbf{r},t)}{\partial t}\right)_{\mathbf{r}} + \boldsymbol{\nabla}_{\mathbf{r}}\cdot\Big(\rho(\mathbf{r},t)\mathbf{u}(\mathbf{r},t)\Big) = 0. \tag{1.75}$$

The proper velocity $\mathbf{u}(\mathbf{r},t)$, has two contributions,

$$\mathbf{u} = \frac{d\mathbf{r}}{dt} = \dot{a}\boldsymbol{x} + a\dot{\boldsymbol{x}}. \tag{1.76}$$

The first term $\dot{a}\boldsymbol{x}$, is just the Hubble expansion (Hubble flow). The second term, called the peculiar velocity $\boldsymbol{v} = a\dot{\boldsymbol{x}}$, represents motion out of the Hubble flow caused by the gravitational interactions of elements within the fluid.

The analysis is simplified by transforming to the comoving reference frame. In this case the time derivatives become

$$\left(\frac{\partial}{\partial t}\right)_{\mathbf{r}} \to \left(\frac{\partial}{\partial t}\right)_{\mathbf{x}} - \frac{\dot{a}}{a}\boldsymbol{x} \tag{1.77}$$

whereas spatial derivatives obey

$$\boldsymbol{\nabla}_{\mathbf{r}} \to \frac{1}{a}\boldsymbol{\nabla}_{\mathbf{x}}. \tag{1.78}$$

The Euler and continuity equations in the comoving frame are then

$$\frac{\partial \boldsymbol{v}}{\partial t} + \frac{1}{a}(\boldsymbol{v}\cdot\boldsymbol{\nabla})\boldsymbol{v} + \frac{\dot{a}}{a}\boldsymbol{v} = -\frac{1}{\rho a}\boldsymbol{\nabla}p - \frac{1}{a}\boldsymbol{\nabla}\phi \tag{1.79}$$

$$\frac{\partial \rho}{\partial t} + \frac{3\dot{a}}{a}\rho + \frac{1}{a}\boldsymbol{\nabla}\cdot(\rho\boldsymbol{v}) = 0, \tag{1.80}$$

assuming that all terms are functions of $\boldsymbol{x}$ and t unless otherwise stated. As a further simplification we subtract the contribution to the potential from the homogeneous background. The source for the new potential ϕ is then the fluctuation in ρ about the mean, namely δ from §1.3.2. Using the first of the Friedmann equations, (1.22), with mean matter density $\bar{\rho}$, Poisson's equation becomes

$$\nabla^2\phi = 4\pi G a^2(\rho - \bar{\rho}), \qquad \phi = \Phi + a\dot{a}x^2 \tag{1.81}$$

The evolution equation for $\delta(\boldsymbol{x}, t)$ comes from multiplying equation (1.79) by ρ, equation (1.80) by $\boldsymbol{v}$ and adding the two together. The divergence of the resulting expression is

$$\begin{aligned} \frac{\partial^2\delta}{\partial t^2} + 2\frac{\dot{a}}{a}\frac{\partial\delta}{\partial t} &= \frac{1}{a^2\bar{\rho}}\nabla^2 p + \frac{1}{a}\boldsymbol{\nabla}\cdot(1+\delta)\boldsymbol{\nabla}\phi \\ &+ \frac{1}{a^2}\frac{\partial^2}{\partial x_i \partial x_j}\left[(1+\delta)v_i v_j\right]. \end{aligned} \tag{1.82}$$

In terms of the density contrast, the continuity and Poisson equations are

$$\frac{\partial\delta}{\partial t} + \frac{1}{a}\boldsymbol{\nabla}\cdot(1+\delta)\boldsymbol{v} = 0 \tag{1.83}$$

$$\nabla^2\phi = 4\pi G a^2\bar{\rho}\delta. \tag{1.84}$$

Equations (1.82), (1.83) and (1.84) describe the evolution of perturbations in an expanding universe.

Linear perturbation approximation

The system of equations for $\delta(\boldsymbol{x}, t)$ may be solved by making use of the *perturbation expansion.* We let

$$\delta(\boldsymbol{x}, t) = \delta_1(\boldsymbol{x}, t) + \delta_2(\boldsymbol{x}, t) + \ldots \tag{1.85}$$

where each term is a small fluctuation about the mean density such that

$$\delta_1 \ll 1, \quad \delta_n = \mathcal{O}(\delta_1^n). \tag{1.86}$$

To first, or linear, order we consider just the first term in the expansion. The linearised fluid equations are

$$\frac{\partial^2\delta_1}{\partial t^2} + 2\frac{\dot{a}}{a}\frac{\partial\delta_1}{\partial t} = \frac{1}{a^2\bar{\rho}}\nabla^2 p + 4\pi a^2\bar{\rho}\delta_1, \tag{1.87}$$

$$\frac{\partial \delta_1}{\partial t} + \frac{1}{a}\nabla \cdot \boldsymbol{v} = 0. \tag{1.88}$$

First consider a universe dominated by cold, collisionless matter (CDM) for which $p = 0$. The solution to (1.87) was found by Heath (1977). In general there is a growing and a decaying mode

$$\delta_1(\boldsymbol{x}, t) = D_+(t)\delta_0(\boldsymbol{x}) + D_-(t)\delta_0(\boldsymbol{x}), \tag{1.89}$$

where $\delta_0(\boldsymbol{x})$ is the primordial fluctuation field and the time dependent part is given by

$$D_+(t) = (\dot{a}/a)\int_0^a da'\,(\dot{a}')^{-3}, \quad D_-(t) = \dot{a}/a. \tag{1.90}$$

The solution indicates that to linear order, perturbations grow by a simple *scaling* of the initial conditions in a way dependent upon the spatial curvature through $\dot{a}$. In an Einstein-de Sitter universe the two modes scale like $D_+ = t^{2/3}$ and $D_- = t^{-1}$. The decaying mode is rarely of physical interest as it becomes negligible within a short time.

The effect of a vacuum term can be incorporated into the solution above. A useful fitting formula was presented in Carroll *et al.* (1992) who compare the growth of perturbations as a function of Ω_m and Ω_v at the present epoch to that of the Einstein-de Sitter universe

$$\frac{D(a=1,\Omega_m,\Omega_v)}{D(a=1,\Omega_m=1)} \simeq \frac{5}{2}\Omega_m\left[\Omega_m^{4/7} - \Omega_v + (1+\frac{1}{2}\Omega_m)(1+\frac{1}{70}\Omega_m)\right]^{-1}. \tag{1.91}$$

This expression says that the growth of perturbations is suppressed where $\Omega_m < 1$ compared to the Einstein-de Sitter case. In flat universes with a cosmological constant ($\Omega_m + \Omega_v = 1$) the suppression is not so pronounced as for the open models. However the difference between the two cases is not large, meaning that the dynamical effect of the vacuum on the growth of δ is only small.

Equation (1.87) can be Fourier transformed, resulting in an identical evolution equation for $\delta(\boldsymbol{k}, t)$. The important implication is that in the linear regime, $\delta(\boldsymbol{k}, t)$ grows independantly of scale so that the *linear* power spectrum retains its shape.

For baryonic perturbations the pressure term cannot be neglected. A suitable equation of state for this component is $p(\rho) = p(\bar{\rho}) + c_2^2\bar{\rho}\delta$, with c_s the sound speed. The evolution of baryonic perturbations is most clearly demonstrated in Fourier space. The equation for $\delta(\boldsymbol{k}, t)$ becomes

$$\frac{\partial^2\delta_1(\boldsymbol{k},t)}{\partial t^2} + 2\frac{\dot{a}}{a}\frac{\partial\delta_1(\boldsymbol{k},t)}{\partial t} = \left[4\pi a^2\bar{\rho} - \frac{c_2^2k^2}{a^2}\right]\delta(\boldsymbol{k},t), \tag{1.92}$$

which behaves differently depending upon k. The *Jeans length* is defined as the scale ($\lambda = 2\pi/k$) for which the terms on the RHS of equation (1.92) equate

$$\lambda_J = c_s\left(\frac{\pi}{G\bar{\rho}a^2}\right)^{1/2}. \tag{1.93}$$

For modes where $\lambda > \lambda_J$, equation (1.92) looks similar to the collisionless case, subsequently the perturbations collapse under their own self gravity in a manner close to that discussed above. When $\lambda > \lambda_J$ however, equation (1.92) describes the propagation of waves with velocity c_s. In this regime the perturbations do not have enough mass to counteract the build up of pressure and oscillate like acoustic waves.

For matter perturbations in the background of a uniform, radiation component, the evolution of δ is very different. Solutions were first obtained by Meszaros (1974). If the independent variable in equation (1.92) is changed from t to $y \equiv \rho_m/\rho_r = a/a_{eq}$, where a_{eq} the scale factor for matter-radiation equality, then the matter perturbations evolve according to

$$\frac{\partial^2\delta_1}{\partial y^2} + \frac{2+3y}{2y(1+y)}\frac{\partial\delta_1}{\partial y} - \frac{3}{2y(1+y)}\delta = 0, \tag{1.94}$$

for zero spatial curvature[5]. The solution for the growing mode is

$$D(t) = y + 2/3 \tag{1.95}$$

During radiation domination, $y \ll 1$ and the growth of the perturbation is effectively suspended (the Meszaros effect). In the matter dominated phase, $y \propto a$ and growth maps onto the normal Einstein-de Sitter solution.

The linearised continuity equation can be used to obtain an expression for the velocity field of collisionless matter. Fourier transforming equation (1.88) gives, using the solution to equation (1.87)

$$\boldsymbol{v}(\boldsymbol{k},t) = -\frac{i\boldsymbol{k}}{k^2}\, aHf\,\delta(\boldsymbol{k},t). \tag{1.96}$$

The inverse transform is

$$\nabla\cdot\boldsymbol{v}(\boldsymbol{x},t) = -aHf\,\delta(\boldsymbol{x},t)$$

[5]this is most appropriate since the epoch of radiation domination occurs at early times for which $\Omega(a) \sim 1$.

or equivalently

$$\boldsymbol{v}(\boldsymbol{x},t) = -\frac{1}{4\pi}aHf\,\boldsymbol{\nabla}\int\frac{d\boldsymbol{x}'\delta(\boldsymbol{x}')}{|\boldsymbol{x}-\boldsymbol{x}'|}. \tag{1.97}$$

The parameter $f \equiv (a/D)(dD/da)$ contains important information about the mass density of the Universe. Peebles (1980) gives the useful fitting formula

$$f \simeq \Omega_m^{0.6}. \tag{1.98}$$

This is interesting since it implies that comparison of the galaxy velocity field with the density field should provide an estimate of the mass density parameter. Lastly, equation (1.97) indicates a relationship between the linear peculiar velocity and the peculiar gravity fields, where $\boldsymbol{g} = -\boldsymbol{\nabla}\phi$;

$$\boldsymbol{v} = \frac{Hf}{4\pi a\bar{\rho}G}\boldsymbol{g}. \tag{1.99}$$

1.4.3 Lagrangian perturbation theory

In Lagrangian perturbation theory one follows the trajectories of small elements of the fluid as they move under the influence of the potential ϕ according to the fluid equations. The fluid elements are labeled according to their initial *Lagrangian* positions $\boldsymbol{q}$. The displacement from $\boldsymbol{q}$ at a given time is denoted by the vector $\boldsymbol{\Psi}(\boldsymbol{q},t)$ so that the *Eulerian* comoving position is

$$\boldsymbol{x}(t) = \boldsymbol{q} + \boldsymbol{\Psi}(\boldsymbol{q},t). \tag{1.100}$$

If the displacements obey continuity then the density at a given point in the trajectory of a particle that started at $\boldsymbol{q}$ will be given by

$$\rho[\boldsymbol{x}(\boldsymbol{q})] = \rho(\boldsymbol{q})\left|\frac{\partial x_i}{\partial q_j}\right|^{-1}, \tag{1.101}$$

where the initial density $\rho(\boldsymbol{q})$ is just the background $\bar{\rho}$.

To chart the evolution of ρ, a similar approach can be adopted to the Eulerian case in that we suppose the displacement vector can be expanded in a perturbation series

$$\boldsymbol{\Psi}(\boldsymbol{q},t) = \boldsymbol{\Psi}_1(\boldsymbol{q},t) + \boldsymbol{\Psi}_2(\boldsymbol{q},t) + ... \tag{1.102}$$

The first order solution to this problem was due to Zel'dovich (1970). In the linear case the displacement can be decomposed into temporal and spatial parts,

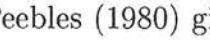

$\Psi_1(\boldsymbol{q},t) = D(t)\Psi_1(\boldsymbol{q})$. Upon using the continuity equation it follows that

$$\begin{aligned} \boldsymbol{v} = a\dot{\boldsymbol{x}} &= -a\dot{D}(t)\Psi_1(\boldsymbol{q}) \\ &\quad -aHf\Psi_1(\boldsymbol{q},t), \end{aligned} \tag{1.103}$$

where $D(t)$ is just the growing mode solution for the Eulerian case. The Jacobian for the transformation $\boldsymbol{q} \rightarrow \boldsymbol{x}$ can be expanded

$$\left|\frac{\partial x_i}{\partial q_j}\right| = \left|\delta_{ij} + \frac{\partial \Psi_i}{\partial q_j}\right|, \tag{1.104}$$

which defines the deformation tensor. The deformation tensor can be diagonalised by choice of a suitable new set of coordinates, in which case the density is

$$\rho = \bar{\rho}\prod_{i=1}^{3}[1 + D(t)\lambda_i(\boldsymbol{q})]^{-1}. \tag{1.105}$$

This expression provides a neat picture of the structure formation process that fits in extremely well with the observed pattern of large scale structure. The eigenvalues λ_i define the axis along which the fluid is compressed under gravity. The collapse occurs firstly along the direction of largest negative λ resulting in flattened pancake-like structures. The pancakes then compress in the direction of the next largest negative eigenvalue to give filaments and so on.

Zel'dovich's solution is quasi-nonlinear in the sense that it remains a reasonable approximation to the growth of structure even when the perturbations to the density become quite large. In fact in 1D the Zel'dovich solution is exact. The limit in 3D comes when any $\lambda_i = -1/D(t)$, in which case the density diverges to infinity. This limit is known as orbit crossing since it corresponds to the intersection of fluid particles.

1.4.4 Nonlinear models

When the fluctuations in the density begin to grow large, the linear perturbation approximation starts to break down. The obvious next step is to include progressively higher order terms in the perturbation series, solving the full nonlinear evolution equation for $\delta(\boldsymbol{x},t)$ iteratively. For the Eulerian case, this is dealt with in detail in §2.2 up to second order in δ. The inclusion of higher order terms significantly complicates the structure formation picture; whereas in the linear approximation growth is determined by scaling of the density field at a point,

in the nonlinear regime the effect of velocity and tidal effects become important. From the expression for the linear velocity, equation (1.97), we can already see that this involves an integral over the whole field.

Higher order solutions to the fluid equations in the Eulerian picture have been comprehensively studied (Peebles, 1980; Juszkiewicz, 1981; Vishniac, 1983; Fry, 1984; Goroff *et al.*, 1986; Catelan *et al.*, 1995), as have solutions in the Lagrangian picture (Moutarde *et al.*, 1991; Bouchet *et al.*, 1992, 1995). Ultimately however, tracing the evolution of the density field far into the nonlinear regime by any sort of perturbation theory is bound to break down or become intractable at some level. The formation of galaxies and clusters occurs at densities $\delta \gg 1$, and so some form of nonlinear approximation would be useful.

The spherical collapse model

In the *spherical collapse model* the highly nonlinear behaviour of spherical overdensities is inferred by assuming that such a perturbation behaves like an independent overdense universe. The solutions to this problem are well known (Peebles, 1980), it can be shown that when $\Omega = 1$, the proper radius of a spherical overdensity scales with time like

$$\begin{aligned} r &= A(1 - \cos\theta) \\ t &= B(\theta - \sin\theta) \end{aligned} \tag{1.106}$$

which for small values of t give

$$r_L \simeq \frac{A}{2}\left(\frac{6t}{B}\right)^{2/3}\left[1 - \frac{1}{20}\left(\frac{6t}{B}\right)^{2/3}\right]. \tag{1.107}$$

Note that this expression is an approximation. The radius as given by equation (1.106) goes to zero at some finite time, this is not so for equation (1.107). The *linear* density within the spherical region is found by contrasting the density in spheres of radius r_L and r

$$\delta_L \simeq \frac{3}{20}\left(\frac{6t}{B}\right)^{2/3}. \tag{1.108}$$

For early t, the radius grows like $t^{2/3}$ with $\delta \propto r$ as in the Einstein-de Sitter case. There is a turnaround from the Hubble expansion when $\theta = \pi$. At this point the actual density within the sphere is starting to grow large $\delta \simeq 5.55$. The

linear density, inferred from the above is $\delta_L \simeq 1.06$. When $\theta = 2\pi$ the radius of the overdensity goes to zero and subsequently the density diverges. The linear approximation at this time is $\delta_L = 1.69$. In reality the effect of gravity will not collapse the system to a singular point, dissipative effects will eventually slow the evolution down. At some point the system will virialise into a *halo* for which $V = -2K$, with V and K the potential and kinetic energy respectively. This seems a likely endpoint for gravitational collapse, corresponding to $\delta \simeq 147$ and $\delta_L = 1.58$.

The Press-Schechter approach

The theory of Press & Schechter (1974) (PS) makes use of the simple arguments above to calculate the abundance of virialised halos as a function of mass. The number of halos per comoving Mpc in the mass range $M \rightarrow M + dM$ defines the mass function $n(M)dM$. In the PS formalism, halos form via spherical collapse when the smoothed linear density field at a given point crosses the threshold $\delta_c = 1.69$. The smoothing radius defines the mass scale

$$\sigma(M) = \int_{-\infty}^{\infty} \frac{dk}{2\pi^2} P(k)[W(kR)]^2, \tag{1.109}$$

in the notation of §1.3.3.

The number of halos of mass $> M$ can then be found by dividing the fraction of the density field, smoothed on mass scale M, that is above δ_c, by the average volume of the halo, $M/\bar{\rho}$. Specifically, the number in the range $M \rightarrow M + dM$ is

$$n(M)dM = \frac{\bar{\rho}}{M}\frac{d}{dM}F(\delta > \delta_c)\, dM. \tag{1.110}$$

If the smoothed linear density fluctuations form a Gaussian random field of variance $\sigma^2(M)$, then equation (1.110) can be evaluated by integrating the probability distribution for δ above δ_c. The result is usually expressed as

$$n(M)\, dM = \sqrt{\frac{2}{\pi}}\frac{\bar{\rho}}{M}\frac{d\sigma(M)}{dM}\frac{\delta_c}{\sigma^2(M)}\exp\left[-\frac{1}{2}\frac{\delta_c^2}{\sigma^2(M)}\right]dM \tag{1.111}$$

which includes a factor 2 "fudge", presented in the original derivation by PS. In fact the fudge is connected with the way that PS incorrectly counts underdense regions. More detailed derivations can be found in Bond *et al.* (1991) and Peacock & Heavens (1990) who account for the discrepancy naturally for sharp k-space

filtering, although one could argue that the physical meaning of sharp k-space filtering is questionable since halos in real space become infinitely large.

Although seemingly a little *ad hoc*, the Press-Schechter formalism provides a remarkably good fit to the halo mass function from numerical n-body simulations, although a more accurate fit can be found in Sheth & Tormen (1999). The halo picture is a phenomenally successful way to address the statistics of the highly nonlinear density with simple arguments. Recent important applications are to be found in, amongst others, Mo & White (1996), Lacey & Cole (1993), Viana & Liddle (1996), Seljak (2000), Ma & Fry (2000) and Peacock & Smith (2000).

1.5 Overview

This chapter has outlined some of the important elements of the current cosmological model, namely the hot big bang scenario plus various add-ons such as inflation and dark matter. The model is by no means complete since there is much yet to be understood, however a great deal of our ignorance can be summarised in terms of a collection of fundamental parameters. Of particular importance are the overall mean density of the Universe (Ω), the fraction of the energy density made up by baryons, dark matter and cosmological constant/vacuum energy (Ω_b, Ω_{cdm} and Ω_v) and the expansion rate of the Universe (H_0). Also significant are the shape and normalisation of the primordial power spectrum, the present day normalisation of the power spectrum and so forth. Determination of these parameters is of paramount importance in the subject of cosmology today.

Fortunately cosmology has entered something of a data boom in the past decade and the possibility of finally pinning down the values of cosmological parameters has never been more real. One of the most dramatic improvements in the quality and quantity of data has been with galaxy redshift surveys, which play a key role in parameter estimation. The original 3D galaxy catalogues were remarkably sparse by todays standards, for example the slice of the Universe presented by de Lapparent *et al.* (1986) contained the redshifts of only 1100 galaxies. By contrast the Anglo Australian 2-degree Field galaxy redshift survey (2dF; Colless 1998) will contain some 250,000 redshifts by its completion and the Sloan Digital Sky Survey (SDSS; Gunn 1995) will collect over 10^6 redshifts.

The information content of large galaxy, lensing and CMB surveys cannot be

stressed enough. As discussed in §1.4.1, the shape of the density fluctuation power spectrum after recombination depends upon the matter content of the Universe and upon various important physical scales: the size of the Hubble horizon at matter-radiation equality, and the size of the Jeans length at recombination. The slope and amplitude of the power spectrum on large scales, *i.e.* where perturbation growth continued outside the horizon until after equality, directly reflects the primordial spectrum of fluctuation produced during inflation, and the position and amplitude of any acoustic oscillations depends sensitively upon the mass and baryon density. As illustrated by equation (1.97), the galaxy velocity field contains much information about the mean density parameter through the function $f(\Omega_m)$. Also the probability distribution of mass and galaxies on very large scales and the measurement of higher order moments in the CMB temperature anisotropies may be able to place constraints on the degree of non-Gaussianity in the Universe's initial conditions.

For the galaxy distribution, biasing and redshift space effects would seem to represent a significant complication to the estimation of parameters. By way of an example, consider again the linear velocity field as given by equation (1.97), which relates the velocity at a given point to the local linear density fluctuation with a proportionality constant that reflects the mean matter density of the Universe. What is missing from this expression is the relation between mass and galaxies. In reality the velocity $\boldsymbol{v}$ of galaxies is largely determined by the dominant gravitating material, *i.e.* the dark matter. If galaxies trace matter perfectly then there is no problem, however, as discussed in §1.2.2 this is probably not the case. The simplest way to quantify the relation at linear order is with the bias parameter b, defined such that

$$\delta_g = b\delta_m, \tag{1.112}$$

where δ_g is the density field for galaxies and δ_m that for dark matter. This means that the quantity actually measured from the velocity field of galaxies is the *degenerate* combination $f(\Omega_m)/b$. Of course, the actual relation between δ_g and δ_m is almost certainly more complicated than a simple multiplicative factor. The most obvious generalisation is that the exact relation is nonlinear so that b is a function of δ, although far more complicated scenarios can be imagined. This issue is returned to in chapter 3. In fact the biased relationship between mass and galaxies can be taken as a parameterization of our ignorance of the galaxy formation process; determining the nature of this relation is therefore of

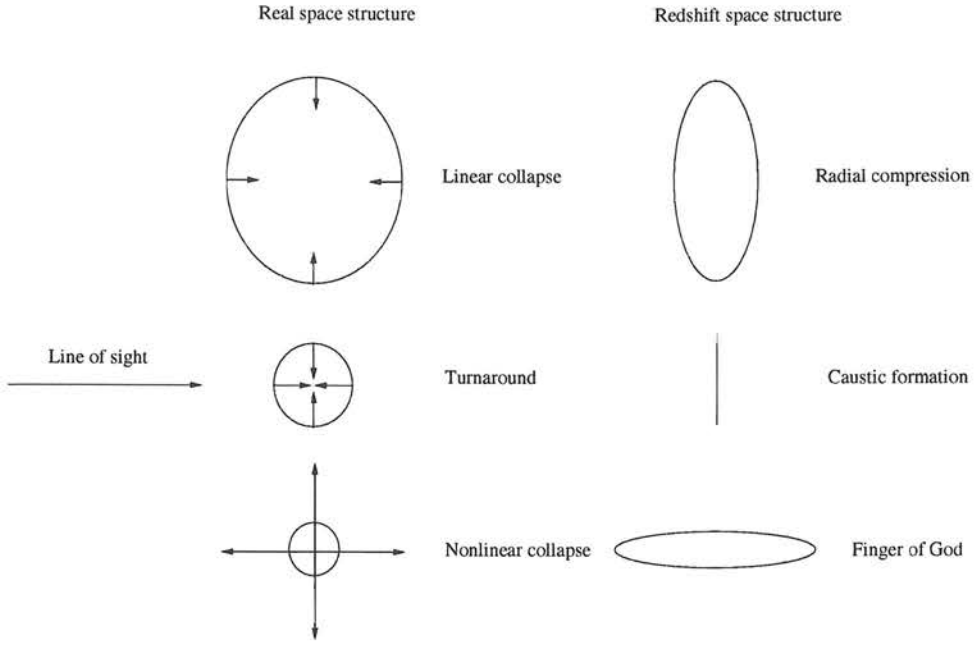

Figure 1.6: Illustration of the redshift space distortion effect. The real space structure is shown on the left and its projection into redshift space on the right. The arrows indicate the size of the peculiar velocities of the galaxies.

considerable importance.

The redshift distortion effect arises as a result of the peculiar motions of galaxies. In 3D galaxy surveys the distances to objects are measured in terms of the redshift. This is a convenient measure since the redshifts of galaxies are relatively easy to determine from the positions of transition lines in their spectra. But the peculiar motion of galaxies due to local gravitational effects introduces a radial distortion in the distance measurement. Galaxies with a peculiar velocity component pointing towards the observer will appear nearer than they really are, while those with velocities pointing away from the observer appear further away. The degree of distortion is related to the magnitude of the peculiar velocity, which is in turn related to the degree of overdensity in the structure the galaxy belongs to. The effect is illustrated in figure 1.6. For mildly overdense structures such as superclusters and large filaments, the effect is a compression along the line of sight, making the region look more compact than it really is. For highly collapsed clusters, the infall velocities of galaxies are large, resulting in a high degree of distortion along the line of sight. These structures were seen in the earliest redshift surveys and became known as Fingers of God. For such highly collapsed regions

the apparent density is decreased.

Redshift distortions have a significant effect on the statistics of galaxy clustering, as first calculated by Kaiser (1987). If not properly modeled the distortions can lead to a significant mismatch between theory and observation. However, if properly accounted for, they can be used to estimate cosmological parameters since the amplitude of the effect depends strongly upon the mass density of the Universe and the bias. This idea has been successfully applied to galaxy redshift surveys by a number of authors using a variety of different approaches. These are not discussed further here, but see Hamilton (1998) and references therein for a review. The most up to date analysis of redshift space distortions is in Tadros *et al.* (1999) and Taylor *et al.* (2000).

1.5.1 Breakdown of thesis

Much of the work in this thesis deals with the distribution of galaxies and dark mass in the Universe. The intended major application is therefore to the next generation of galaxy redshift surveys, although some of the work may be applied to future weak lensing surveys and even the CMB. The main points of interest in this work are how nonlinear evolution, galaxy biasing and redshift space distortions affect the statistics of the matter distribution, with an ultimate goal being to develop new statistical tools for the estimation of parameters from nonlinear cosmic fields.

In chapter 2 a new derivation of the 1-point probability distribution function is presented. The calculation makes use of Eulerian perturbation theory taken to second order in the density δ. Propagation of initial probabilities is performed using the Chapman-Kolmogorov equation from statistical physics, which allows for freedom in the initial conditions and transition probability. An analytical form for the probability generating function is given, from which the skewness and other moments can be inferred. The PDF is compared with the results of numerical simulations and finds favorable agreement. The method is also contrasted with other approximations for the 1-point PDF.

The flexibility of the Chapman-Kolmogorov approach is exploited in chapter 3 for the derivation of the 1-point PDF of galaxies in redshift space. The generating function is derived making use of the methods in chapter 2. This leads to a new result for the skewness of a biased field in redshift space which is found to have

cosmological parameter dependance. The effect of bias and redshift distortion on the shape of the PDF is investigated, and comparisons are made with numerical simulations. Comparisons are also made with an alternative expansion of the PDF, which utilizes the calculation of the redshift space skewness. Lastly a way of discriminating between models that are degenerate in linear theory is given.

In chapter 4 the flow of parameter information into the nonlinear regime is investigated by developing a non-Gaussian generalisation of the Gaussian likelihood method. The Fisher information matrix for non-Gaussian fields is also constructed and a new function, the parameter entropy, introduced. The new methods are applied to a model for a galaxy redshift survey including the effects of nonlinear biasing, redshift distortions and shot noise. Impressive improvements are found for the accuracy of joint parameter estimates over linear theory. Most importantly, incorporating nonlinear terms in the likelihood allows degeneracies between parameters to be broken.

In chapter 5 the results of the thesis are summarised. Some indication as to future applications of the work are also given.

Chapter 2

Nonlinear evolution of the 1-point distribution function

The work in this chapter was done in collaboration with A. N. Taylor. It was first presented in the paper Taylor & Watts (2000).

2.1 Introduction

The standard scenario for the formation of structure in the Universe is via the gravitational amplification of primordial random Gaussian fluctuations generated in the early Universe during an inflationary phase. An attractive feature of this scenario is its predictive power in determining the history of mass perturbations from initial times up until the present day. In principle this should allow one to compare observation with theory. But while detailed predictions at high redshift for the CMB are possible due to their linearity and dependence on well tested laboratory physics, predictions at lower redshift are complicated by nonlinear gravitational evolution and the physics of galaxy formation. One of the goals of cosmology is accounting for the statistical evolution of mass and galaxies up to the present day.

A complete specification of galaxy clustering may only truly be given by the full set of galaxy N-point correlation functions. Such functions form the solution to the so-called Bogoliubov-Born-Green-Kirkwood-Yvon (BBGKY) system of dynamical equations (see Peebles, 1980). This approach, pioneered in the 1970s by Peebles and co workers (Davis & Peebles 1977, Groth & Peebles 1977, Fry & Peebles 1978, Peebles 1980), has met with little success in practice. From a

theoretical perspective, a closed solution to the BBGKY hierarchy equations has never been found, although arguments based upon the scaling *ansatz* discussed in §1.3.2 have been proposed. Observationally, measurements of the correlation functions have been restricted to the lowest few orders.

An alternative description, and the focus of this chapter, may be given by the Probability Distribution Function (PDF) of a random field. Strictly, the PDF at a single spatial location (the 1-point PDF) is investigated, but in general the PDFs are a family of N-point distribution functions for the probability at N positions in space (see §1.3). The random fields of interest are the density fields of both dark matter (this chapter) and galaxies (chapter 3).

The evolution of the 1-point distribution function has been computed by a number of authors using a variety of techniques. Here a new approach is presented, based on propagating the distribution function by the Chapman–Kolmogorov equation from statistical physics. Nonlinear evolution will be incorporated using second-order perturbation theory. In chapter 3 the formalism is developed further to include the effects of galaxy biasing and redshift space distortions (Watts & Taylor, 2000).

2.1.1 The 1-point probability distribution

PDFs are useful in cosmology because, in principle, they encode much of the information contained within the full hierarchy of correlation functions, thus providing valuable information about gravitational evolution and initial conditions. The discrete analogy of the PDF, the counts in cells statistic is reasonably straightforward to measure in galaxy surveys (see Hamilton, 1985; Alimi *et al.*, 1990; Szapudi *et al.*, 1992; Gaztañaga, 1992, 1994; Bouchet *et al.*, 1993; Szapudi *et al.*, 1996; Kim & Strauss, 1998). Furthermore, measurement of the PDF ensures that physical constraints such as the Lyapunov inequalities for the moments, $\langle x^{a+b}\rangle \geq \langle x^a\rangle\langle x^b\rangle$, for any random variable x, are automatically satisfied. This is not necessarily the case for direct measurement of the moments. The PDF also offers a convenient way of dealing with Poisson sampling in the galaxy distribution.

The shape of the PDF is strongly influenced by the nonlinear effects of gravitational instability. A cosmic field that is initially Gaussian random, the generic prediction of most inflationary models, will remain so only when its evolution is

linear. When the evolution becomes nonlinear, the higher-order moments of the field, more correctly the cumulants, become non-zero for the first time resulting in a PDF that may be strongly skewed about its mean and cuspy around its peak.

From a theoretical perspective, the 1-point PDF is a convenient quantity to calculate if it is initially Gaussian. A number of different methods have been developed to calculate its evolution. Fry (1985) first suggested calculating the probability function by applying a hierarchical series suggested by the BBGKY equations to solve for the moment generating function. Bernardeau (1992) derived an exact expression for the evolution of the moment generating function. The generalisation to top-hat filtered density and velocity fields is found in Bernardeau (1994), while Bernardeau (1996) studied the 2-point cumulants and the PDF. However so far a generalisation of these results to include bias and redshift space distortions in the PDF has not been presented.

An approximation for the PDF can also be constructed from the first few cumulants, in the limit of small variance, by the Edgeworth expansion (Juszkiewicz *et al.*, 1995; Bernardeau & Kofman, 1995), where the cumulants have been derived directly from Eulerian perturbation theory (Bouchet *et al.*, 1992) or Lagrangian perturbation theory (Bouchet *et al.*, 1995). This can be extended to redshift space using the Lagrangian perturbation calculations of Hivon *et al.* (1995) for the skewness. Colombi *et al.* (1997) introduced an extended perturbation theory, where the results of perturbation theory are allowed extra freedom and extrapolated to the nonlinear regime.

As well as Eulerian perturbation theory other approximations have also been applied. Kofman *et al.* (1994) and Bernardeau & Kofman (1995) derived the PDF in the Zel'dovich approximation, while Hui *et al.* (2000) extended this to include the effects of redshift space distortions.

A more phenomenological approach was taken by Coles & Jones (1991) who approximated the properties of the PDF by a lognormal distribution while Colombi (1994) suggested an Edgeworth expansion about the lognormal distribution.

2.1.2 Chapter overview

In this chapter second-order perturbation theory is applied to an initially Gaussian distributed density field to calculate the exact second-order characteristic

function. This is then numerically inverse Fourier transformed to yield the 1-point PDF. The method therefore treats the propagation of probabilities exactly.

The chapter is organised as follows. In §2.2 the second-order perturbation theory solution for $\delta(\boldsymbol{x},t)$ is reviewed. The calculation of the evolution of the cosmological probability distribution function and a discussion the transformation to a discrete count distribution is given in §2.3. In §2.4 the results are compared with the those of N-body simulations and with other distributions in §2.5. Conclusions are presented in §2.6. We begin by describing second-order perturbation theory.

2.2 second-order perturbation theory

The fluid equations from §1.4.2 can be solved to second-order in the Eulerian density, $\delta(\boldsymbol{x},t)$ for collisionless matter. This will form the basis of the approximation for nonlinear evolution of the density field. To derive the second-order solution we first expand the density contrast so that

$$\begin{aligned}\delta(\boldsymbol{x},t) &= \delta_1(\boldsymbol{x},t)+\delta_2(\boldsymbol{x},t)\\ &= \delta_1(\boldsymbol{x},t)[1+\varepsilon\delta_1(\boldsymbol{x},t)],\end{aligned} \tag{2.1}$$

where ε is a small factor. This series may be inserted into the nonlinear evolution equation for δ (equation 1.82) to obtain an expression for ε,

$$\begin{aligned}\frac{d^2\varepsilon}{dt^2}+2\left(\frac{1}{D}\frac{dD}{dt}+\frac{\dot{a}}{a}\right)\frac{d\varepsilon}{dt} &= 4\pi G\bar{\rho}\delta_1+\frac{1}{a^2\delta_1}\nabla_i\phi\nabla_i\delta_1\\ &+ \frac{1}{a^2}\nabla_i\nabla_j(v_iv_j).\end{aligned} \tag{2.2}$$

To arrive at this result we have subtracted off the solution to the linear equations and made use of the separability property $\delta_1(\boldsymbol{x},t) = D(t)\delta_0(\boldsymbol{x})$. To proceed further linear theory is used to provide expressions for the velocity field $\boldsymbol{v}$, and potential ϕ. Defining the inverse Laplacian operator

$$\nabla^{-2}\equiv\frac{1}{4\pi}\int\frac{d\boldsymbol{x}'}{|\boldsymbol{x}-\boldsymbol{x}'|}, \tag{2.3}$$

one can write the solution to Poisson's equation

$$\phi(\boldsymbol{x},t) = -4\pi a^2G\bar{\rho}\,\nabla^{-2}\delta_1(\boldsymbol{x},t). \tag{2.4}$$

The expressions for $\boldsymbol{v}$ and $\boldsymbol{g}$ from §1.4.2 can also be recast in the convenient form

$$\boldsymbol{v}(\boldsymbol{x},t) = -afH\,\boldsymbol{\nabla}\nabla^{-2}\delta_1(\boldsymbol{x},t)$$

$$\boldsymbol{g}(\boldsymbol{x},t) = 4\pi a^2 G\bar{\rho}\,\boldsymbol{\nabla}\nabla^{-2}\delta_1(\boldsymbol{x},t). \tag{2.5}$$

Equation (2.2) can then be written entirely in terms of the linear density, giving

$$\begin{aligned}\frac{d^2\varepsilon}{dt^2} + 2\left(\frac{1}{D}\frac{dD}{dt} + \frac{\dot{a}}{a}\right)\frac{d\varepsilon}{dt} &= 4\pi G\bar{\rho}\delta_1 - \frac{4\pi G\bar{\rho}}{\delta_1}\nabla_i\nabla^{-2}\delta_1\nabla_i\delta_1 \\ &+ \frac{\dot{D}}{D}[\nabla_i\nabla_j\nabla^{-2}\delta_1][\nabla^i\nabla^j\nabla^{-2}\delta_1].\end{aligned} \tag{2.6}$$

For an Einstein-de Sitter universe, this expression can be integrated by noting that $D \propto t^{2/3}$ and $4\pi G\bar{\rho} = 2t^2/3$. The solution for ε is then (Peebles, 1980)

$$\varepsilon = \frac{5}{7}\delta_1 - \frac{1}{\delta_1}\nabla_i\nabla^{-2}\delta_1\nabla_i\delta_1 + \frac{2}{7\delta_1}[\nabla_i\nabla_j\nabla^{-2}\delta_1][\nabla^i\nabla^j\nabla^{-2}\delta_1]. \tag{2.7}$$

Since the final distribution function will be dimensionless, it is convenient to work with the convention that $4\pi G\bar{\rho} = 3\Omega H^2/2 = 1$ and the scale factor $a(t) = 1$. The trace free tidal tensor is thus defined as

$$E_{ij}(\boldsymbol{x},t) = \nabla_i\nabla_j\nabla^{-2}\delta_1(\boldsymbol{x},t) - \frac{1}{3}\delta_1(\boldsymbol{x},t)\delta_{ij}, \tag{2.8}$$

and the gradient density field represented by

$$\boldsymbol{\eta}(\boldsymbol{x},t) = \boldsymbol{\nabla}\delta_1(\boldsymbol{x},t). \tag{2.9}$$

In terms of these quantities, the second-order solution for the Einstein-de Sitter universe can be written

$$\delta = \delta_1 + \frac{17}{21}\delta_1^2 - \boldsymbol{\eta}.\boldsymbol{g} + \frac{2}{7}E^2. \tag{2.10}$$

The problem is much more complicated when the spatial curvature is not zero as equation (2.6) cannot be simply integrated. The full solution was first provided by Bouchet *et al.* (1992) using second order Lagrangian perturbation theory and making the transformation from $\boldsymbol{q}$ to $\boldsymbol{x}$ at the end. An Eulerian formalism for the general case was finally developed by Catelan *et al.* (1995), who recast the fluid equations in terms of gravity and velocity potentials. The solution for arbitrary cosmology is given by

$$\delta = \delta_1 + \frac{1}{3}(2-\kappa)\delta_1^2 - \boldsymbol{\eta}.\boldsymbol{g} + \frac{1}{2}(1+\kappa)E^2, \tag{2.11}$$

where $\kappa \approx -3/7\Omega^{-2/63}$ (Bouchet *et al.*, 1992). Note that in general it is not possible to separate out the temporal and spatial parts of the solution for $\delta_n(\boldsymbol{x},t)$ when $n > 2$. The Einstein-de Sitter cosmology is the exception to this.

It is immediately clear from equation (2.11) that to second-order, evolution of density perturbations is far more complicated than the scaling of the field in linear theory. Although the second term in equation (2.11) just acts to enhance the density at every point in a simple manner, the third and fourth terms involve integrals over the whole field. In this way, the second-order growth of a density perturbation depends upon its environment. The term involving the peculiar gravity/velocity appears with a negative sign and hence deals with evacuation of material from void regions. Positive local gradient and velocity vectors point away from underdensities meaning that the net density in such a region decreases further. The tidal contribution acts to distort the perturbations according to the distribution of matter around them.

2.3 The cosmological 1-point distribution function

2.3.1 The distribution function of initial fields

In order to calculate the evolution of the probability distribution function to second-order $P(\delta)$, one must first calculate the joint probability of each of the fields in equation (2.11), $P(\delta_1, \boldsymbol{\eta}, \boldsymbol{g}, \boldsymbol{E})$. All of these quantities are constructed from derivatives of the linear density field. Consequently their Fourier transforms just look like products of $(i\boldsymbol{k})^n$ with $\delta(\boldsymbol{k})$. Since the fields themselves are just a superposition of the Fourier modes, they are guaranteed to be Gaussian quantities. Their joint distribution will then just be a multivariate Gaussian. Defining the parameter vector $\boldsymbol{y} = (\delta_1, \boldsymbol{\eta}, \boldsymbol{g}, \boldsymbol{E})$ the probability is

$$P(\boldsymbol{y}) = \frac{1}{((2\pi)^n \mid \det \boldsymbol{C} \mid)^{1/2}} \exp\left(-\frac{1}{2}\boldsymbol{y}^t \boldsymbol{C}^{-1} \boldsymbol{y}\right), \tag{2.12}$$

where

$$\boldsymbol{C} = \langle \boldsymbol{y}\boldsymbol{y}^t \rangle \tag{2.13}$$

is the covariance matrix. The covariance matrix specifies the 2-point correlations between the components of $\boldsymbol{y}$. If the fields, or some linear combination of them, are uncorrelated then the covariance matrix will be diagonal. The diagonal elements are positive definite quantities – representing the variance of each of the component fields. The elements of the covariance matrix may be calculated with

the following simple recipe (following Bardeen *et al.* 1986, and van de Weygaert & Bertschinger 1996).

Consider the $\langle \eta_i g_j \rangle$ element of the covariance matrix, specifying the correlation between components of the velocity and the gradient density fields. The first stage in evaluating this quantity is to use equations (2.5) and (2.9) to re-cast in terms of the linear density,

$$\langle \eta_i g_j \rangle = \langle \nabla_i \delta_1 \, \nabla_j \nabla^{-2} \delta_1 \rangle. \tag{2.14}$$

Expanding the RHS in terms of its Fourier components this becomes

$$\langle \eta_i g_j \rangle = \int d^3k_1 \int d^3k_2 \frac{[k_1]_i [k_2]_j}{k^2} \langle \delta(\boldsymbol{k}_1) \delta(\boldsymbol{k}_2) \rangle \exp\left[(\boldsymbol{k}_1 + \boldsymbol{k}_2) \cdot \boldsymbol{x}\right]. \tag{2.15}$$

The angled brackets may be placed only around the $\delta(\boldsymbol{k})$ because within each realisation we require that the $\boldsymbol{k}$ and $\boldsymbol{x}$ be fixed, the density is therefore the only random quantity. The mean squared density fluctuation on a given scale is specified by the power spectrum via equation (1.61) from §1.3.3. With the vector identity

$$\int d\Omega \hat{\boldsymbol{k}}_i \hat{\boldsymbol{k}}_j = \frac{4\pi}{3} \delta_{ij} \tag{2.16}$$

the angular parts of the integral in equation (2.15) can be evaluated, leaving

$$\langle \eta_i g_j \rangle = \frac{1}{3} \sigma_0^2 \delta_{ij}. \tag{2.17}$$

The family of variances, σ_m^2, are defined by

$$\sigma_m^2 = 4\pi \int dk P(k) k^{2m+2}. \tag{2.18}$$

A similar calculation can be used to calculate the remaining elements of $\boldsymbol{C}$. Repeating the above procedure for all combinations of $y_i y_j$ gives the following non-zero components of the covariance matrix

$$\begin{aligned}
\langle \delta^2 \rangle &= \sigma_0^2, & \langle \eta_i \eta_j \rangle &= \frac{1}{3} \sigma_1^2 \delta_{ij}, \\
\langle g_i g_j \rangle &= \frac{1}{3} \sigma_{-1}^2 \delta_{ij}, & \langle \eta_i g_j \rangle &= \frac{1}{3} \sigma_0^2 \delta_{ij}, \\
\langle E_{ij} E_{kl} \rangle &= \frac{1}{15} \sigma_0^2 \left(\delta_{ik} \delta_{jl} + \delta_{il} \delta_{jk} - \frac{2}{3} \delta_{ij} \delta_{kl} \right).
\end{aligned} \tag{2.19}$$

The parameter vector can be therefore be cut down to 13 components from 16, they are

$$\boldsymbol{y} = (\delta_1, \eta_x, \eta_y, \eta_z, g_x, g_y, g_z, E_{xx}, E_{yy}, E_{zz}, E_{xy}, E_{xz}, E_{yz}). \tag{2.20}$$

Unfortunately the resulting matrix is not in a particularly convenient form for further calculation. To simplify matters, the 3×3 portion of the matrix containing correlations between the diagonal elements of E_{ij} is diagonalized, making use of the fact that $\boldsymbol{E}$ is trace free. The eigenvectors of the new sub-matrix are

$$\begin{aligned} E_X &= (E_{xx}+E_{yy}+E_{zz})/2 \quad = 0 \\ E_Y &= (E_{xx}-E_{zz})/2 \\ E_Z &= (E_{xx}-2E_{yy}+E_{zz})/2, \end{aligned} \tag{2.21}$$

which are uncorrelated with all other fields but for which

$$\begin{aligned} \langle E_Y E_Y \rangle &= \frac{1}{15}\sigma_0^2 \\ \langle E_Z E_Z \rangle &= \frac{1}{5}\sigma_0^2. \end{aligned} \tag{2.22}$$

The resulting 12×12 matrix can be arranged by row and column interchange into a simple block diagonal form. The action in equation (2.12) can then be readily expanded, giving

$$\boldsymbol{y}^t\boldsymbol{C}^{-1}\boldsymbol{y} = \frac{\delta^2}{\sigma_0^2} + \frac{3}{(1-\gamma_\nu^2)}\left(\frac{\eta^2}{\sigma_1^2} + \frac{g^2}{\sigma_{-1}^2} - 2\gamma_\nu\frac{\boldsymbol{\eta}.\boldsymbol{g}}{\sigma_1\sigma_{-1}}\right) + 15\frac{E^2}{\sigma_0^2}, \tag{2.23}$$

and for the determinant

$$\det\boldsymbol{C} = \frac{20}{3^{10}5^3\pi^4}\sigma_0^{12}\sigma_1^6\sigma_{-1}^6(1-\gamma_\nu^2)^3. \tag{2.24}$$

The correlation parameter, γ_ν, is defined as

$$\gamma_\nu = \frac{\sigma_0^2}{\sigma_1\ \sigma_{-1}}, \tag{2.25}$$

providing a measure of the correlation between the linear velocity and density gradient fields. If a power-law power spectrum with a Gaussian cut-off is assumed, $P(k) \propto k^n e^{-k^2R^2}$, where n is the spectral index and R some arbitrary length scale, then

$$\gamma_\nu = \frac{n+1}{n+3}, \tag{2.26}$$

with the constraint $n > -1$ to insure convergence of the velocity field. The correlation parameter must be positive definite since under gravity matter will be displaced from low to high density regions. The special case of $n \to -1$ for a power-law initial spectra results in $\gamma_\nu = 0$ because the velocity field diverges on small scales. In fact the diverging velocities form an incoherent Gaussian random field which is uncorrelated with the density field (Taylor & Hamilton, 1996).

2.3.2 Propagation of the density distribution function

The distribution function can be propagated to later times by the Chapman-Kolmogorov equation (see for example, van Kampen, 1992),

$$P(\boldsymbol{x}) = \int d\boldsymbol{y}\, W(\boldsymbol{x}|\boldsymbol{y})P(\boldsymbol{y}), \tag{2.27}$$

where $W(\boldsymbol{x}|\boldsymbol{y})$ is the transition probability from $\boldsymbol{x}$ to $\boldsymbol{y}$. In the case of a deterministic process, such as the one considered here, the transition probability reduces to a delta-function restricting the number of possible paths of evolution to one. This transition probability is given by

$$W(\delta|\boldsymbol{y}) = \delta_D[\delta - \delta_1 - \frac{1}{3}(2-\kappa)\delta_1^2 + \boldsymbol{\eta}.\boldsymbol{g} - \frac{1}{2}(1+\kappa)E^2] \tag{2.28}$$

Inserting this into equation (2.27) yields

$$P(\delta) = \langle \delta_D(\delta - \delta(\boldsymbol{y}))\rangle_y. \tag{2.29}$$

where $\delta(\boldsymbol{y})$ is the right hand side of equation (2.11). Hence for deterministic transitions the Chapman–Kolmogorov equation becomes the expectation value of the delta function. This is a well–known result from probability theory (*e.g.* van Kampen, 1992).

Fourier transforming the delta function one finds

$$P(\delta) \equiv \frac{1}{2\pi}\int_{-\infty}^{\infty} dJ\, \mathcal{G}(J)\exp(iJ\delta), \tag{2.30}$$

where

$$\begin{aligned} \mathcal{G}(J) &\equiv \int_{-\infty}^{\infty} d\delta P(\delta)\exp\left(-iJ\delta\right) \\ &= \langle \exp\left(-iJ\delta(\boldsymbol{y})\right)\rangle_y \end{aligned} \tag{2.31}$$

is the characteristic function. In the second line equation (2.29) is used to write the characteristic function as an expectation over all the linear fields $\boldsymbol{y}$. This expression reduces to a set of multivariate Gaussian–type integrals that can be easily evaluated with the well known result

$$\int_{-\infty}^{\infty} dX \exp\left(-AX^2 - BX\right) = \sqrt{\frac{\pi}{A}}\exp\left(-\frac{B^2}{4A}\right). \tag{2.32}$$

Performing all of the integrals yields

$$\mathcal{G}(J) = \Theta(J)\exp\left[-\frac{J^2\sigma_0^2}{2(1+i\alpha_1 J)}\right], \tag{2.33}$$

where

$$\Theta(J) = (1 + i\alpha_1 J)^{-1/2}(1 + i\alpha_2 J)^{-5/2}(1 - i\alpha_3 J + \alpha_4 J^2)^{-3/2}, \tag{2.34}$$

and where the α coefficients are given by

$$\alpha_1 = \frac{2}{3}(2 - \kappa)\sigma_0^2, \quad \alpha_2 = \frac{2}{15}(1 + \kappa)\sigma_0^2,$$

$$\alpha_3 = \frac{2}{3}\sigma_0^2, \quad \alpha_4 = \frac{1}{9}\frac{(1 - \gamma_\nu^2)}{\gamma_\nu^2}\sigma_0^4. \tag{2.35}$$

The probability distribution can then be found by numerically integrating equation (2.30). Equations (2.33), (2.34) and (2.35) are the central results of this chapter.

If the fields in the summation in equation (2.11) remained uncorrelated, then the characteristic function could be reduced to a simple product of the characteristic functions for each term. This is not quite the case here due to the correlations between the velocity and gradient density fields which give rise to the term in α_3 and α_4 in equation (2.34).

Figure 2.1 shows the evolved density distribution function for a range of σ_0. A linear axis for the top plot is used emphasising the peak and a logarithmic axis in the lower plot emphasising the tail of the distribution. As expected, the shape of the distribution is very nearly Gaussian when the variance is small, becoming very rapidly non-Gaussian for higher values. For high variances the probability density does not drop to zero at $\delta = -1$, since in second-order perturbation theory the density field can be negative, generating non-vanishing regions with $\delta \leq -1$. This is also true of linear theory where there are always negative density regions for Gaussian initial conditions. This is a feature of Eulerian distribution functions. Those calculated in Lagrangian perturbation theory, or the lognormal, have positive definite densities at all times.

Figure 2.2 demonstrates the effects of the correlation parameter γ_ν, on the PDF. The main effects are an increase in volume of underdense regions with a corresponding decrease in extremely underdense regions when γ_ν is high. For low γ_ν, the underdensities are smaller and deeper. The physical reason for this is that the $\boldsymbol{\eta}.\boldsymbol{g}$ term in second-order perturbation theory deals with the evacuation of the voids, rather than the amplification of peaks. When γ_ν is low this term is weakened and voids tend to be smaller and deeper, as they would be if the linear

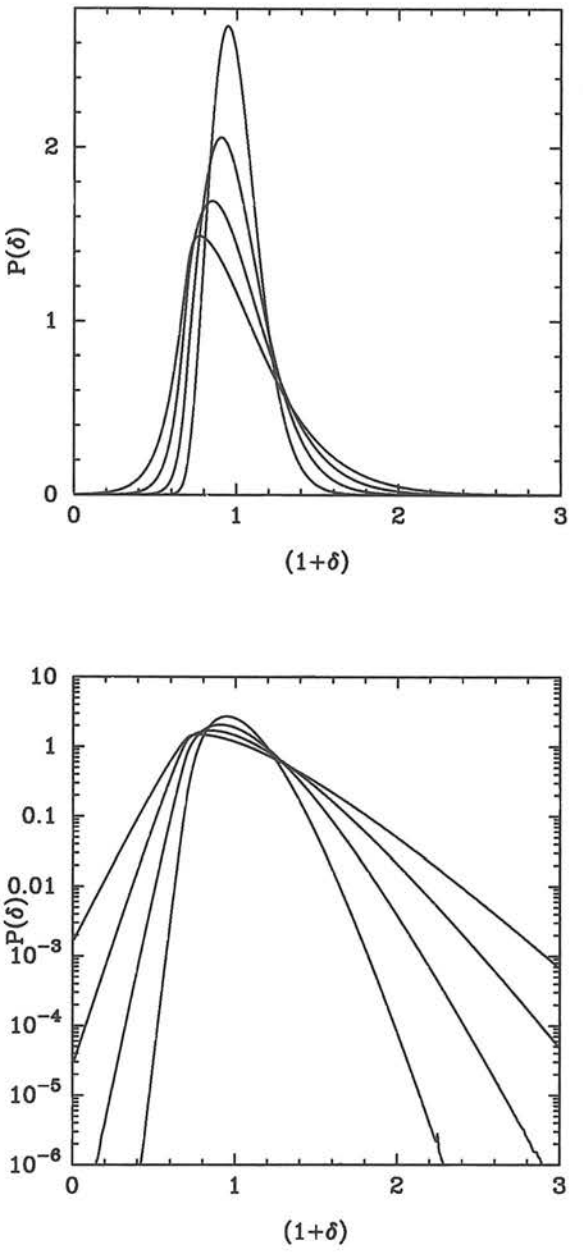

Figure 2.1: The evolution of the 1-point distribution function, $P(\delta)$ calculated from second-order perturbation theory. The variances are $\sigma_0 = 0.15,\ 0.20,\ 0.25,\ 0.3$. In the lower plot a logarithmic axis is used to emphasise the tails of the distribution.

field were extrapolated. Increasing this correlation widens the voids, but makes them shallower to help satisfy the $\delta \geq -1$ constraint. This effect is small for CDM-type initial power spectra where the correlation parameter is in the range

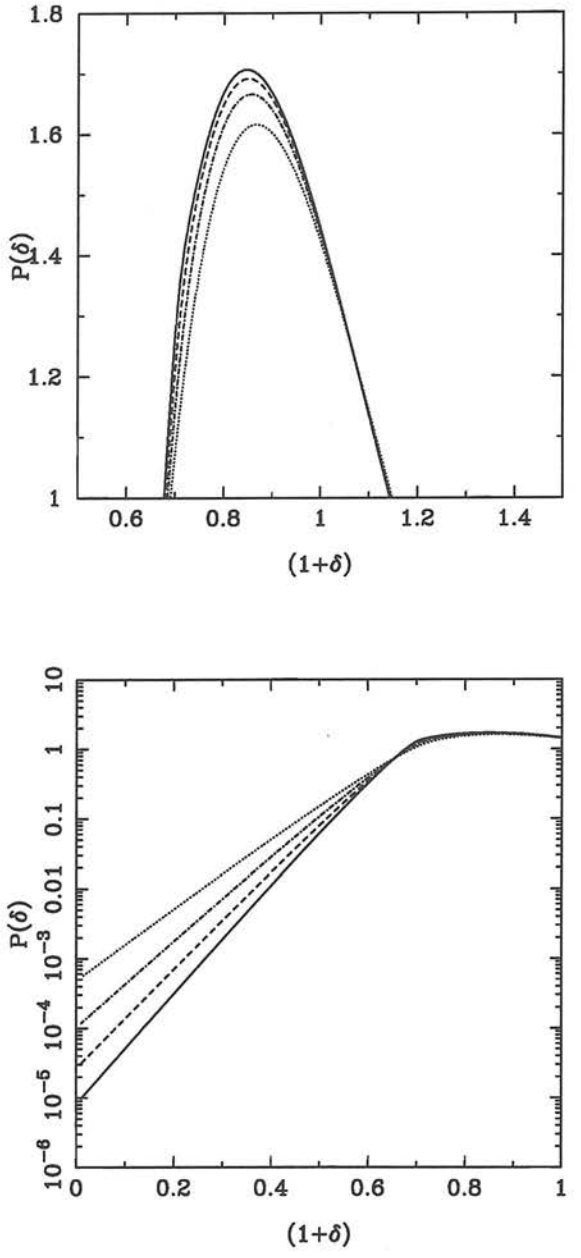

Figure 2.2: The variation in the peak (upper) and tail (lower) of the 1-point density distribution function as a function of the correlation parameter, γ_ν. The values used were $\gamma_\nu = 0.65$ (solid line), 0.55 (dashed), 0.45 (dot-dashed) and 0.35 (dotted). The effect is small for CDM-type initial power spectra where the correlation parameter is in the range $0.55 < \gamma_\nu < 0.65$ over a wide range of scales.

$0.55 < \gamma_\nu < 0.65$ over a wide range of scales.

2.3.3 Skewness from the characteristic function

Since the derived characteristic function is correct to second-order, a useful check is to calculate the variance and skewness to compare with previous estimates. Taking the derivatives of the characteristic function with respect to J and setting J equal to zero yields the moments of the evolved density distribution function,

$$\frac{\partial^n}{\partial[iJ]^n}\mathcal{G}(J=0) = \langle\delta^n\rangle. \tag{2.36}$$

In the literature it is common to express the moments in the form of the moment parameters

$$S_n = \langle\delta^n\rangle_c/\langle\delta^2\rangle^{n-2} \tag{2.37}$$

where $\langle\delta^n\rangle_c$ is the connected or irreducible part of $\langle\delta^n\rangle$.

The irreducible moments, or cumulants, can be generated by

$$\frac{\partial^n}{\partial[iJ]^n}\ln\mathcal{G}(J=0) = \langle\delta^n\rangle_c. \tag{2.38}$$

From this we can calculate the second and third-order connected moments of the distribution function. The differentials are most efficiently calculated using a symbolic mathematics package. The results are

$$S_2 = 1 \tag{2.39}$$

and

$$S_3 = 2(2-\kappa) \xrightarrow{\Omega\to 1} \frac{34}{7} \tag{2.40}$$

to lowest order. This result is well known (Peebles, 1980) and comes directly from perturbation theory. From the equations of §1.3 the lowest order contribution to the skewness is

$$\begin{aligned}\langle\delta^3\rangle_c &= \langle\delta_2\delta_1\delta_1\rangle_c \\ &= \frac{1}{3}(1-2\kappa)\langle\delta_1^4\rangle - \langle\delta_1^2\eta_i g_i\rangle + \frac{1}{3}(1+\kappa)\langle\delta_1^2 E_{ij}E_{ij}\rangle,\end{aligned} \tag{2.41}$$

which we have expanded using equation (2.11). The 4-point correlations can be written in terms of irreducible components using the cumulant expansion theorem, which for Gaussian fields is simply

$$\langle\delta_1\delta_2\delta_3\delta_4\rangle = \langle\delta_1\delta_2\rangle_c\langle\delta_3\delta_4\rangle_c + cyc. \tag{2.42}$$

The 2-point correlations are therefore just those that appear in the covariance matrix of equation (2.12). Using these results along with the definition from equation (2.37) gives the expected value of S_3.

2.3.4 The discrete distribution function

In reality the density field of galaxies is not a continuous function, but a discrete distribution. To account for this it is usual to assume Poisson sampling of the continuous density field as a crude approximation to galaxy formation processes. Any variation is attributed to biased galaxy formation, which modulates the underlying function. This shall be considered further in chapter 3 (Watts & Taylor, 2000).

The continuous density distribution function can be transformed to a discrete form by the expectation

$$P(n) = \frac{\bar{n}^n}{n!}\langle (1+\delta)^n e^{\bar{n}(1+\delta)}\rangle_\delta, \tag{2.43}$$

where $\bar{n}$ is the mean galaxy count and the expectation is taken with respect to the nonlinear density distribution. Expanding this in terms of the characteristic function and taking the expectation we find

$$P(n) = \int_{-\infty}^{\infty} dJ\ G(J)\left(1 - \frac{iJ}{\bar{n}}\right)^{-n-1} \exp(-iJ). \tag{2.44}$$

In the limit $\bar{n} \to \infty$ this returns the continuum distribution where $\delta = n/\bar{n} - 1$. We note that again that the discrete distribution has a non-vanishing value at $n = 0$, $P(n = 0)$, since the probability of finding zero galaxies within a cell is finite. This is the Void Probability Function (White, 1979).

It is also useful to have the generating function for the discrete moments of this distribution $G_n(k)$. Following some straightforward calculation one finds that

$$G_n(k) = G[i\bar{n}(e^{-ik} - 1)] \exp \bar{n}(e^{-ik} - 1). \tag{2.45}$$

The discrete moments can then be found by differentiating $G_n(k)$;

$$\langle \delta^m \rangle = \frac{\partial^m G_n(k=0)}{\partial (ik)^m}. \tag{2.46}$$

Again the connected moments can be found by differentiating $\ln G(k)$ with respect to ik.

2.4 Comparison of results with n-body simulations

In this section a comparison between the theoretical PDF derived above and the counts in cells PDF found from cosmological N-body simulations is given. A version of Hugh Couchman's (1991) Adaptive P^3M code, altered by Peacock & Dodds (1994) to allow simulations of low density open and flat universes, was used.

The simulation volume was a periodic cube of comoving side $200\,h^{-1}$Mpc containing 100^3 particles. A CDM–type linear power spectrum of Gaussian initial perturbations (Bardeen *et al.*, 1986) was chosen, normalised to match the observed abundance of clusters with linear variance given by $\sigma_8 = 0.6\Omega^{-0.53}$ (Viana & Liddle, 1996). The simulation was carried out on a 128^3 Fourier mesh.

To measure the PDF from the numerical simulations, the discrete particle distribution was smoothed with a Gaussian filter of radius R. The PDF was then found from the smoothed density field evaluated on a 128^3 grid. Since the effective radius of the binning grid was much smaller than that of the filter radius a negligible contribution to the smoothing was expected from it.

The choice of variance to use in the model was slightly ambiguous, given that the smoothing was not treated exactly. Hence it was better to match variances rather than smoothing scales. However the variance in second-order perturbation theory is the same as in linear theory so one could use either the linear input variance from the simulations, or take the measured nonlinear variance when making a comparison. In practice it was found that all of the models provided a better fit if the nonlinear variances where used. This is a well know effect and is the basis of the extended perturbation theory approach of Colombi *et al.* (1997).

Figures 2.3 (top) and 2.3 (bottom) show the results of numerical simulations (points) alongside the calculated second-order PDF (solid line), the lognormal model (Coles & Jones 1991, dotted) and the Edgeworth expansion (Juszkiewicz *et al.* 1995, Bernardeau & Kofman 1995; dashed). Each plot shows the PDF for two different variances, $\sigma_0 = 0.2$, smoothed on a scale of $R = 20\,h^{-1}$ Mpc (open circles) and 0.3 (filled squares) smoothed on $13.5\,h^{-1}$ Mpc.

The effects of shot noise were taken into account as shown in §2.3.4 with the mean particle density $\bar{n}$ chosen to coincide with the mean particle count in a

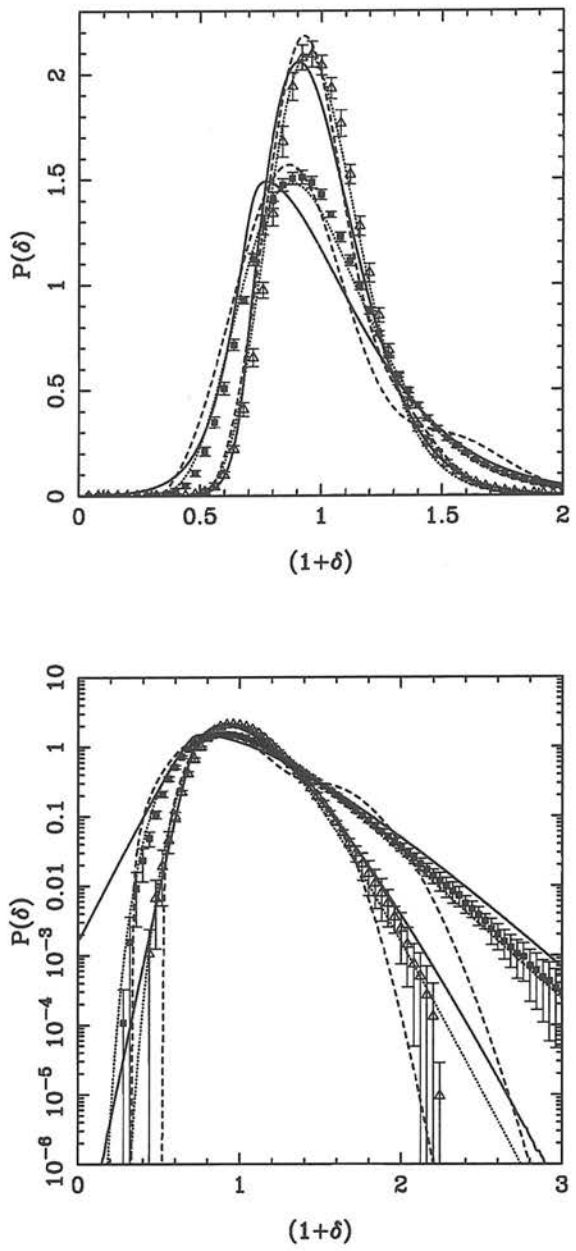

Figure 2.3: Comparison of the second-order PDF (solid line) with the results of N-body simulations (points). The variances are $\sigma_0 = 0.2$ (open triangles) and 0.3 (filled squares). Also plotted are the corresponding distribution functions for the lognormal model (dotted) and Edgeworth expansion (dashed).

boxes with side $l = \sqrt{5}R$. Since $\bar{n}$ was a very large number in all cases, shot noise effects were extremely small. This would not be the case in a real galaxy survey with lower number counts. The remaining factor controlling the shape of

the theoretical PDF was γ_ν. For linear CDM power spectra the calculated γ_ν was approximately 0.55 for a wide range of smoothing radii and it was this value that was used to prepare all the plots in this section.

Error bars on the N-body data points were the standard deviation over 5 independent simulations with identical cosmological parameters.

The linear axes of figure 2.3 (top) show the accuracy around the peak of the distributions while the logarithmic scale of figure 2.3 (bottom) shows the tails of the distributions. At low variance ($\sigma_0 = 0.2$) very good agreement was found between all of the models and the simulations. Overall it was found that the lognormal model fitted the simulations extremely well for all values of the variance around both the peak and the tails. As has been remarked elsewhere, this is regarded as something of a fluke (Bernardeau & Kofman, 1995) and that the lognormal makes a very useful fitting function.

The second-order PDF fits the peak fairly accurately, but tends to be slightly too skewed. This effect becomes greater at higher variance. The tails of the distribution match the N-body simulations rather well, although at high variances and low densities the distribution is too high. This is due to the real distribution being constrained to go to zero at zero density, whereas, as has already been remarked, the second-order PDF is not. In comparison the Edgeworth expansion, taken to second-order (Juszkiewicz *et al.*, 1995; Bernardeau & Kofman, 1995)

$$P_E(\delta) = \left[1 + \frac{1}{6} S_3 \sigma_0 H_3(\delta/\sigma_0)\right] \frac{e^{-\delta^2/2\sigma_0^2}}{\sqrt{2\pi}}, \tag{2.47}$$

where $H_n(x)$ is a Hermite polynomial, is also slightly too skewed and tends to undershoot the high density tail compared to the simulations. At large variance the expansion breaks down and the Edgeworth distribution develops a wiggle on the high density tail. In fact the Edgeworth expansion fares badly even when taken to third-order because the unphysical wiggles are exaggerated and the low density tail becomes more rapidly negative.

2.5 Comparison with other approximations

Finally the PDF derived in this work is compared with other approximations for the 1-point density distribution. Figure 2.4 shows three distributions, the second-order PDF calculation of this chapter (solid line), the Zel'dovich approx-

imation (Kofman *et al.* (1994); dot-dashed line) and the Edgeworth expansion (dotted line) plotted relative to the lognormal distribution. The choice of the lognormal distribution as the point of normalisation is based on the agreement found between it and the N-body simulations.

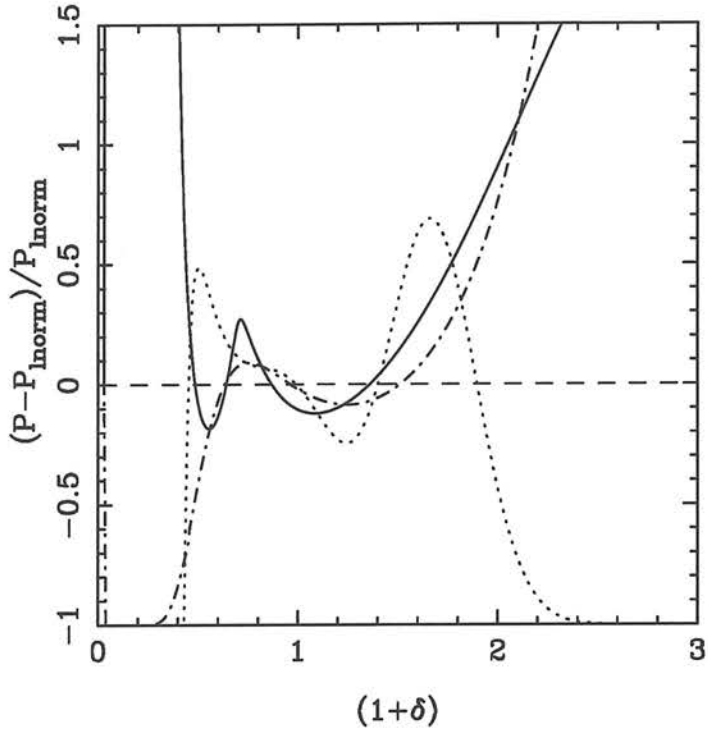

Figure 2.4: Comparison with other distributions. All the models are normalised to the lognormal distribution ($P_{\rm lnorm}(\delta)$; dotted line), since it is found that this best fits the N-body simulation results over a wide range of parameter values. The plot shows the ratio $(P(\delta) - P_{\rm lnorm}(\delta))/P_{\rm lnorm}(\delta)$ for our second-order calculation (solid line), the Zel'dovich approximation (Kofman *et al.* (1994); dot-dashed line) and the Edgeworth expansion (dotted line). The variance used for the comparison was $\sigma_0 = 0.25$.

Over the range $0.4 < \delta < 1.5$ all of the models agree to within a few percent, with the exception of the second-order Edgeworth expansion. But for densities below this regime the second-order PDF overpredicts because the positive density condition is only weakly met. Both the Zel'dovich and Edgeworth models underpredict the probability of low density regions. Above the regime of good agreement our model again overpredicts, again because the high density evolution is over-extrapolated, although not as much as for the Zel'dovich approximation, where caustic formation tends towards a too high distribution. In contrast to both

models the Edgeworth approximation underpredicts the high density regions and develops a large wiggle in the positive density regime.

2.6 Summary

A new method for calculating the nonlinear evolution of the 1-point density distribution function has been presented, using the Chapman-Kolmogorov equation to propagate the probability distribution, and second-order perturbation theory to evolve the density field. This has the advantage over other methods that the resultant probability distribution must be positive definite, and can be readily extended to include the effects of Eulerian deterministic or stochastic bias and redshift space distortions. The main disadvantages of this method are that it is not obvious how to include the effects of smoothing in the final distribution and it is difficult to see how one could extend the evolution of the density field to higher order. However, despite these problems extremely good agreement with numerical simulations is found. Since the characteristic function is derived, the moments and cumulants (connected moments) of the field are easily found, as is the distribution of any local transformations of the density field. The formalism we have introduced can also be used to calculate more complicated 1- and 2-point distributions of cosmologically interesting fields.

Chapter 3

Redshift space evolution of the galaxy distribution function.

The work in this chapter was done in collaboration with A.N. Taylor and published in Watts & Taylor (2000).

3.1 Introduction

One of the central goals of modern cosmology is to gain a quantitative understanding of the nature of the observed galaxy distribution. In order that such an understanding be complete it must incorporate an explanation of both the evolution of large-scale structure in the universe and of the relationship between galaxies and the underlying dark mass.

The standard picture for the origin and evolution of cosmic structures has been discussed in the last two chapters. The arguments hold for the growth of structure in the dark matter, however the picture becomes much more complex when one considers the galaxy distribution. Firstly, the astrophysical processes that govern the formation of the galaxies themselves introduce a nontrivial relationship between the galaxies and the dark matter. This relationship is generally termed galaxy bias. The biasing relation may prove to be simple to describe, depending only upon the local density in dark matter at a given point (*e.g.* Coles, 1993). Conversely it could be extremely complex, depending on the larger scale environment, tidal fields, feedback and entire history of the galaxy formation site. This could lead to non-local (Bower *et al.*, 1993) or non-deterministic forms of biasing (Pen, 1998; Dekel & Lahav, 1999). Secondly, the observed galaxy distribution

is distorted in 3D redshift catalogues due to the line of sight components of the galaxy peculiar motions adding to the general Hubble expansion (Kaiser, 1987). These redshift distortions, if not properly modelled, may lead to misinterpretation when comparing theory with observation.

In chapter 2 a statistical specification of the dark matter density field was presented in terms of the 1-point probability distribution function. It was shown that second order perturbation theory could accurately describe the nonlinear evolution of this quantity starting from Gaussian initial conditions. Other attempts to describe theoretically this evolution have been numerous with the result that, at least for quasi-linear evolution of the matter field, the behavior of the PDF is quite well understood. However, since the the density field of galaxies inferred from a galaxy redshift survey may not be a good representation of the underlying dark matter it is unlikely that the PDF of the dark matter density field is a realistic approximation for that of galaxies. Just as nonlinear gravitational evolution drives the PDF away from Gaussianity, so too will nonlinear bias and redshift distortions. The challenge is to separate out each of the effects and quantify the evolution of the PDF in terms of a few essential parameters.

There have been significantly fewer attempts to calculate the evolution of the PDF in redshift space than in real space. Most notably, Hui *et al.* (2000) extended the work of Bernardeau & Kofman (1995) to calculate the evolution using the Zel'dovich approximation. Despite being an excellent approximation for the nonlinear gravitational dynamics Zel'dovich's solution does not produce a good fit to the PDF of N-body simulations. This is principally due to the formation of caustics in the density field at shell crossing. The result for the Zel'dovich PDF is an asymptotic high density tail that falls off like δ^{-3} in both real and redshift space. Tails like these are not observed in simulations.

Another way of incorporating the effect of redshift distortions and bias is to use the Edgeworth expansion (Juszkiewicz *et al.*, 1995; Bernardeau & Kofman, 1995). In this approximation, the PDF is reconstructed from the moments of the field which must be calculated separately using perturbation theory. Such a calculation was done by Juszkiewicz *et al.* (1993) (but see Hivon *et al.* 1995 for more details), who used second order Lagrangian perturbation theory (Bouchet *et al.*, 1995) to map the skewness of an unbiased field into redshift space. They did not, however, try to use the skewness to evolve the PDF via the Edgeworth expansion. Use of the Edgeworth approximation as a tool for constructing the

nonlinear probability distribution of cosmic fields based upon information from only few moments, is returned to in chapter 4.

A potential problem with using the Edgeworth expansion is its tendency to produce unphysical features in the PDF. In particular is the appearance of negative probabilities at low densities and the formation of unphysical "wiggles" in the high density tail of the distribution when the variance and skewness are pushed too far. These problems can be overcome by reconstructing the PDF using a Gamma expansion (Gaztañaga *et al.*, 2000) which shows a good agreement with N-body data in real space. As we shall see, the features in the Edgeworth do not render it a weak approximation, but care must be taken to establish the range of its applicability.

3.1.1 Chapter overview

This chapter makes use of an extension of the formalism developed in chapter 2, where it was shown how the PDF transforms when the matter density field is propagated to second-order. This method is based on an exact propagation of Gaussian initial probabilities using the Chapman-Kolmogorov equation from statistical physics (*e.g.* van Kampen, 1992). In this chapter the approach is developed further to include the transformation to a local, second-order biased galaxy distribution. Second-order Eulerian perturbation theory is also used to describe the mapping into redshift space. A short discussion about how the method can be naturally extended to incorporate a stochastic (or hidden variable) bias is given, although no detailed calculation is performed. The calculation also provides a new analytic solution for the skewness in redshift-space. This result is different to that of Hivon *et al.* (1995) who estimated the skewness by inverse transform of the bispectrum. However they were unable to find a closed-form solution, and did not include the effects of nonlinear galaxy biasing. Here a closed-form solution for the skewness is derived, including second-order bias. It is found that nonlinear bias has a large effect.

The layout of this chapter is as follows. In §3.2 the theory of redshift distortions is outlined and the definition of a model for galaxy bias is given. An account of the new fields that are introduced to second-order in redshift space is also presented. Some of the material discussed in this section draws from definitions in a short appendix at the end of the chapter, which details the second-order

Lagrangian perturbation theory calculation. In §3.3 the derivation of the 1-point PDF is presented. The new result for the skewness, and a discussion of stochastic biasing may also be found here. In §3.4 the various dependencies on cosmological parameters of the shape of the PDF are illustrated. The results are compared with N-body simulations and other approximations in §3.5. Conclusions are given in §3.6 .

3.2 Redshift distortions and biasing in second-order perturbation theory

3.2.1 Second-order perturbation theory

To recap, in Eulerian perturbation theory the density field $\delta(\boldsymbol{x},t)$ at real space comoving position $\boldsymbol{x}$ and time t in a flat universe can be expanded into a series of separable functions;

$$\delta(\boldsymbol{x},t) = \sum_{n=1}^{\infty} \delta_n(\boldsymbol{x},t) = \sum_{n=1}^{\infty} D_n(t)\delta_0(\boldsymbol{x}). \tag{3.1}$$

In curved space this expansion is only separable to second-order. The evolution of $\delta(\boldsymbol{x},t)$ can therefore be traced into the nonlinear regime by solving the fluid and Poisson's equations for each order in the perturbation expansion (Peebles, 1980; Juszkiewicz, 1981; Vishniac, 1983; Fry, 1984; Bouchet *et al.*, 1992, 1995; Catelan *et al.*, 1995);

$$\begin{aligned} \delta &= \delta_1 + \delta_2 \\ &= \delta_1 + \frac{1}{3}(2-\kappa)\delta_1^2 - \boldsymbol{\eta}.\boldsymbol{g} + \frac{1}{2}(1+\kappa)E^2, \end{aligned} \tag{3.2}$$

where

$$\boldsymbol{\eta}(\boldsymbol{x},t) = \boldsymbol{\nabla}\delta_1(\boldsymbol{x},t), \tag{3.3}$$

is the gradient of the linear density field. Using the convention of chapter 2[1], we define

$$\boldsymbol{g}(\boldsymbol{x},t) = -\boldsymbol{\nabla}\nabla^{-2}\delta_1(\boldsymbol{x},t), \tag{3.4}$$

[1]We let $4\pi G\rho_0 = 3/2\Omega H^2 = 1$ and the expansion parameter $a(t) = 1$, since the final distribution function will be dimensionless.

as the linear peculiar gravity field, where ∇^{-2} is the inverse Laplacian. The trace-free tidal tensor is given by

$$E_{ij}(\boldsymbol{x},t) = (\nabla_i\nabla_j\nabla^{-2} - \frac{1}{3}\delta_{ij})\,\delta_1(\boldsymbol{x},t). \tag{3.5}$$

3.2.2 Redshift space distortions

In redshift space, objects appear displaced from their true positions by an amount dependant upon the radial projection of their peculiar velocity vectors. For mildly overdense regions, infall velocities are relatively low. Objects either side of the overdensity appear slightly closer to each other and hence the local density appears exaggerated. For highly overdense regions such as galaxy clusters, the pairwise velocity of galaxies can be extremely large. In redshift space these regions appear stretched along the line of sight, decreasing the local density. See the excellent review by Hamilton (1998) for a full account of redshift distortions and their use for parameter estimation.

Quantitatively, the mapping from real space comoving position to redshift space comoving position is given by (Kaiser, 1987)

$$\boldsymbol{s} = \boldsymbol{x} + \hat{\boldsymbol{x}}u \tag{3.6}$$

where $u = \hat{\boldsymbol{x}} \cdot \boldsymbol{v}(\boldsymbol{x},t)/H_0$ is the projection of the velocity field along the line of sight.

Transforming to redshift space must conserve mass, so the continuity equation may be written as

$$[1+\delta(\boldsymbol{x})]J^{-1}d^3s = [1+\delta^s(\boldsymbol{x})]d^3s \tag{3.7}$$

where J is the determinant of the Jacobian matrix

$$J_{ij} = \frac{\partial s_i}{\partial x_j}. \tag{3.8}$$

Equation (3.7) accounts for the apparent change in density at a point due to the distortions in the positions of objects in redshift space. Note that the redshift space density field δ^s is still a function of $\boldsymbol{x}$. The Jacobian may be expanded into

$$J = \left(1+\frac{u}{x}\right)^2\left(1+\frac{\partial u}{\partial x}\right). \tag{3.9}$$

To simplify the remaining calculation we invoke the distant observer approximation (Kaiser, 1987). In this regime the peculiar motions of objects are small with

respect to their cosmological distance so that $u/x \ll 1$. For this reason we may write, to second-order

$$\delta^s(\boldsymbol{x}) = \delta(\boldsymbol{x}) - u'(\boldsymbol{x}) + u'^2(\boldsymbol{x}) - \delta(\boldsymbol{x})u'(\boldsymbol{x}) \tag{3.10}$$

where $' \equiv \partial/\partial x$. Finally all terms in equation (3.10) are rewritten as functions of the redshift space comoving position $\boldsymbol{s}$. To first-order, differences in the arguments are unimportant, however to second-order they are. To account for the change in position we make use of the Taylor expansion

$$B(\boldsymbol{x}) = B(\boldsymbol{s}) + u(\boldsymbol{s})\frac{\partial}{\partial s}B(\boldsymbol{s}), \tag{3.11}$$

to finally give

$$\delta^s(\boldsymbol{s}) = \delta(\boldsymbol{s}) - u'(\boldsymbol{s}) - [u(\boldsymbol{s})(\delta(\boldsymbol{s}) - u'(\boldsymbol{s}))]'. \tag{3.12}$$

This result is part of a series in u and δ, which carries to higher order,

$$\delta^s = \sum_{n=0}^{\infty} \frac{(-u)^n}{n!}\frac{\partial^n}{\partial s^n}\left(\frac{\delta - u'}{1+u'}\right). \tag{3.13}$$

3.2.3 Galaxy bias

Next we assume that the density field of galaxies, smoothed on some scale R, is some local function of the underlying smoothed field of dark mass. Following Fry & Gaztañaga (1993), the galaxy density field is expanded in powers of δ;

$$\delta_g = \sum_n \frac{b_n}{n!}\delta^n. \tag{3.14}$$

The coefficients in this expansion b_n, are the bias parameters. No assumptions about the biasing function are made other than that it is local and that it may be expanded in a Taylor series. This is a deterministic Eulerian biasing scheme, but can be generalised to a stochastic Eulerian biasing scheme to allow for the hidden effects of galaxy formation (Pen, 1998; Dekel & Lahav, 1999). The discussion in §3.3.3 illustrates how our intrinsically probabilistic approach can be used to incorporate a stochastic Eularian bias. Other alternatives for bias are non-local Eulerian biases (Bower *et al.*, 1993) and Lagrangian biasing schemes, which are intrinsically non-local in Eulerian coordinates. The latter is possibly the most natural to arise from following halos in the Press-Schechter approach

to galaxy formation (Press & Schechter, 1974). The approach in this chapter is more phenomenological and such possibilities are not considered further.

Combining equations (3.13) and (3.14) gives to second-order (Heavens *et al.*, 1998)

$$\delta_g^s = b_1\delta - u' + \frac{b_2}{2}(\delta^2 - \sigma_0^2) + u'^2 - b_1\delta u' - b_1\delta' u + uu'', \tag{3.15}$$

where all quantities are evaluated at $\boldsymbol{s}$.

In order that this expression has the correct expectation value, $\langle\delta_g^s\rangle = 0$, we have set $b_0 = -b_2\sigma_0^2/2$.

3.2.4 New fields in redshift space

Equation (3.15) is finally rewritten in terms of the familiar linear density, gravity and tidal fields to be used in later calculations. Three new fields, appearing as a result of the transformation into redshift space, are also introduced. These arise from the second derivative of the velocity, the u'' term from equation (3.15), and from the second-order development of the velocity field, the u' term. The mapping from $\boldsymbol{q}$ to $\boldsymbol{x}$ together with the perturbative expansion of the displacement field to second order (see the appendix to this chapter and also §1.4.3), implies the relation

$$\begin{aligned} u_1 &= f_1\hat{s}_i\Psi_{1i} \\ u_2 &= f_2\hat{s}_i\Psi_{2i} \end{aligned} \tag{3.16}$$

where the vector $\hat{s}_i$ is co-linear with $\hat{x}_i$, the line of sight vector. All quantities are assumed functions of $\boldsymbol{s}$ and t and the notation Ψ_{ni} labels the i^{th} component of the n^{th} order displacement field. The redshift parameter f_2 is the obvious second-order analogy of f_1, *i.e.*

$$\begin{aligned} f_1 \equiv \frac{d\ln D_1}{d\ln a} &\approx \Omega_m^{3/5} \qquad \text{open universe} \\ &\approx \Omega_m^{5/9} \qquad \text{flat universe} \end{aligned} \tag{3.17}$$

$$\begin{aligned} f_2 \equiv \frac{d\ln D_2}{d\ln a} &\approx 2\Omega^{4/7} \qquad \text{open universe} \\ &\approx 2\Omega_m^{6/11} \qquad \text{flat universe} \end{aligned} \tag{3.18}$$

(Peebles, 1980; Lahav *et al.*, 1991; Martel, 1991; Hivon *et al.*, 1995). The derivatives with respect to x in equation (3.15) can be evaluated as

$$u_1' = f_1\hat{s}_i\hat{s}_j\nabla_j\Psi_{1i}$$

$$\begin{aligned} u_2' &= f_2 \hat{s}_i \hat{s}_j \nabla_j \Psi_{2i} \\ u_1'' &= f_1 \hat{s}_i \hat{s}_j \hat{s}_k \nabla_j \nabla_k \Psi_{1i}. \end{aligned} \tag{3.19}$$

Using the relation $\Psi_i = \nabla_i \nabla^{-2} \nabla_k \Psi_k$ along with equations (3.80), (3.82) and (3.83) from the appendix, these may be written as

$$\begin{aligned} u_1' &= -f_1 \hat{s}_i \hat{s}_j \left(\frac{\delta}{3} \delta_{ij} + E_{ij} \right) \\ u_2' &= \frac{1}{3} f_2 \kappa \hat{s}_j \hat{s}_j \left(\Pi_{ij}^{\delta} + \frac{\delta^2}{3} \delta_{ij} \right) - \frac{1}{2} f_2 \kappa \hat{s}_j \hat{s}_j \left(\Pi_{ij}^{E} + \frac{E^2}{3} \delta_{ij} \right) \\ u_1'' &= -f_1 \hat{s}_j \hat{s}_j \hat{s}_k F_{ijk}. \end{aligned} \tag{3.20}$$

The new dynamical variables required for redshift space are the gradient of the tidal field

$$F_{ijk}(\boldsymbol{s}, t) = \nabla_i \nabla_j \nabla_k \nabla^{-2} \delta_1(\boldsymbol{s}, t), \tag{3.21}$$

and the second-order tidal fields

$$\Pi_{ij}^{\delta}(\boldsymbol{s}, t) = (\nabla_i \nabla_j \nabla^{-2} - \frac{1}{3} \delta_{ij})\, \delta_1^2(\boldsymbol{s}, t), \tag{3.22}$$

and

$$\Pi_{ij}^{E}(\boldsymbol{s}, t) = (\nabla_i \nabla_j \nabla^{-2} - \frac{1}{3} \delta_{ij})\, E^2(\boldsymbol{s}, t). \tag{3.23}$$

A final simplification comes from choosing to work in the plane parallel approximation, which is valid if looking at a small patch of sky. In the plane parallel approximation we remove the spherical symmetry of the problem, working instead in Cartesian coordinates and restricting all distortions to a single axis (z-axis). Projection operators such as $\hat{s}_i \hat{s}_j$ pick out only the z-components of the fields upon which they act. The result for equation (3.15) is

$$\delta_g^s = \delta_{g,1}^s + \delta_{g,2}^s + \Delta_{g,1}^s + \Delta_{g,2}^s, \tag{3.24}$$

where

$$\delta_{g,1}^s = b_1 \delta_1, \tag{3.25}$$

$$\delta_{g,2}^s = b_1 \delta_2 + \frac{b_2}{2} (\delta_1^2 - \sigma_0^2), \tag{3.26}$$

$$\Delta_{g,1}^s = f_1 \left(E_{zz} + \frac{\delta_1}{3} \right), \tag{3.27}$$

$$\begin{aligned} \Delta_{g,2}^s &= \Delta_{g,1}^{s2} + \delta_{g,1}^s \Delta_{g,1}^s - \frac{f_2}{3} \kappa \left(\Pi_{zz}^{\delta} + \frac{\delta_1^2}{3} \right) \\ &+ \frac{f_2}{2} \kappa \left(\Pi_{zz}^{E} + \frac{E^2}{3} \right) - f_1 g_z \left(b_1 \eta_z + f_1 F_{zzz} \right). \end{aligned} \tag{3.28}$$

The first two terms in equation (3.24) deal with the nonlinear evolution and second-order bias, the last two terms bring in the effects of redshift distortions.

The remaining parameter in the second-order model is

$$\kappa \equiv \frac{D_2}{D_1^2} \approx -3/7\Omega^{-2/63} \qquad \text{open universe}$$
$$\approx -3/7\Omega_m^{-1/143} \qquad \text{flat universe} \tag{3.29}$$

(Bouchet *et al.* 1992, see also Catelan *et al.* 1995 and the appendix). Note that the expression for the redshift distorted and biased galaxy distribution, equation (3.24), does not agree with Hivon *et al.* (1995), even taking into account their slightly different projection into redshift space. Hivon *et al.*'s expression does not appear to have the correct expectation value, *i.e.* their quantity $\langle \delta^s \rangle \neq 0$.

3.3 The galaxy distribution function in redshift space

3.3.1 The distribution of initial fields

Following the analysis of chapter 2, the joint probability for the fields in equation (3.15) is sought. For Gaussian initial conditions the distribution function is given by

$$P(\boldsymbol{y}) = \frac{1}{((2\pi)^n \mid \det \boldsymbol{C} \mid)^{1/2}} \exp\left(-\frac{1}{2}\boldsymbol{y}^t \boldsymbol{C}^{-1} \boldsymbol{y}\right), \tag{3.30}$$

where $\boldsymbol{C}$ is the covariance matrix and and where the parameter vector for redshift space is

$$\boldsymbol{y} = (\delta_1, \boldsymbol{\eta}, \boldsymbol{g}, \boldsymbol{E}, \Pi^\delta_{zz}, \Pi^E_{zz}, F_{zzz}). \tag{3.31}$$

Taking the plane-parallel approximation for redshift space distortions represents a significant simplification since any dependence of δ_g^s on the off-diagonal parts of Π^δ_{ij}, Π^E_{ij} and F_{ijk} is removed, reducing the size of the required covariance matrix from 34×34 to 15×15.

Equation (3.30) is an approximation, the variables Π^δ and Π^E are not strictly Gaussian random fields as they are generated from the square of linear fields. However, the definition of these quantities as trace-free makes them uncorrelated with all of the other fields. If it is then assumed that their distribution is Gaussian, as may be expected as a result of the Central Limit Theorem, they become

statistically independent Gaussian fields. To test this Gaussian approximation of the distribution of the Π-fields, random Gaussian realisations of δ-fields were generated, from which Π^{δ}_{zz} could be calculated. From this analysis the distribution $P(\Pi^{\delta}_{zz})$ was estimated and found to be fit well by a Gaussian with variance $\sigma^2(\Pi^{\delta}_{zz}) = 8\sigma_0^4/45$ (see equation 3.32). Later on, in §3.3.4, it shall be seen that these terms do not contribute to the skewness of the final distribution to lowest order. Hence the effects of this approximation will only be apparent in the higher moments and at higher order.

The elements of the covariance matrix can be calculated using a similar prescription to that outlined in the last chapter (§2.3.1). The non-zero terms are found to be

$$\begin{aligned}
\langle \delta^2 \rangle &= \sigma_0^2, \qquad \langle \eta_i \eta_j \rangle = \frac{1}{3}\sigma_1^2 \delta_{ij}, \\
\langle g_i g_j \rangle &= \frac{1}{3}\sigma_{-1}^2 \delta_{ij}, \quad \langle \eta_i g_j \rangle = \frac{1}{3}\sigma_0^2 \delta_{ij}, \\
\langle E_{ij} E_{kl} \rangle &= \frac{1}{15}\sigma_0^2 \left(\delta_{ik}\delta_{jl} + \delta_{il}\delta_{jk} - \frac{2}{3}\delta_{ij}\delta_{kl} \right) \\
\langle \Pi^{\delta}_{zz} \Pi^{\delta}_{zz} \rangle &= \frac{8}{45}\sigma_0^4 \quad \langle \Pi^{E}_{zz} \Pi^{E}_{zz} \rangle = \frac{22}{135}\sigma_0^4 \\
\langle g_i F_{jkl} \rangle &= \frac{1}{15}\sigma_0^2 (\delta_{ij}\delta_{kl} + \delta_{ik}\delta_{jl} + \delta_{il}\delta_{jk}) \\
\langle F_{zzz} \eta_z \rangle &= \frac{1}{5}\sigma_0^2 \qquad \langle F_{zzz} F_{zzz} \rangle = \frac{1}{7}\sigma_1^2.
\end{aligned} \tag{3.32}$$

Evaluating the action of equation (3.30) one finds

$$\begin{aligned}
\boldsymbol{y}^t \boldsymbol{C}^{-1} \boldsymbol{y} &= \frac{\delta^2}{\sigma_0^2} + \frac{3}{(1-\gamma_\nu^2)} \left(\frac{\eta^2}{\sigma_1^2} + \frac{g^2}{\sigma_{-1}^2} - 2\gamma_\nu \frac{\boldsymbol{\eta}.\boldsymbol{g}}{\sigma_1 \sigma_{-1}} \right) \\
&+ 15\frac{E^2}{\sigma_0^2} + \frac{63}{4\sigma_1^2} \left(\eta_z - \frac{5}{3} F_{zzz} \right)^2 \\
&+ \frac{45}{8\sigma_0^4} \left(\Pi^{\delta}_{zz} \right)^2 + \frac{135}{22\sigma_0^4} \left(\Pi^{E}_{zz} \right) 2,
\end{aligned} \tag{3.33}$$

with determinant

$$\det \boldsymbol{C} = \frac{22}{7} \frac{2^5}{3^{15} 5^9} \sigma_0^{32} \sigma_1^2 \frac{(1-\gamma_\nu^2)^3}{\gamma_\nu^6}. \tag{3.34}$$

The correlation parameter is defined in chapter 2

$$\gamma_\nu \equiv \frac{\sigma_0^2}{\sigma_1 \sigma_{-1}}, \tag{3.35}$$

which is the correlation coefficient of the velocity and gradient density fields. For linear CDM power spectra γ_ν is found to lie in the range $0.50 < \gamma_\nu < 0.65$ for

a wide range of scales. The effect of varying γ_ν was discussed in chapter 2 and was found to have a very small effect in the given range. The value $\gamma_\nu = 0.55$ is henceforth adopted for all subsequent plots.

3.3.2 Propagation of the density distribution function

The multivariate Gaussian distribution for initial fields is once again propagated to later times using the Chapman-Kolmogorov equation

$$P(\boldsymbol{\beta}) = \int d\boldsymbol{\alpha} W(\boldsymbol{\alpha}|\boldsymbol{\beta}) P(\boldsymbol{\alpha}), \tag{3.36}$$

where $W(\boldsymbol{\alpha}|\boldsymbol{\beta})$ is the transition probability from the state α to β. For the deterministic transition to the nonlinear redshift space distribution, the probability is a just a delta function

$$W(\delta_g^s|\boldsymbol{y}) = \delta_D \left[\delta_g^s - \delta_1^s - \delta_2^s - \Delta_1^s - \Delta_2^s\right]. \tag{3.37}$$

However, the advantage of using the Chapman-Kolmogorov approach is that is generalizes the change of variables to allow for stochasticity in the transformation between initial and final states. This will be further discussed in §3.3.3.

The probability distribution function for δ_g^s can be written as an expectation over the stochastic variables $\boldsymbol{y}$,

$$P(\delta_g^s) = \left\langle \delta_D(\delta_g^s - \delta_1^s - \delta_2^s - \Delta_1^s - \Delta_2^s) \right\rangle_y. \tag{3.38}$$

The characteristic function for $P(\delta_g^s)$, defined by

$$\mathcal{G}(J) \equiv \int_{-\infty}^{\infty} d\delta_g^s P(\delta_g^s) \exp\left(-iJ\delta_g^s\right) \tag{3.39}$$

and with inverse

$$P(\delta_g^s) = \int_{-\infty}^{\infty} \frac{dJ}{2\pi} \mathcal{G}(J) \exp\left(iJ\delta_g^s\right) \tag{3.40}$$

can be expressed as the expectation value

$$\mathcal{G}(J) = \left\langle \exp -iJ(\delta_1^s + \delta_2^s + \Delta_1^s + \Delta_2^s) \right\rangle_y. \tag{3.41}$$

As in chapter 2, equation (3.41) reduces to a set of Gaussian type integrals which yield the probability generating function $\mathcal{G}(J)$, for a smoothed galaxy density

field in redshift space;

$$\begin{aligned}\mathcal{G}(J) &= \prod_{i=1}^{5}\theta_i^{-1/2}\exp\left[-\frac{1}{2}iJ\sigma_0^2 b_2\right]\exp\left[-\frac{J^2\sigma_0^2N^2}{2\theta_1}\right]\\ &\times \exp\left[-\frac{2}{45}\frac{J^2\sigma_0^2f_1^2}{\theta_3}\left(1-\frac{iJ\sigma_0^2NH}{f\theta_1}\right)^2\right]\\ &\times \exp\left[-\frac{1}{2}J^2\sigma_0^8f_2^2\kappa^2\frac{1379}{1080}\right],\end{aligned} \tag{3.42}$$

where

$$\begin{aligned}\theta_1 &= 1+2iJ\sigma_0^2A\\ \theta_2 &= \left(1+\frac{4}{15}iJ\sigma_0^2B\right)^4\\ \theta_3 &= 1+\frac{4}{15}iJ\sigma_0^2B+\frac{8}{45}iJ\sigma_0^2f_1^2+\frac{8}{45}\frac{J^2\sigma_0^4H^2}{2\theta_1}\\ \theta_4 &= \left(1-\frac{2}{3}iJ\sigma_0^2b_1+\frac{1}{9}J^2\sigma_0^4b_1^2\frac{(1-\gamma_\nu^2)}{\gamma_\nu^2}\right)^2\\ \theta_5 &= 1-i\frac{1}{5}J\sigma_0^2\left(f_1^2-\frac{10}{3}M\right)\\ &+ J^2\sigma_0^4\left[M\frac{(1-\gamma_\nu^2)}{9\gamma_\nu^2}\left(M+\frac{18}{15}f_1^2\right)+\frac{1}{21}\frac{f_1^4}{\gamma_\nu^2}\left(1-\frac{21}{25}\gamma_\nu^2\right)\right]\end{aligned} \tag{3.43}$$

and

$$\begin{aligned}A &= \frac{1}{3}(2-\kappa)b_1++\frac{1}{9}f_1^2+\frac{1}{3}b_1f_1-\frac{1}{9}f_2\kappa+\frac{1}{2}b_2\\ B &= \frac{1}{2}(1+\kappa)b_1+\frac{1}{6}f_2\kappa\\ H &= f_1\left(b_1+\frac{2}{3}f_1\right)\\ M &= b_1(1+f_1)\\ N &= b_1+\frac{1}{3}f_1.\end{aligned} \tag{3.44}$$

The 1-point PDF can then be found by numerical integration of equation (3.40). Equations (3.42) to (3.44) represent the main analytical result of this chapter.

3.3.3 Stochastic Bias Schemes

Instead of the local deterministic prescription for galaxy biasing described by equation (3.14), a stochastic Eularian biasing scheme may instead be imple-

mented. In stochastic biasing (Pen, 1998; Dekel & Lahav, 1999) the relation between the underlying density field of dark matter and the galaxy density field is a random process with joint distribution $P(\delta_g, \delta)$.

If the biasing transition distribution, $P(\delta_g, \delta)$, is assumed to be a bivariate Gaussian of the form

$$\begin{aligned} P(\delta_g, \delta) &= \frac{1}{2\pi[\sigma_b^2 + b_1^2\sigma_0^2(1-r^2)]} \\ &\times \exp -\frac{1}{2}\frac{\delta_g^2 + \delta^2 b_1^2(1+\sigma_b^2/b_1^2\sigma_0^2) - 2rb_1\delta_g\delta}{\sigma_b^2 + b_1^2\sigma_0^2(1-r^2)}, \end{aligned} \tag{3.45}$$

then the galaxy distribution function can be written

$$P(\delta_g) = \langle P(\delta_g, f(\boldsymbol{y}))\rangle_y, \tag{3.46}$$

where $f(\boldsymbol{y}) = \delta_1 + \delta_2$ in real space. The covariances between the fields are given to first order by

$$\langle \delta_g^2 \rangle = b_1^2\sigma_0^2 + \sigma_b^2, \tag{3.47}$$

$$\langle \delta_g \delta \rangle = b_1 r \sigma_0^2, \tag{3.48}$$

where σ_b is the variance of the random component determining galaxy formation and r is the correlation coefficient between the mass and galaxy distribution. The characteristic function for galaxies is then

$$G_{\delta_g}(J) = \int dJ' G_\delta(J') G_{\delta_g,\delta}(J, J') \tag{3.49}$$

where

$$\ln G_{\delta_g,\delta}(J, J') = -\frac{1}{2}(J^2\sigma_0^2 + J'^2(b_1^2\sigma_0^2 + \sigma_b^2) + 2JJ'b_1 r\sigma_0^2). \tag{3.50}$$

Equation (3.49) can be evaluated numerically.

The distribution function of galaxies can also be evaluated by numerically integrating

$$P(\delta_g) = \int_{-\infty}^{\infty} \frac{dJ}{2\pi} \mathcal{G}_\delta(J) P(\delta_g, J) \tag{3.51}$$

where

$$P(\delta_g, J) = \int d\delta e^{iJ\delta} P(\delta_g, \delta) \tag{3.52}$$

is the partially transformed characteristic function. The effects of stochastic bias will not be explored further, but note that the mechanism can be naturally incorporated into the Chapman-Kolmogorov approach. For the remainder of the chapter only the deterministic scheme will be discussed.

3.3.4 Skewness of a biased density field in redshift space

The skewness of the biased redshift space galaxy distribution can be found from the characteristic function $\mathcal{G}(J)$, by differentiation. The moment parameters are defined in redshift space as

$$S_3^s = \frac{\langle (\delta_g^s)^3 \rangle_c}{\sigma_s^4}, \tag{3.53}$$

where σ_s^2 is the linear, redshift space variance of the galaxy density field δ_g^s.

Taking the third derivative and setting $J = 0$ gives the redshift space skewness parameter

$$\begin{aligned} S_3^s b_1^4 F^2 &= 4b_1^3 \left(1 + \frac{2}{3}\beta_1 + \frac{3}{25}\beta_1^2\right) + 3b_2 b_1^2 \left(1 + \frac{\beta_1}{3}\right)^2 \\ &- 2\kappa b_1^3 (1 + \frac{1}{3}\beta_2) \left(1 + \frac{2}{3}\beta_1 + \frac{7}{75}\beta_1^2\right) \\ &+ 2b_1^4 \beta_1 \left(1 + \frac{19}{15}\beta_1 + \frac{3}{5}\beta_1^2\right) + \frac{6}{25} b_1^4 \beta_1^4, \end{aligned} \tag{3.54}$$

where $F(\beta_1)$ is the linear redshift space enhancement factor for the redshifted variance given to lowest order by (Kaiser, 1987)

$$F = 1 + \frac{2}{3}\beta_1 + \frac{1}{5}\beta_1^2 \tag{3.55}$$

and where

$$\beta_1 \equiv \frac{f_1}{b_1}, \qquad \beta_2 \equiv \frac{f_2}{b_1}. \tag{3.56}$$

The variance in redshift space is just

$$\sigma_s^2 = b_1^2 \left(1 + \frac{2}{3}\beta_1 + \frac{1}{5}\beta_1^2\right) \sigma_0^2. \tag{3.57}$$

Equation (3.54) for the galaxy skewness in redshift space is the second major result of this chapter. It is interesting to compare this with the results of Hivon *et al.* (1995) who derived the density skewness in redshift space. Hivon *et al.* derived their result by transforming the redshifted bispectrum but did not find a closed form solution and were left with a term containing an integral that was to be determined numerically. The result in equation (3.54) for the skewness should coincide with that of Hivon *et al.* for the special case of $b_1 = 1$ and $b_2 = 0$, but does not. The differences between the two results may arise from the different approaches, or from the difference in initial expressions for δ_g^s. The origin of the

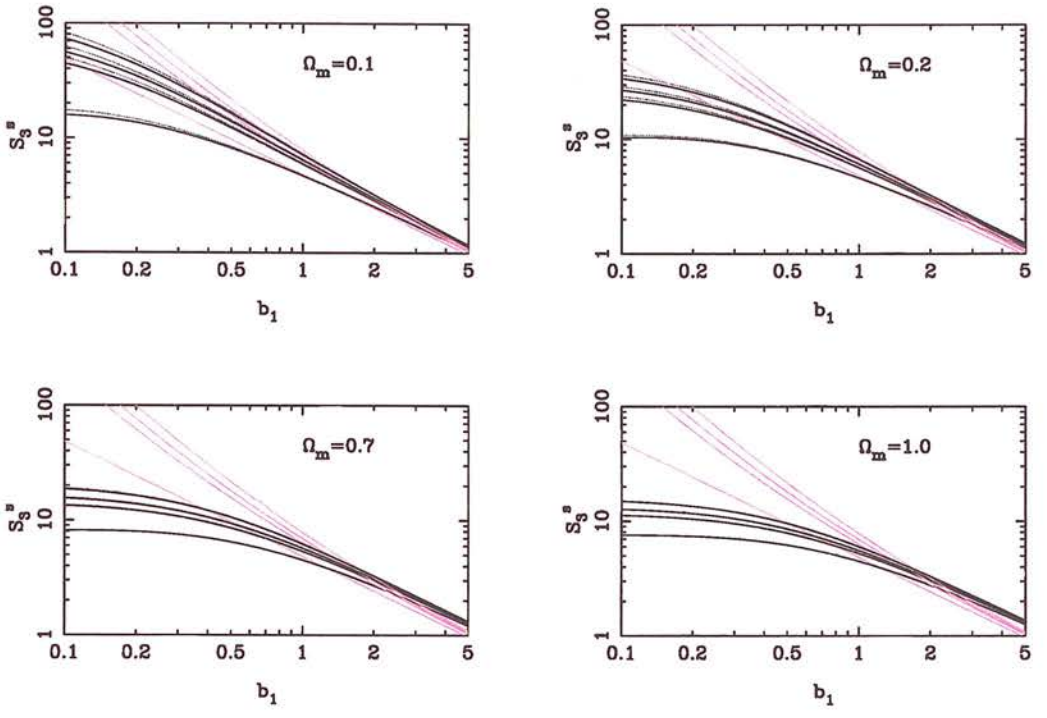

Figure 3.1: Log-log plot of the redshift space galaxy skewness parameter S_3^s, as a function of Ω_m, b_1 and b_2. The panels show increasing values of $\Omega_m = 0.1$, 0.2, 0.7, 1.0. The x-axis is the linear bias parameter b_1. Lines going upwards are the quadratic bias parameter $b_2 = 0.0$, 0.5, 0.7, 1.0. Straight faint lines are the real space skewness S_3, and are independent of Ω_m. Darker curves are for the full redshifted skewness for an open (solid) and flat (dotted) universe.

discrepancy has unfortunately not been traced. Equation (3.54) was verified by a direct calculation of the redshifted galaxy skewness, using equation (3.24) along with the correlators in equation (3.32), to evaluate the quantity $\langle(\delta_g^s)^3\rangle$, as in §2.3.3.

Equation (3.54) displays the hierarchical scaling associated with galaxy clustering. It has already been shown that a local bias will retain a hierarchical form if the underlying field displays hierarchical behavior (Fry & Gaztañaga, 1993) and that the lowest order of perturbation theory reproduces the hierarchical structure. Equation (3.54) would seem to indicate that this structure holds for galaxies in redshift space. This is an important result as it strengthens the claim that if galaxies display a hierarchical scaling then it is consistent that the underlying density field was initially Gaussian distributed and bias is local. Equation (3.54)

suggest that this can be extended as a test of galaxy distributions in redshift space.

In figure 3.1 the skewness parameter S_3^s is plotted as a function of linear bias b_1, for different values of Ω_m and a quadratic bias b_2. An immediate result is that in all the models the redshift space skewness parameter S_3^s, is less than the real-space skewness parameter S_3, until $b_1 > 1.5$. This may seem surprising as one expects the effects of redshift space distortions will tend to make the density field look more evolved along the line of sight. This does happen, but the second-order skewness is dominated by the first-order increase in the variance, so that the ratio $\langle(\delta^s)^3\rangle/\langle(\delta^s)^2\rangle^2$ is smaller than its real space counterpart. This effect was previously observed by Hoyle *et al.* (2000).

Beyond $b_1 \approx 1.5$ the redshift skewness parameter rises above its real space value for all the models. This is because for large values of the linear bias parameter the second-order skewness becomes comparable in magnitude to the redshifted variance.

For $\beta_1 \approx \beta_2 \approx 1$ and $b_1 \approx 1$ the redshifted skewness can be approximated by

$$S_3^s = \frac{1539}{343} b_1^{-0.61} \beta_1^{-0.02} + \frac{75}{49} \frac{b_2}{b_1^2} \beta_1^{-9/14}, \tag{3.58}$$

which is accurate to a few percent. This can be compared with the undistorted skewness (Fry & Gaztañaga, 1993)

$$S_3 = \frac{34}{7} \frac{1}{b_1} + 3\frac{b_2}{b_1^2}. \tag{3.59}$$

Without second-order bias, S_3^s is only weakly dependent on β_1. The main effect of redshift space distortions in this case is to change the dependence on b_1. The second-order bias term, however, has a much stronger dependence on β_1, and has a lower amplitude than the undistorted term when $\beta_1 = 1$.

3.4 The shape of the PDF

The solution for the generating function $\mathcal{G}(J)$, given by equations (3.42) – (3.44) may be integrated numerically without too much difficulty to yield the full distribution function $P(\delta)$. In figure 3.2 the shape of the resulting PDF is shown for a range of values of the parameters b_1, b_2 and Ω_m.

To second-order there are two important quantities working to distort the shape of the PDF from a Gaussian with linear mass variance σ_0. First is the variance of the resulting field which acts to broaden the distribution. Second is he skewness, which produces asymmetry in the PDF about its mean at $\delta = 0$. These two quantities are effected to varying degrees by nonlinear evolution, by nonlinear bias and by the distorting effect of galaxy peculiar motions.

For the plots in figure 3.2 a moderate value was chosen for the linear variance of the underlying dark matter density field, $\sigma_0 = 0.20$. The correlation parameter γ_ν, was 0.55. In the top panel the effect of a purely linear bias is shown with values b_1 =0.7, 1.0 and 1.2 and with $b_2 = 0$. For the lower panel the linear b_1's match those above but in this case $b_2 = 1.0$ for every plot. Each plot shows three different PDFs: one in real space (solid lines), one in redshift space for the case $\Omega_0 = 1.0$ (dotted lines), and a third in redshift space but with $\Omega_0 = 0.3$ (dashed lines). Inset figures show the same plots on logarithmic axis in order to emphasize the tails of the distribution.

In real space and with linear bias only, the shape of the PDF is dominated by the b_1^2 boost to the variance. Where $b_1 > 1$ the change to S_3^s is small and any effect on the shape of the PDF caused by the skewness is masked by the enhanced variance When $b_1 < 1$ there is a more substantial change to S_3^s but in this case the variance becomes small enough that the PDF looks relatively Gaussian regardless of what is happening to the skewness.

To second-order the nonlinear bias parameter b_2, does not alter the variance of the underlying mass density field. The changes to the shape of the PDF when $b_2 \neq 0$ then reflect only the corresponding changes to S_3^s . The real space PDFs appear to peak sharply around $\delta = -1\sigma_s$ with an abrupt drop off of the low density tail to the left of the peak. The high density tail is extended beyond the corresponding case where $b_2 = 0$. With low b_1 the effect of b_2 is most pronounced, causing an increasingly abrupt drop off in $P(\delta)$ on the low density side of the peak. This pronounced effect on the PDF would appear to be an important signature of quadratic bias, which cannot be reproduced by any combination of other parameters.

In redshift space the PDF is dominated by the enhancement of the variance due to linear redshift space distortions. As discussed in §3.3.4 the second-order change in the skewness is less than the linear change in variance resulting in a

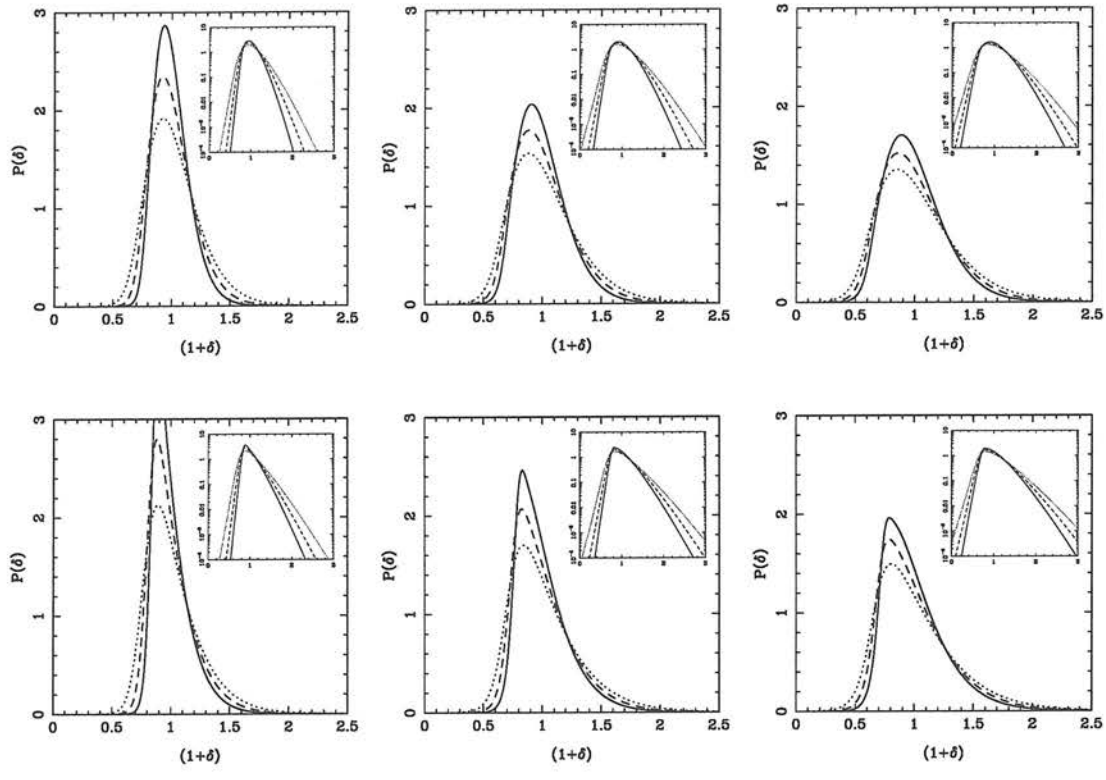

Figure 3.2: The effect of linear and quadratic bias parameters on the 1-point PDF when the variance of the underlying mass density is $\sigma_0 = 0.2$. From left to right the linear bias is $b_1 = 0.7$, 1.0, 1.2. On the top row the second-order bias parameter, $b_2 = 0.0$ and on the bottom $b_2 = 1.0$. In all plots a solid line represents the PDF in real space, a dashed line is for redshift space when $\Omega = 0.3$, and a dotted line for redshift space when $\Omega = 1.0$.

lower skewness parameter S_3^s, in redshift space than in real space. The result for the PDFs is a broader and less asymmetric appearance. This is most clearly seen in the PDFs where $b_2 \neq 0$. For these plots, the sharp peak in $P(\delta)$ around $\delta = -1\sigma_s$ is significantly damped and both the low and high density tails are much shallower than their real space counterparts.

3.5 Comparison of results with N-body simulations

3.5.1 The simulations

In this section the theoretical PDF derived above is compared with the PDF measured from cosmological N-body simulations. For the comparison a version Hugh Couchman's Adaptive P^3M N-body code (Couchman, 1991) was chosen to model the evolution of the dark matter. The simulation volume was a cube of comoving side 200 h^{-1}Mpc with periodic boundary conditions. The initial power spectrum was of CDM form (Bardeen *et al.*, 1986), normalized to match the present day abundance of clusters. The variance on a scale of 8 h^{-1}Mpc when the particle distribution was smoothed with top hat filters was $\sigma_8 = 0.5\ \Omega_m^{-0.5}$ in the final time-step of the simulation. The shape parameter used was $\Gamma = 0.25$, representing the best fit of the CDM power spectrum to galaxy clustering data. The simulation was performed on a 128^3 Fourier mesh with 100^3 particles.

The numerical PDFs were investigated in three sets of circumstances:

- in real space with bias;
- in redshift space without bias;
- in redshift space with bias.

The first two scenarios were trivial to construct from the simulations. For the case of bias in real space, the data was binned and the overdensity estimated from $\delta = (n_p - \bar{n}_p)/\bar{n}_p$, where n_p was the number of particles in a cell and $\bar{n}_p$ was the mean number of particles per cell. The biased distribution was then estimated by the transformation

$$\delta_g = b_1\delta + \frac{b_2}{2}(\delta^2 - \sigma_0^2) \tag{3.60}$$

where σ_0 was the variance on the scale of the binning.

Redshift distortions, in the absence of bias, were calculated using the peculiar velocities of the simulation particles. The distortions were made plane parallel in order to match the approximation from §3.2.2. The resulting particle distribution was smoothed with Gaussian filters of radius R_s. The PDF was then evaluated from the relative abundance of δ across the grid.

Measuring the combined effect of redshift distortions and bias was more difficult. A simple combination of the above methods could not be used, as it was necessary to identify biased galaxies before making the transformation to redshift space. The basic biasing method calculated the biased density field on the grid so that information about individual galaxies was lost. In order to identify individual biased galaxies in the simulation, a population of galaxies was sampled from the simulation particles so that the number of galaxies in a cell n_g, was

$$n_g = \bar{n}_g \left[1 + b_1\delta + \frac{b_2}{2}(\delta^2 - \sigma_0^2)\right]. \tag{3.61}$$

The resulting distribution could then be transformed to redshift space by using the velocity of the galaxies.

The size of the grid was dictated by the need for n_p to be sufficiently larger than n_g so that underdense regions could be enlarged by the bias. Given this constraint we chose to smooth the particle distribution on a coarse mesh of between 9 and 11 cells, with a cell size of $l = 22\,h^{-1}$Mpc and $18\,h^{-1}$Mpc, respectively. As the linear variance was calculated using a Gaussian filter, this corresponds to a smoothing scale of $Rs = l/\sqrt{12} = 6.5$ and $5\,h^{-1}$Mpc. The total number of galaxies was constrained by the requirement that n_g was not larger than n_p in areas of high density, so the total number in the simulation volume was set to $N_g = 5 \times 10^5$.

The errors on the numerical PDFs for the biased and distorted only simulations were taken from the standard deviation over 5 independent realisations of the simulated volume. Errors due to shot noise were incorporated into the theoretical PDF based on the mean density of particles in a cubical cell of side $l = \sqrt{12}R_s$, as discussed in chapter 2. In practice the shot noise contribution was small for simulations due to the high particle density.

In the case of a combined biased and redshift space distorted PDFs the need to sample the galaxies on a coarser mesh meant that the resulting PDF from an individual simulation had a larger scatter from simulation to simulation for the same value of σ_s^2. To avoid this a simulation with a smaller clustering variance was used. A relatively large number of particles could then to be found in each cell. For the case $R_s \approx 5h^{-1}$Mpc there numbered on average 375 galaxies per cell sampled from around 750 simulation particles. When the numerical PDFs were averaged over 7 independent realisations the results were reasonably smooth, although the error bars, again the standard deviation over the 7 realisations, do reflect the scatter.

3.5.2 The Edgeworth Expansion

In addition to the PDF calculated from this work, the PDF reconstructed from the Edgeworth expansion (Juszkiewicz *et al.*, 1995; Bernardeau & Kofman, 1995) was examined, using the redshift space skewness parameter derived in §3.3.4. The distribution function from the Edgeworth expansion is, to second order,

$$P(\nu) = \frac{1}{\sqrt{2\pi}} \left[1 + \frac{1}{3!} H_3(\nu) S_3^s \right] \exp \left[-\frac{1}{2} \nu^2 \right], \tag{3.62}$$

where σ_s^2 is the redshift space galaxy variance given by equation (3.57), S_3^s is the skewness parameter from equation (3.54), $H_n(\nu)$ is an n^{th}-order Hermite polynomial and $\nu = \delta^s / \sigma_s$ is the scaled redshift space density field.

The main difference between the Edgeworth expansion and the model for the PDF discussed above, is that the Edgeworth relies upon two levels of approximation: firstly in the moments, which come from, in this case, a second-order perturbative calculation; and secondly in the Edgeworth series itself, which reconstructs the non-linear PDF by expanding about a Gaussian distribution. The PDF derived in §3.3.2 comes directly from the perturbation theory without any further constraints other than those implicit in the theory itself. In this way the second-order model is perhaps more representative of the perturbation theory and its predictions and limitations. Another dissimilarity between the models, and a problem with trying to derive the PDF to second-order, lies in the fact that second-order perturbation theory does not get the higher moments of the distribution correct. In the calculation from §3.3.2, all of the higher moments exist but have terms missing that would come in in a higher-order calculation. This may strongly affect the shape of the PDF, particularly around the peak. Such problems are not an issue for the Edgeworth and other similar approximations because in these models the cumulants are either put into the series explicitly, or else are zero.

3.5.3 Results

In comparing the models with simulation data the PDF was constructed so that the variance of the distorted, biased density field σ_s^2, was constant for all choices of the parameters Ω, b_1 and b_2. This was arranged by using an appropriate value of σ_0 for each plot. For the case of bias in real space and of no bias in redshift

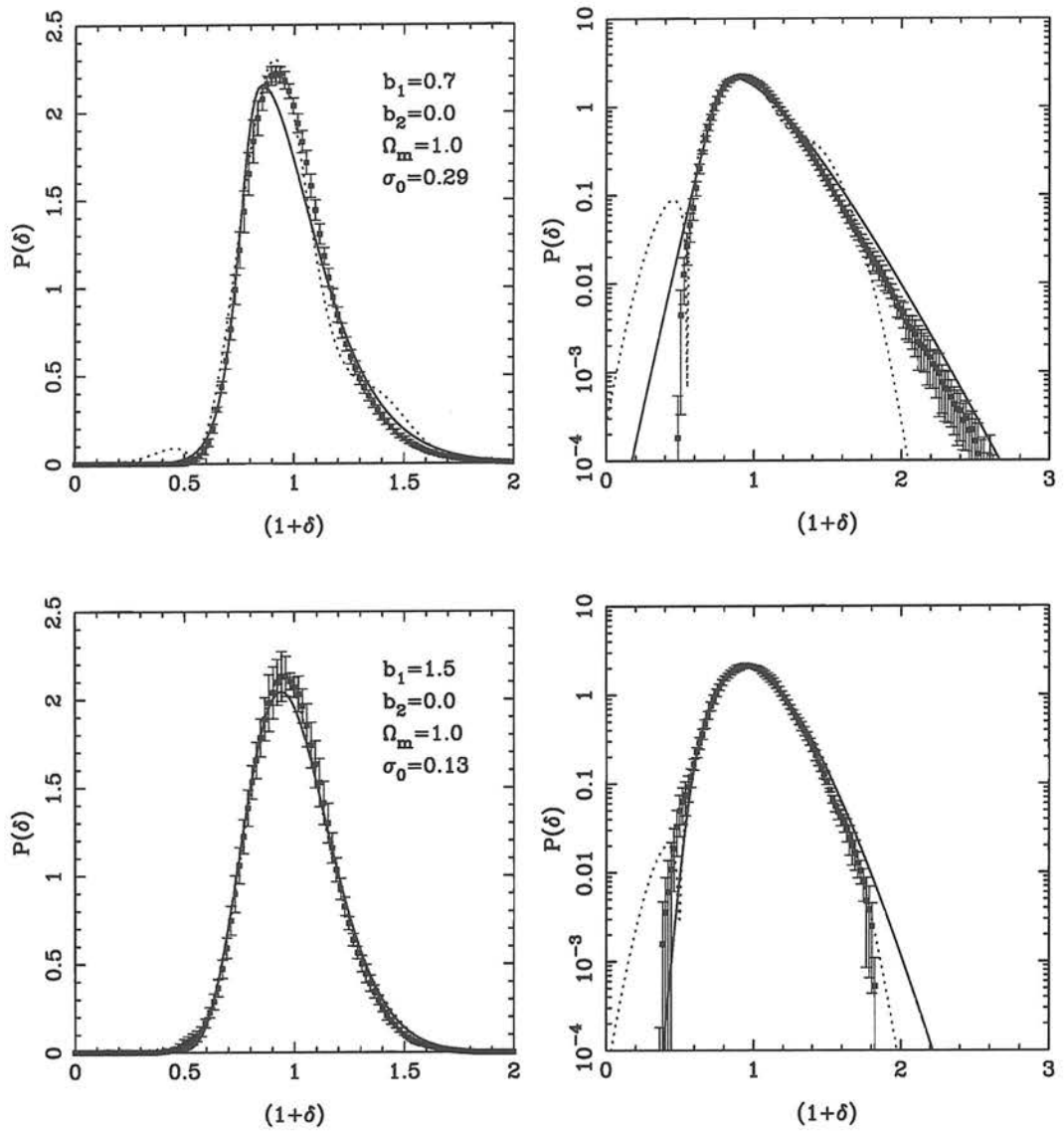

Figure 3.3: Comparison with N-body simulation in real space when $\sigma_s = 0.20$ and with linear bias $b_1 = 0.7$ (top panel) and $b_1 = 1.5$ (bottom panel). The solid line is the PDF for this work, the dotted line shows the reconstruction of the PDF from the Edgeworth expansion with the skewness parameter from §3.3.4. Filled squares represent the simulation data. The linear mass variance was $\sigma_0 = 0.29$ and 0.13 for the top and bottom plots respectively.

space $\sigma_s = 0.2$ was chosen. This relatively moderate variance was necessary because for the cases where $b_1 < 1$ the underlying σ_0 had to start quite large. For the combination of bias and redshift distortions the linear mass variance had to start a little higher because the simulation PDFs became dominated by sampling variance when the cell size was large. For these plots $\sigma_s = 0.25$.

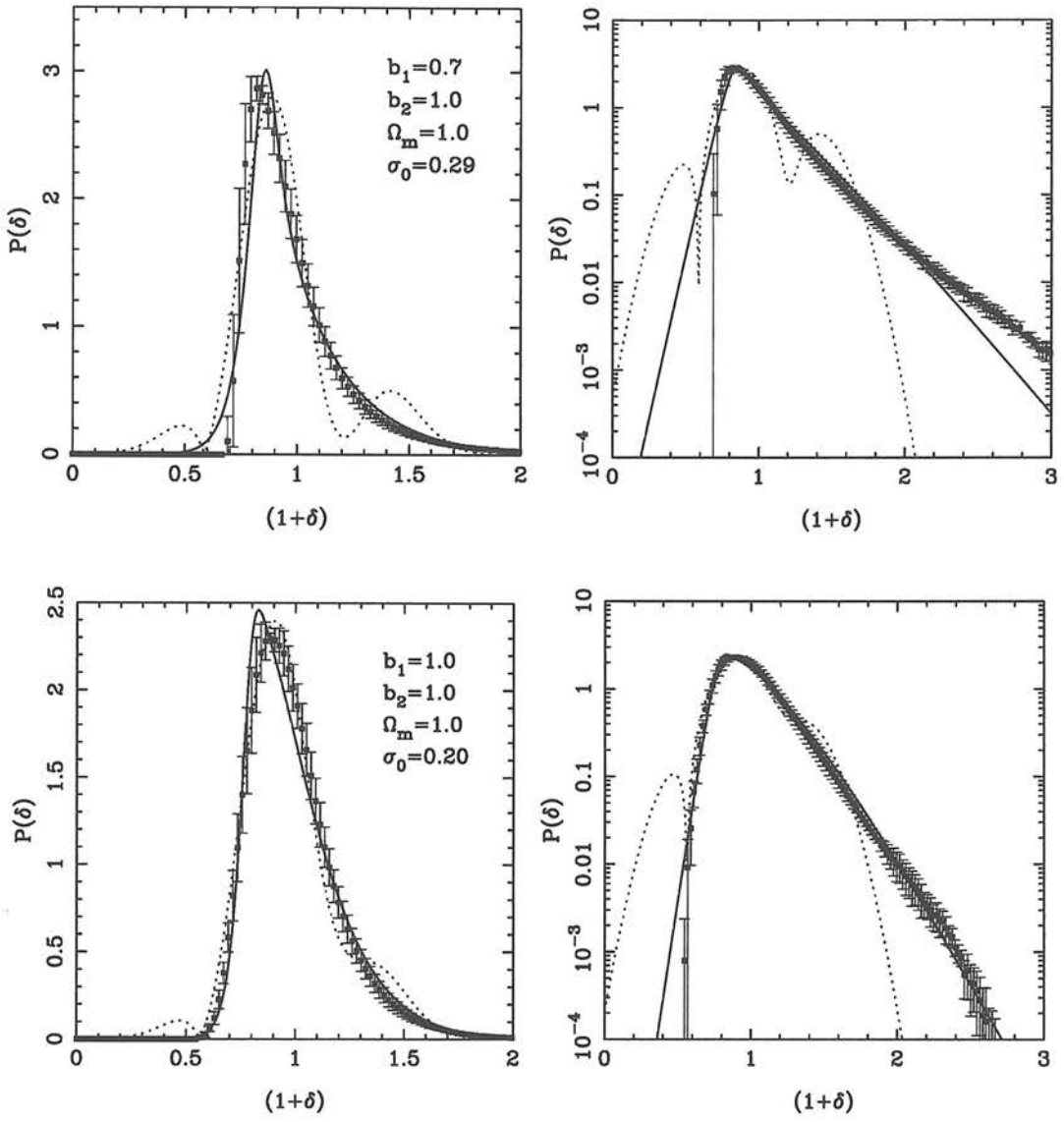

Figure 3.4: Comparison with N-body simulation in real space when $\sigma_s = 0.20$ and with linear and second-order bias. In the top panel $b_1 = 0.7$ while in the lower panel $b_1 = 1.0$ In both cases the second-order bias parameter $b_2 = 1.0$. The solid line is the PDF for this work, the dotted line shows the reconstruction of the PDF from the Edgeworth expansion with the skewness from §3.3.4. Filled squares represent the simulation data. The linear mass variance was $\sigma_0 = 0.29$ and 0.13 for the top and bottom plots respectively.

Figures 3.3 and 3.4 show the behavior of the PDF with various combinations of the bias parameters and with no redshift space distortions. The density parameter for these simulations was $\Omega = 1.0$, though in real space the quasi-linear evolution is not sensitive to this quantity (Bouchet *et al.*, 1992; Martel & Freudling, 1991).

Figure 3.3 shows the effect of a linear bias only, $b_1 = 0.7$ in the top panel and $b_1 = 1.5$ in the bottom. The linear mass variance was $\sigma_0 = 0.29$ and 0.13 respectively. The dominant effect on the shape is through the variance which tends to broaden and lower the amplitude PDF for $b_1 > 1$ and conversely makes the PDF more Gaussian when $b_1 < 1$. The fit to the data (points) of the PDF from this work is good in both cases, though when σ_0 is relatively large it misses the peak of the distribution and appears to be slightly too strongly skewed. The Edgeworth approximation (dotted lines) also shows excellent agreement with the simulations, particularly in the vicinity of the peak. The plots show the absolute value of the Edgeworth PDF. The "lobes" in the low density tail of the distribution represent negative probabilities in the Edgeworth PDF.

In figure 3.4 we show the fit to simulations when the second-order bias term b_2, is 1.0. The linear bias was set to $b_1 = 0.7$ (top) and $b_1 = 1.0$ (bottom). The linear mass variance was $\sigma_0 = 0.29$ (top) and $\sigma_0 = 0.20$ (bottom). To second-order in b_2 only contributes to the PDF via S_3 and the higher moments. The effect of the second-order bias is to fill in the void regions and enhance the peaks. The result for the PDF is a sharp drop-off of the low density tail and a dramatic amplification of the peak just beyond that point. The high density tail is also extended to account for the increased regions of very high density. The fit to the simulations for second-order biasing is good so long as σ_0 is reasonably small, though still in the quasi-linear regime. The breakdown in the fit comes mainly in the low density tail which for the theoretical curves drops away too slowly when the variance is high. The Edgeworth PDF breaks down quite badly in the tails when $b_2 \neq 0$. This suggests that the Edgeworth approximation becomes rather unstable when the skewness parameter is large, even when the variance is low. The peak of the Edgeworth PDF is not so badly affected however, and fits the data nicely so long as σ_0 is not too high.

Figure 3.5 shows the fit of the PDF to an unbiased field of galaxies in redshift space. Two sets of simulations were run with $\Omega_0 = 1.0$ and 0.3. The linear variance used for the theoretical PDFs was $\sigma_0 = 0.15$ and 0.17. The fit to both the second order model and the Edgeworth PDF is very good, although the linear variance in each case was quite small to ensure that $\sigma_s = 0.2$. We found that the perturbation theory approximation began to break down when the redshift space variance was $\sigma_s = 0.4$. Although the Edgeworth followed the peak and low density part of the distribution well to this variance and higher, its high density

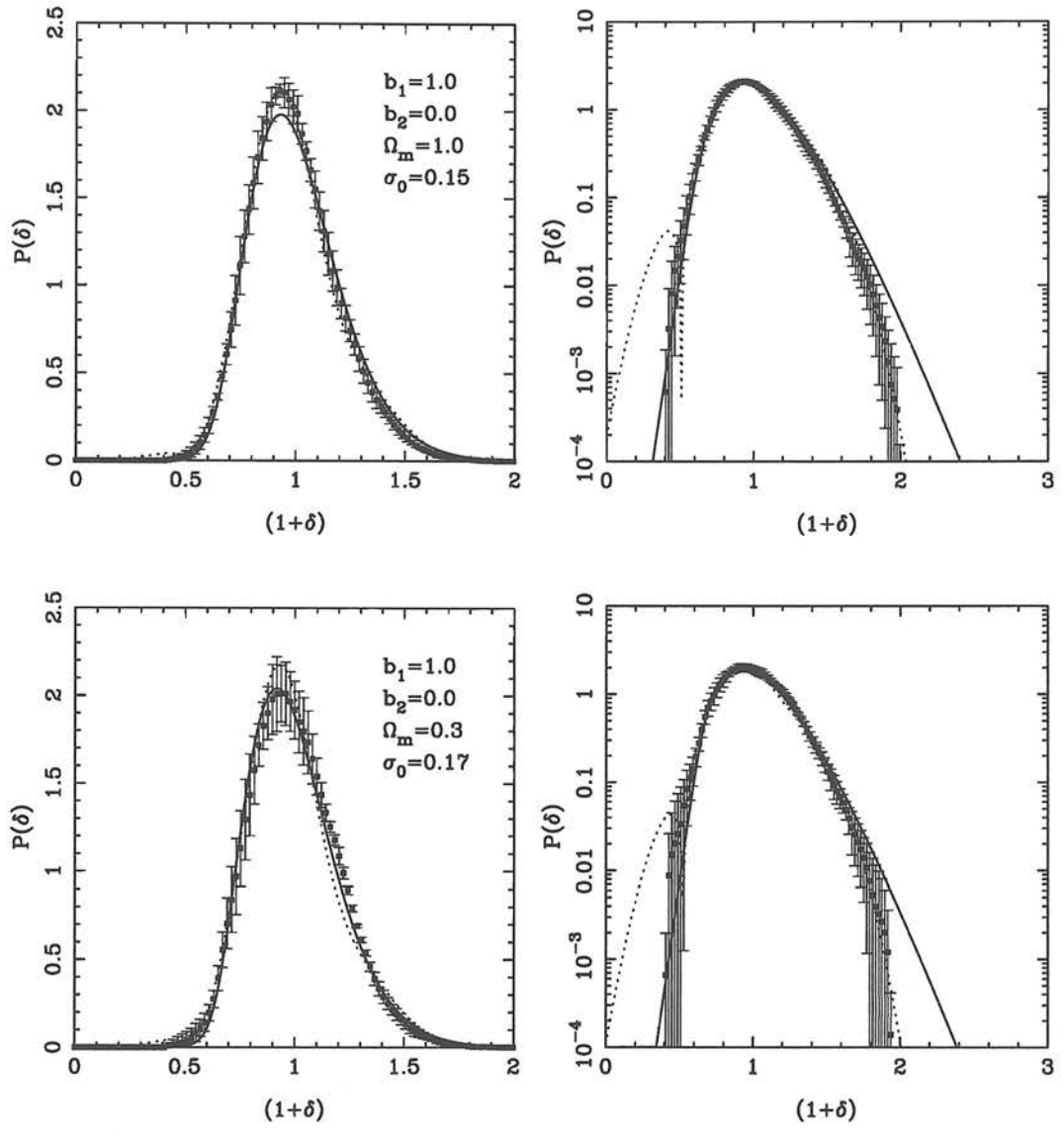

Figure 3.5: Comparison with N-body simulations in redshift space for $\Omega_0 = 1.0$ and $\Omega_0 = 0.3$ when $\sigma_s = 0.2$. The bias parameters were in both cases $b_1 = 1.0$ and $b_2 = 0$, i.e no bias. The solid line is the PDF for this work, the dotted line shows the reconstruction of the PDF from the Edgeworth expansion with the skewness parameter from §3.3.4. Filled squared represents the simulation data. The linear mass variance was $\sigma_0 = 0.15$ and 0.17 for the top and bottom plots respectively.

tail became unstable at a much lower σ_s. In both cases the PDFs look more Gaussian than in real space because of the reduction in S_3^s. The theoretical plots are almost identical in each case, as expected since it was arranged for the variance of the redshifted field to be identical in each case, and anyway the skewness in redshift space is only very weakly dependant upon Ω_m when b_1 is close to unity.

The numerical PDFs are marginally different, although this is suspected to be a numerical effect, as suggested by the large error bars around the peak of the distribution for $\Omega_m = 0.3$.

On much smaller scales one would expect there to be a real difference between the two PDFs as fingers of god, due to the pairwise velocities in clusters, become important. The second-order analysis does not allow for these strongly nonlinear effects, and so the analysis was restricted to scales large enough that these effects were not important. The agreement between theory and the simulations suggests that this is was indeed that valid. The effect that would be expected, would be a decrease in the variance and skewness of the PDFs in redshift space.

The final plots, figure 3.6, show the combined effect of both bias and redshift distortions. In the top row $b_1 = 1.2$ with $b_2 = 0.0$ and on the bottom $b_1 = 1.0$ and $b_2 = 1.0$. For both cases the density parameter was $\Omega_m = 1.0$. In each of the plots $\sigma_s = 0.25$ — due to problems with creating the bias/redshift simulations, satisfactory measurements of the PDFs for $\sigma_s = 0.2$ were unable to be made. The linear mass variance was therefore $\sigma_0 = 0.18$ in the top plot and 0.19 in the bottom. The fit in both cases is very good, although the Edgeworth approximation becomes slightly unstable when $b_2 = 1.0$ because of the relatively high skewness. Although the redshift distortions do wash out some of the effect of the bias parameters, there are dependencies which are reproduced by the models to a reasonable degree of accuracy. This is encouraging for the purposes of constraining cosmological models using the PDF and data from galaxy redshift surveys.

In general there is a good similarity between all of the numerical PDFs and those found from either our analysis based on the Chapman-Kolmogorov equation or the Edgeworth approximation with the redshift space skewness parameter S_3^s. The Edgeworth expansion clearly breaks down sooner in the tails of the distribution, and for large values of the skewness parameter. Considering that both models use second-order perturbation theory and have the same skewness and variance it is perhaps confusing that they behave so differently with various combinations of the parameters. However one must not forget that the Edgeworth approximation and the model of §3.3.2, rely on very different approaches to obtain the PDF.

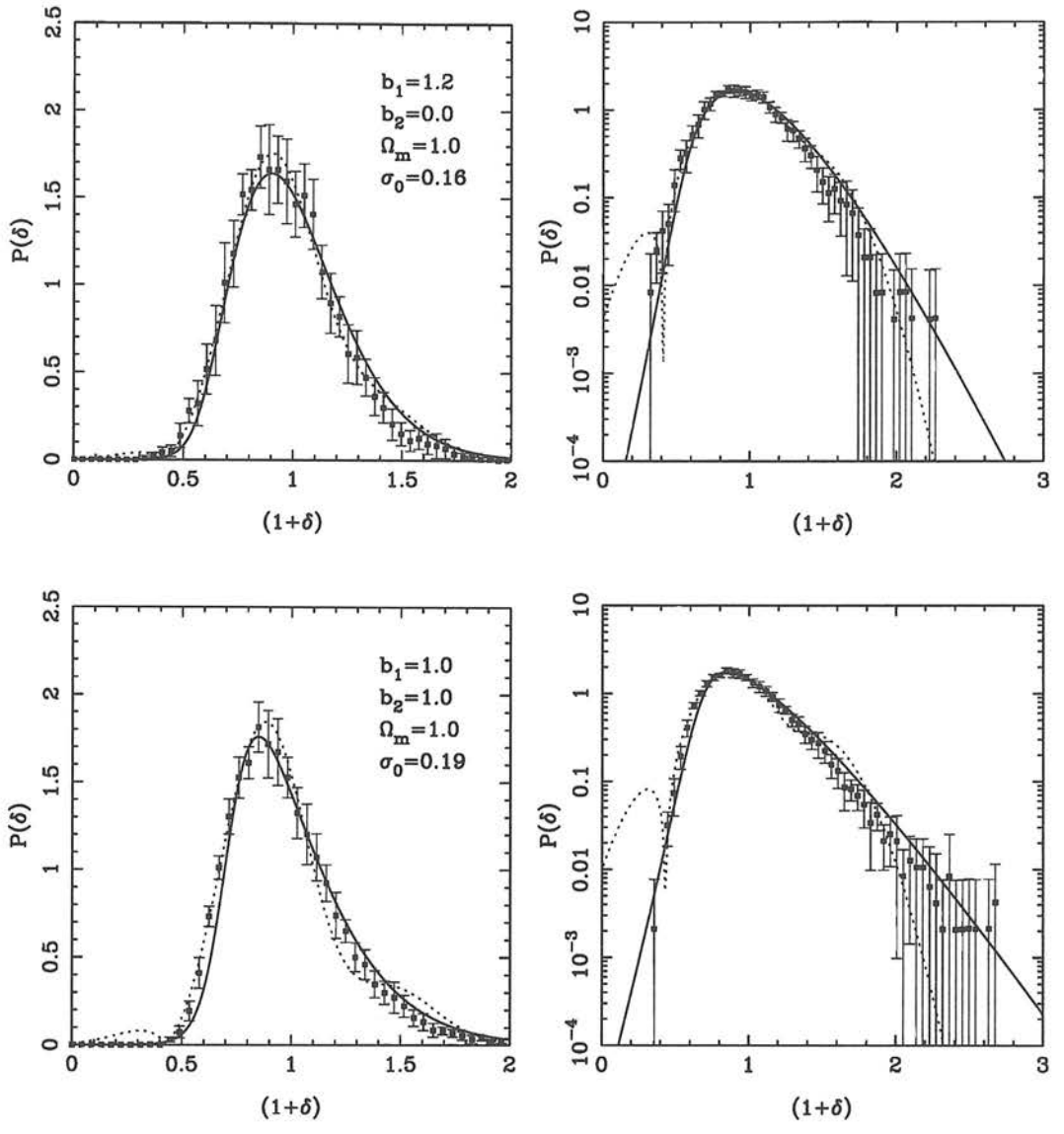

Figure 3.6: Comparison with N-body simulations showing the combined effect of bias and redshift distortions for $\Omega_0 = 1.0$ and when $\sigma_s = 0.25$. The bias parameters were $b_1 = 1.2$ and $b_2 = 0$ in the upper panel and $b_1 = 1.0$, $b_2 = 1.0$ in the lower. The solid line is the PDF for this work, the dotted line shows the reconstruction of the PDF from the Edgeworth expansion with the skewness parameter from §3.3.4. Filled squared represents the simulation data. The linear mass variance was $\sigma_0 = 0.16$ and 0.19 for the top and bottom plots respectively.

3.5.4 Constant β PDFs

An interesting and potentially useful feature of modeling the PDF in redshift space comes when one considers parameter combinations that are degenerate to

linear order. The combination

$$\beta_1 = \frac{\Omega_m^{0.6}}{b_1}, \tag{3.63}$$

for example, is a common quantity to measure in linear analysis of galaxy redshift surveys (see *e.g.* Tadros *et al.* 1999 and Taylor *et al.* 2000, for a recent measurement from the PSCz redshift survey).

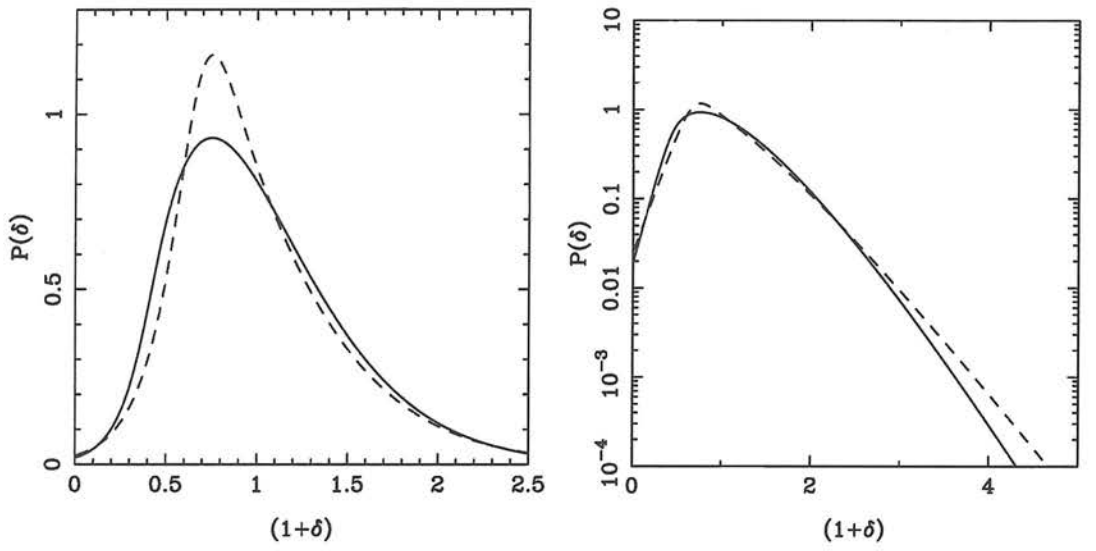

Figure 3.7: Theoretical PDFs for a biased galaxy field in redshift space. The parameters are such that the combination $\beta = 0.5$. For the solid curve $\Omega_0 = 1.0$ with $b_1 = 2.0$ and $b_2 = 0$ whereas for the dotted curve $\Omega_0 = 0.3$ with $b_1 = 1.0$ and $b_2 = 0$. In both cases the filter was a Gaussian of radius 10 h^{-1}Mpc.

PDFs were constructed of two fields sharing the same β_1 but with different combinations of the cosmological density and linear bias parameters, neglecting the effects of second-order bias. The combination $\beta_1 = 0.5$ with $\Omega_m = 0.3$ and $b_1 = 1.0$ was chosen for one model and $\Omega_m = 1.0$ with $b_1 = 2.0$ for the other. The linear mass variance for each was inferred from the observed abundance of clusters from (Viana & Liddle, 1996)

$$\sigma(R_{th}) = \sigma_8 \left(\frac{R_{th}}{8\,h^{-1}\mathrm{Mpc}} \right)^{-\gamma(R)}, \tag{3.64}$$

where

$$\gamma = (0.3\Gamma + 0.2) \left[2.92 + \log \left(\frac{R_{th}}{8\,h^{-1}\mathrm{Mpc}} \right) \right] \tag{3.65}$$

and with Γ the CDM shape function. The abundance of clusters was parameterised by

$$\sigma_8 = 0.6\Omega_0^{-C}, \tag{3.66}$$

where $C \approx 0.49$ for the closed and $C \approx 0.43$ for the open models. The underlying linear mass variance was found for each at constant top–hat filter radius, R_{th}. The resulting PDFs are shown in figure 3.7, the solid curve being the high-Ω model and the dashed line the low-Ω model. Clearly there is a marked difference between the two PDFs, a result of the different ways in which b_1 and Ω contribute to the variance and the skewness. This effect could potentially be used to discriminate between different cosmological models.

3.6 Summary

In this chapter an expression for the nonlinear 1-point probability distribution of galaxies in redshift space was derived. This function is useful in the analysis of redshift surveys as it is a quantity that can be directly observed. The nonlinearity of the density field was treated with second-order Eulerian perturbation theory, and transformed from the mass-density distribution to a galaxy distribution using a second-order local bias prescription. This was then mapped to redshift space, again using second-order perturbation theory. The transformation of the initial probability distribution to the evolved distribution was carried out using the Chapman-Kolmogorov equation. This allowed an exact expression for the second-order characteristic function for the galaxy distribution to be derived. The Chapman-Kolmogorov equation was shown to be more general than just a transformation of variables as it could be used to calculate the effects of stochastic bias schemes.

Taking the derivative of the galaxy characteristic function a new expression for the skewness parameter of galaxies in redshift space was derived, S_3^s. Unlike other derivations, a closed-form expression was found which included the effects of a quadratic bias term. It was found that in general for values of the linear bias parameter b_1 below 1.5, S_3^s was smaller than its real space value, S_3. It was also found that, while the first-order bias terms were largely independent of the linear distortion parameter β_1, or Ω_m for values of b_1 around unity, the quadratic bias terms introduced a strong dependency on cosmological parameters. An analysis of the full 1-point PDF in real and redshift space confirmed these findings. In

addition it was found that quadratic bias produced a distinct sharp cut-of in the PDF for low-density regions.

In comparing the PDF with those measured from N-body simulations, good agreement was found for all combinations of parameters. Also, the Edgeworth series was found to fit the numerical PDFs rather well when the series was truncated to second-order and the redshift space skewness and variance from §3.3.4 were used. The models, particularly the Edgeworth approximation, fit the data most poorly when the linear mass variance and the skewness were both high ($\sigma_0 > 0.4$). This occurred on small scales or where there was a large degree of non-linear bias.

The analysis leaves two problems unresolved. The first is the issue of Fingers of God, which were not modelled. This restricts the scales on which the PDF can be modelled, although it did not seem to be a problem when results were compared to simulations. The second issue is that of smoothing the final density field. This was neglected in the analysis, although it has been included in the analysis of other PDFs (see *e.g.* Bernardeau, 1994). Again, when comparing with the results of simulations a significant effect was not seen. This may have been a result of the type of power spectra that was used to test the model against. The effect of smoothing is to transfer power across scales and for some power spectra this transfer will be minimal. However, for the range of spectra that was investigated here it was only required that the variance be correctly calibrated against simulations, and good agreement was found. An advantage of the PDF over other statistical measures is that it is straightforward to see if the fit is poor.

A possible future extension of this work would be to compare the theoretical PDF with that of galaxies measured from the PSCz galaxy survey. This would be useful both in testing the gravitational instability hypothesis and in constraining cosmological models, using data from the nonlinear regime of the galaxy distribution. This step is vital for maximising the amount of information available from galaxy redshift surveys. Although it was found that redshift distortions do dampen some of the effects of bias, there are dependencies that may be exploited. It was shown how using the PDF in conjunction with the abundance of clusters may provide a way to distinguish between cosmological models that are degenerate in linear analysis.

3.7 Appendix: Lagrangian perturbation theory

In this appendix the higher order generalisation of the Lagrangian perturbation theory, hinted at in §1.4.3, is presented. The reason for this inclusion is to set the stage for deriving the second-order, redshift space evolution of δ. For a full account of Lagrangian perturbation theory see (Bouchet *et al.*, 1995).

From the outline in chapter 1 we have the Eulerian – Lagrangian mapping

$$\boldsymbol{x} = \boldsymbol{q} + \Psi(\boldsymbol{q}, t), \tag{3.67}$$

where $\Psi(\boldsymbol{q}, t)$ is the displacement vector field of fluid particles initially at $\boldsymbol{q}$. The density at a point in the trajectory of such a fluid particle was found to be related to the Jacobian of the transformation

$$\delta[\boldsymbol{x}(\boldsymbol{q})] = J^{-1} - 1 \tag{3.68}$$

where the Jacobian matrix J_{ij}, with determinant J, is

$$J_{ij} = \frac{\partial x_i}{\partial q_j}. \tag{3.69}$$

The Euler and Poisson equations simplify when recast in terms of a new time variable

$$d\tau \propto a^{-2}\, dt \tag{3.70}$$

(Doroshkevich *et al.*, 1973). The evolution of density perturbations is then governed by

$$\ddot{x}_i = -\nabla_i \phi, \quad \nabla^2 \phi = \beta(\tau)\delta, \tag{3.71}$$

where dots denote differentiation with respect to τ and where $\nabla_i \equiv \partial/\partial x_i$ for the moment. The factor β depends upon the spatial curvature

$$\beta = \frac{6}{\tau^2 + K} \tag{3.72}$$

where K is $0, -1$ or $+1$ for flat, open and closed universes respectively. The equations to solve can be written in terms of the Jacobian, they are

$$J \nabla_i \ddot{x}_i = \beta(J - 1) \tag{3.73}$$

and

$$\nabla_i \ddot{x}_i = J^{-1} \frac{\partial \ddot{x}_i}{\partial q_j} A_{ij}. \tag{3.74}$$

The solutions follow from a perturbative expansion of the displacement field and expansion of the determinant of the Jacobian into its invariant scalars. To second-order this gives

$$J = 1 + \boldsymbol{\nabla} \cdot \boldsymbol{\Psi}_1 + \boldsymbol{\nabla} \cdot \boldsymbol{\Psi}_2 + \frac{1}{2}\left[(\boldsymbol{\nabla} \cdot \boldsymbol{\Psi}_1)^2 - \nabla_i \Psi_1^j \nabla_j \Psi_1^i\right], \tag{3.75}$$

where we now define $\nabla_i \equiv \partial/\partial q_i$. The solutions for the growth of $\boldsymbol{\Psi}(\boldsymbol{q}, t)$ are found to be

$$\boldsymbol{\Psi}_1(\boldsymbol{q}, t) = D_1(t)\tilde{\boldsymbol{\Psi}}_1(\boldsymbol{q}), \tag{3.76}$$

$$\boldsymbol{\Psi}_2(\boldsymbol{q}, t) = D_2(t)\tilde{\boldsymbol{\Psi}}_2(\boldsymbol{q}), \tag{3.77}$$

where the $D_n(t)$, are related by

$$D_2 = -\frac{3}{7}\Omega^{-2/63} D_1^2 \tag{3.78}$$

for $\Omega < 1$ and $\Omega_\Lambda = 0$, and by

$$D_2 = -\frac{3}{7}\Omega^{-1/143} D_1^2 \tag{3.79}$$

for $\Omega + \Omega_\Lambda = 1$. The linear growth factor D_1, is the same factor as for the Eulerian derivation, as discussed in §1.4.3. The divergence of the second-order displacement field $\boldsymbol{\Psi}_2(\boldsymbol{q}, t)$ can be inferred from the initial linear displacements

$$\boldsymbol{\nabla} \cdot \boldsymbol{\Psi}_2(\boldsymbol{q}, t) = \frac{D_2}{2D_1^2}\left[(\boldsymbol{\nabla} \cdot \boldsymbol{\Psi}_1(\boldsymbol{q}, t))^2 - \nabla_i \Psi_1^j(\boldsymbol{q}, t) \nabla_j \Psi_1^i(\boldsymbol{q}, t)\right]. \tag{3.80}$$

Writing the functional $\delta[\boldsymbol{x}(\boldsymbol{q})]$ as a function of both Lagrangian coordinate $\boldsymbol{q}$, and time t, the development of the density field in Lagrangian coordinates is, using equation (3.68)

$$\delta(\boldsymbol{q}, t) = \nabla \cdot \boldsymbol{\Psi}_1 + \boldsymbol{\nabla} \cdot \boldsymbol{\Psi}_2 + \frac{1}{2}\left[(\boldsymbol{\nabla} \cdot \boldsymbol{\Psi}_1)^2 - \nabla_i \Psi_1^j \nabla_j \Psi_1^i\right] + (\boldsymbol{\nabla} \cdot \boldsymbol{\Psi}_1)^2. \tag{3.81}$$

This implies the important relation (also obtainable from the linearised continuity equation)

$$\delta_1 = \boldsymbol{\nabla} \cdot \boldsymbol{\Psi}_1 \tag{3.82}$$

which is true to first order either in Lagrangian or Eulerian coordinates. The definition of the trace free tidal tensor is then

$$E_{ij}(\boldsymbol{q}, t) = \nabla_i \Psi_1^j(\boldsymbol{q}, t) - \frac{1}{3}\boldsymbol{\nabla} \cdot \boldsymbol{\Psi}(\boldsymbol{q}, t). \tag{3.83}$$

In terms of familiar fields the second-order Lagrangian evolution of the density reads

$$\delta(\boldsymbol{q},t) = \delta_1(\boldsymbol{q},t) + \frac{1}{3}(2-\kappa)\delta_1^2(\boldsymbol{q},t) + \frac{1}{3}(1+\kappa)E^2(\boldsymbol{q},t), \tag{3.84}$$

where we have used equation (3.81) in conjunction with equations (3.80) and (3.83) and where $\kappa = D_2/D_1^2$. The equivalent Eularian solution (see e.g. Peebles, 1980 and chapter 2) is obtained by evolving equation (3.84) from $\boldsymbol{q}$ to the comoving position $\boldsymbol{x}$ by a Taylor expansion to the appropriate order

$$\mathbf{A}(\boldsymbol{x}) = \mathbf{A}(\boldsymbol{q}) - (\boldsymbol{q}-\boldsymbol{x}) \cdot \boldsymbol{\nabla}\, \mathbf{A}(\boldsymbol{q}). \tag{3.85}$$

Chapter 4

Nonlinear parameter estimation

This work was carried out in collaboration with Andy Taylor. It was submitted to Monthly Notices of the Royal Astronomical Society for publication.

4.1 Introduction

The estimation of cosmological parameters from galaxy redshift surveys, Cosmic Microwave Background (CMB) surveys, weak lensing surveys and velocity field surveys has become a major industry in cosmology, due to the data explosion the field is currently undergoing. To date the majority of the analysis has considered the problem of parameter estimation from the large-scale, linear regime. However much of the important information on parameters lies on smaller scales, where nonlinear gravitational clustering has distorted the initial field. In the case of galaxy redshift surveys additional nonlinearity may arise form the bias relationship between galaxies and matter, while in the case of the CMB the original pattern is still evident, allowing one to test the temperature fluctuations for evidence of primordial non-Gaussianity.

The industry standard for parameter estimation in the linear regime is the multivariate Gaussian likelihood method. Within this framework the uncertainty on parameters can be estimated from the second derivatives of the likelihood function, the Fisher Information matrix. These ideas are discussed further in §4.2, by way of introduction for the material in the rest of the chapter. While likelihood methods in the linear, Gaussian regime have been extensively studied, until recently little work has been done on the non-Gaussian generalisation. Amendola

(1996) and Rocha *et al.* (2000) have extended the likelihood methods to include non-Gaussian contributions by expanding the likelihood function in a series of cumulants. Amendola considered the effects of degradation of parameter uncertainties due to the non-Gaussian broadening of the likelihood function, while Rocha et al. applied their likelihood to estimate residual non-Gaussianity in the CMB.

In the analysis of galaxy redshift surveys, Matarrese *et al.* (1997) have investigated a Gaussian likelihood estimator for the bispectrum as a tool for extracting the mean density parameter and galaxy bias from galaxy redshift surveys in the nonlinear regime. This builds on the work of Fry (1994) who suggested that the bispectrum could be used to break the linear degeneracy between the bias parameter and the density parameter, Ω_m. Verde *et al.* (1998) developed this further to include redshift space distortions. Scoccimarro *et al.* (1998) and Scoccimarro *et al.* (1999) similarly investigated the bispectrum, including the effects of redshift space distortions and galaxy bias. Scoccimarro *et al.* (2000) have recently estimated the bias parameters from the combined IRAS-QDOT and 2 Jy and 1.2 Jy redshift surveys.

4.1.1 Chapter breakdown

In this chapter a new method is developed for exploring the estimation of cosmological parameters from scales going into the nonlinear regime. The general non-Gaussian multivariate probability distribution function and the non-Gaussian Fisher matrix are derived. Since the most relevant non-Gaussianity will be due to nonlinear evolution of the density field, second-order perturbation theory is used to find the dependance of the higher-order moments on cosmological parameters and to estimate the Fisher matrix to second-order. The methods are illustrated using a realistic model galaxy redshift survey, but note that they can be similarly applied to a 2D weak lensing, or 3D cosmic velocity survey.

The chapter is organised as follows. In §4.2 the ideas central to likelihood and Fisher analysis are discussed, setting up definitions for the material in the chapter to follow. In §4.3 the non-Gaussian expansion of the multivariate probability distribution function is described in both the discrete and continuum limits. In §4.4 the formalism for calculating the Fisher information matrix in the non-Gaussian regime is developed. A new function, the parameter entropy, is introduced to

study the likelihood surface in parameter space in §4.5, a general expression is calculated for non-Gaussian fields. The new methods are illustrated by application to a model galaxy redshift survey, including the effects of shot noise, redshift space distortions and galaxy bias. Details of the analytical model are presented in §4.6. It is shown how nonlinear effects change the estimation of parameters in two surveys; the 2-degree Field galaxy redshift survey (2dF; Colless 1998) and the Sloan Digital Sky Survey (SDSS; Gunn 1995). The results are shown in §4.7. Finally, conclusions are presented in §4.8. A short appendix deals with technical issues.

4.2 Likelihood and Fisher analysis

Any cosmological dataset can be represented by a random field $\phi(\boldsymbol{x})$, that is completely characterised by its multivariate PDF, $\rho[\phi(\boldsymbol{x})]$. The PDF may depend in some known way upon a vector of parameters $\boldsymbol{\theta} = (\theta_1, \theta_2, ..., \theta_m)$, which define a model for ϕ. Given a measured dataset, the probability distribution of possible parameters is given by the likelihood function $L(\boldsymbol{\theta}|\phi)$. The best estimate of the true parameter values $\boldsymbol{\theta}'$ that one may make, are those for which the likelihood function is a maximum *i.e.* for which the probability is highest, given the data. The relationship between the likelihood and the PDF of the data is given by the Bayesian expression

$$\rho(\boldsymbol{\theta}|\phi) = \rho(\boldsymbol{\theta})\rho(\phi|\boldsymbol{\theta}). \tag{4.1}$$

Here $\rho(\boldsymbol{\theta}|\phi)$ represents the conditional probability of the parameters given the data, which is just the likelihood, and $\rho(\phi|\boldsymbol{\theta})$ is the conditional probability for the data given the model, which is provided by $\rho[\phi(\boldsymbol{x})]$. The quantity $\rho(\boldsymbol{\theta})$ is the prior probability. In this chapter it is always assumed that the prior is a uniform distribution, since it seems a reasonable approximation to make that all sets of parameters are equally likely *a priori*. Equation (4.1) then states that the likelihood function for parameters is just given by the multivariate probability distribution for ϕ.

If the maximum likelihood estimate for $\boldsymbol{\theta}$ is to be a good estimate, then it should be unbiased, $\langle\boldsymbol{\theta}\rangle = \boldsymbol{\theta}'$. In other words, on average the likelihood estimate picks the true parameters. A good estimate should also be scattered tightly about the

true values θ'. This means that the standard deviation

$$\Delta\theta_i = (\langle\theta_i^2\rangle - \langle\theta_i\rangle^2)^{1/2} \tag{4.2}$$

should be small. In fact a number of important theorems have been proven along these lines (*e.g.* Kendal & Stuart, 1969). It has been shown that that the maximum likelihood estimate of $\boldsymbol{\theta}'$ will always be the best, unbiased estimate that one can make of the parameters. Furthermore given a sufficiently large dataset, any estimate of the parameters asymptotically becomes the maximum likelihood estimate. The smallest attainable error bars on $\boldsymbol{\theta}$ can be predicted given the likelihood using the so called *Cramèr-Rao* inequality

$$\Delta\theta_i \geq (F_{ij})^{-1/2}, \tag{4.3}$$

where the quantity F_{ij} is called the Fisher information matrix, which measures the curvature of the likelihood function about its peak in parameter space. The Fisher matrix is defined by

$$F_{ij} = \left\langle \frac{\partial^2 \mathcal{L}}{\partial\theta_i \partial\theta_j} \right\rangle, \tag{4.4}$$

where $\mathcal{L} = -\ln L$ is the log likelihood.

When ϕ forms a Gaussian random field, the likelihood and Fisher methods have been explored in detail and shown to be of great importance in cosmology. Tegmark *et al.* (1997) were the first to study the Gaussian Fisher information matrix as a general tool for characterising the information content of cosmological surveys, while Heavens & Taylor (1997) demonstrated its value for the design of galaxy redshift surveys. Tegmark (1997) used the Gaussian Fisher matrix to investigate the accuracy of parameter estimation from the Sloan Digital Sky Survey in some detail, but did not calculate the effects of nonlinear clustering, redshift space distortions, or nonlinear biasing (as is done in §4.6). Jungman *et al.* (1996) applied a Fisher analysis to the CMB, while Hu & Tegmark (1999) used it to estimate parameter uncertainties in weak lensing surveys. The concern of this chapter is what happens when ϕ is not a Gaussian field, something that has been dealt with little in the literature (as discussed in §4.1).

4.3 Expansion of the multivariate PDF

4.3.1 The discrete distribution

The first step is to construct a non-Gaussian multivariate PDF. The continuous random field $\phi(\boldsymbol{x})$, can be discretised and treated like an N-dimensional data vector $\boldsymbol{\phi}$, whose components ϕ_i, may represent, for example, an array of pixel values or the amplitude of a set of harmonic modes. The multivariate PDF of ϕ_i can be written as the Fourier transform of a characteristic function;

$$\rho[\boldsymbol{\phi}] = \int D[\boldsymbol{J}]\, G[\boldsymbol{J}] e^{i\boldsymbol{J}.\boldsymbol{\phi}}, \tag{4.5}$$

where $\int D[\boldsymbol{J}] = \int \prod d^N J/(2\pi)^N$ is a multidimensional integral. The characteristic function can be expressed by a set of cumulants, defined by the series

$$\ln G[\boldsymbol{J}] = \sum_n \frac{i^n}{n!} \langle \phi_{j_1} ... \phi_{j_n} \rangle_c J_{j_1} ... J_{j_n}, \tag{4.6}$$

where there is an implicit summation over the j_n, running from 1 to N. The $\langle \phi_{j_1} \cdots \phi_{j_n} \rangle_c$ are the n^{th} order cumulants, or connected moments, of the field.

If only the second cumulant exists the distribution is a Gaussian. If the initial distribution is Gaussian one can separate out the $n = 2$ term and then deal with the rest of the terms in the series. Expanding out this second exponential to first order, keeping only terms to $n = 3$ and substituting back into equation (4.5) one finds

$$\begin{aligned} \rho[\boldsymbol{\phi}] &= \int D[\boldsymbol{J}] \exp[-\frac{1}{2} J_i C_{ij} J_j] \\ &\quad \times \left(1 - \frac{i}{3!} D_{ijk} J_i J_j J_k\right) \exp(i J_m \phi_m) \\ &= \int D[\boldsymbol{J}] \exp[-\frac{1}{2} J_i C_{ij} J_j] \\ &\quad \times \left(1 - \frac{1}{3!} D_{ijk} \frac{\partial^3}{\partial\phi_i \partial\phi_j \partial\phi_k}\right) \exp(i J_m \phi_m), \end{aligned} \tag{4.7}$$

where $C_{ij} = \langle \phi_i \phi_j \rangle_c$ is the data covariance matrix and $D_{ijk} = \langle \phi_i \phi_j \phi_k \rangle_c$ is the data skewness. In the second line of equation (4.7) the substitution $i\boldsymbol{J} = \partial/\partial\boldsymbol{\phi}$ has been used. Evaluating the Gaussian integral gives

$$\rho[\boldsymbol{\phi}] = \left(1 - \frac{1}{3!} D_{ijk} \frac{\partial^3}{\partial\phi_i \partial\phi_j \partial\phi_k}\right) \frac{\exp[-\frac{1}{2}\phi_i C_{ij}^{-1} \phi_j]}{\sqrt{2\pi \det C}}. \tag{4.8}$$

This procedure is a multivariate generalisation of the Edgeworth expansion for a single variable (see Juszkiewicz *et al.*, 1995; Bernardeau & Kofman, 1995). Finally, performing the differentiation one finds

$$\begin{aligned}\rho[\phi] &= \left[1 - \frac{1}{6}D_{ijk}\left(3C^{-1}_{a[i}C^{-1}_{jk]}\phi_a - C^{-1}_{ia}C^{-1}_{jb}C^{-1}_{kb}\phi_a\phi_b\phi_c\right)\right] \\ &\quad \times \frac{\exp\left[-\frac{1}{2}\phi_i C^{-1}_{ij}\phi_j\right]}{\sqrt{2\pi \mathrm{det}C}},\end{aligned} \tag{4.9}$$

where $A_{[i_1\cdots i_n]} \equiv 1/n!(A_{i_1\cdots i_n} + \text{perms})$ is the symmetrization operator. This non-Gaussian multivariate distribution is the first major result of this chapter.

A well-known problem with truncating the moments, as for equation (4.9), is that the resulting distribution is not thought to be a well-defined probability distribution function. In fact the problem lies not in the truncation of moments, as the characteristic function is still well-defined, but in the approximate calculation of the PDF itself in equation (4.7). Hence the Edgeworth series, although properly normalised, can produce non-physical oscillations and negative values if the variance and skewness are pushed too far, as discussed in chapter 3. This is a breakdown of the series approximation, and one should take care not to force the PDF into this regime.

Equation (4.9) can be generalised to arbitrary order. The input for the nonlinear multivariate PDF are the higher-order moments of the field. These can either be left arbitrary and measured from the data using the PDF as a fitting function, or estimated by perturbation theory and used to estimate other parameters from the Bayesian relation, equation (4.1).

In developing the methodology it will be useful to express the perturbed Gaussian distribution as

$$\rho[\phi] = \rho_0[\phi](1 - X), \tag{4.10}$$

where $\rho_0[\phi]$ is the underlying Gaussian distribution and X is a small perturbation. It is worth noting that some of the results of this chapter are quite general and apply to all cases where the multivariate PDF is expressible in this way, for example the harmonic oscillator approach of Rocha *et al.* (2000), or multivariate generalisations of other non-Gaussian fields.

4.3.2 The continuum distribution

In most calculations it is easier to consider the continuum distribution of the function $\phi(\boldsymbol{x})$. This can be found by taking the limit $N \to \infty$ and substituting $\sum \to V \int d^3k/(2\pi)^3$. From here on we choose to use a field embedded in three spatial dimensions, but the method is easily generalised to an arbitrary number of dimensions. In the continuum limit the underlying Gaussian distribution is

$$\rho_0[\phi] = \frac{1}{A^{1/2}} \exp\left[-\frac{1}{2}\int d^3x_1 d^3x_2\, \phi(\boldsymbol{x}_1) C^{-1}(\boldsymbol{x}_1, \boldsymbol{x}_2)\phi(\boldsymbol{x}_2)\right], \tag{4.11}$$

where A is a normalisation factor. The expression for X, in the continuum case, containing the higher-order moments of the field $\phi(\boldsymbol{x})$, is

$$\begin{aligned} X &= \int \prod_{i=1}^{4} d^3x_i\, D(\boldsymbol{x}_1, \boldsymbol{x}_2, \boldsymbol{x}_3)\, C^{-1}(\boldsymbol{x}_4, \boldsymbol{x}_1) C^{-1}(\boldsymbol{x}_2, \boldsymbol{x}_3)\, \phi(\boldsymbol{x}_4) + \text{cyc}(231, 312) \\ &+ \int \prod_{i=1}^{6} d^3x_i \Big[D(\boldsymbol{x}_1, \boldsymbol{x}_2, \boldsymbol{x}_3)\, C^{-1}(\boldsymbol{x}_1, \boldsymbol{x}_4) C^{-1}(\boldsymbol{x}_2, \boldsymbol{x}_5) C^{-1}(\boldsymbol{x}_3, \boldsymbol{x}_6) \\ &\quad \phi(\boldsymbol{x}_4)\phi(\boldsymbol{x}_5)\phi(\boldsymbol{x}_6)\Big], \end{aligned} \tag{4.12}$$

where cyc means to permutate indices. The covariance and bivariance functions are, respectively

$$C(\boldsymbol{x}_1, \boldsymbol{x}_2) = \langle \phi(\boldsymbol{x}_1)\phi(\boldsymbol{x}_2)\rangle_c \tag{4.13}$$

$$D(\boldsymbol{x}_1, \boldsymbol{x}_2, \boldsymbol{x}_3) = \langle \phi(\boldsymbol{x}_1)\phi(\boldsymbol{x}_2)\phi(\boldsymbol{x}_3)\rangle_c \tag{4.14}$$

and the inverse function $C^{-1}(\boldsymbol{x}_1, \boldsymbol{x}_2)$ is defined by

$$\int d^3x\, C^{-1}(\boldsymbol{x}_1, \boldsymbol{x}) C(\boldsymbol{x}, \boldsymbol{x}_2) = \delta_D(\boldsymbol{x}_1 - \boldsymbol{x}_2). \tag{4.15}$$

4.4 The non-Gaussian Fisher matrix

To examine the information content available in nonlinear data it is useful to construct the Fisher information matrix for parameters. One issue of interest is the flow of information about parameter values during nonlinear evolution. In one respect nonlinear evolution destroys information about initial conditions. But since information has to be preserved, it must inevitably be transported up the hierarchy of correlation functions. However nonlinear growth itself depends on

the detailed values of cosmological parameters. The question is does nonlinear evolution create or destroy parameter information?

To explore these questions three useful quantities can be defined: the entropy of the system,

$$S \equiv \langle \mathcal{L} \rangle = -\int d\rho \, \ln \rho, \tag{4.16}$$

which is the average log-likelihood evaluated at the true parameter values; the average gradient of the log-likelihood in parameter space,

$$\langle \mathcal{L}_i \rangle = -\int d\rho \, \partial_i \ln \rho = 0, \tag{4.17}$$

where ∂_i is the gradient in the i direction of parameter space, and is identically zero at the maximum likelihood values; and the Fisher information matrix, defined above, which quantifies our knowledge of a set of parameters,

$$\mathcal{F}_{ij} \equiv \langle \mathcal{L}_{ij} \rangle = -\int d\rho \, \partial_i \partial_j \ln \rho = \int d\rho \, (\partial_i \ln \rho)(\partial_j \ln \rho). \tag{4.18}$$

The parameter covariance matrix can be constructed from the Fisher matrix via

$$\boldsymbol{T} \equiv \langle \delta\boldsymbol{\theta}^t \delta\boldsymbol{\theta} \rangle = \boldsymbol{\mathcal{F}}^{-1}, \tag{4.19}$$

where $\delta\boldsymbol{\theta}$ is the displacement from the maximum likelihood point, $\delta\boldsymbol{\theta} = \boldsymbol{\theta} - \boldsymbol{\theta}'$.

4.4.1 Two-point correlations

For the case of a Gaussian PDF, a simple and familiar result may be derived for the Fisher information matrix. Since all higher order correlations are zero, $X = 0$. The Fisher matrix for Gaussian fields is therefore

$$\mathcal{F}_{0,ij} = -\int d\rho_0 \, \partial_i \partial_j \ln \rho_0. \tag{4.20}$$

The calculation is simplified if we choose the random field $\phi(\boldsymbol{x})$, to be the set of Fourier modes $\delta(\boldsymbol{k})$, where the covariance matrix is diagonal due to spatial invariance;

$$\begin{aligned} C(\boldsymbol{k}_1, \boldsymbol{k}_2) &= \langle \delta(\boldsymbol{k}_1) \delta(\boldsymbol{k}_2) \rangle \\ &= (2\pi)^3 P(k) \delta_D(\boldsymbol{k}_1 + \boldsymbol{k}_2). \end{aligned} \tag{4.21}$$

In this case the log-likelihood becomes

$$2\mathcal{L}_0 = \int \frac{d^3k}{(2\pi)^3} \frac{\delta(\boldsymbol{k}) \delta^*(\boldsymbol{k})}{P(k)} + V \int \frac{d^3k}{(2\pi)^3} \ln P(k), \tag{4.22}$$

where the second term is the normalisation factor modulo an unimportant constant term. Here the matrix relation $\ln\det \boldsymbol{C} = \mathrm{Tr}\ln \boldsymbol{C}$ was used before transforming to the continuum limit. For a finite volume survey the approximation $\delta_D(\mathbf{0}) = V$ was used, where V represents the survey volume. For a Gaussian distribution the Fisher matrix, equation (4.20), becomes

$$\mathcal{F}_{0,ij} = \frac{V}{2}\int \frac{d^3k}{(2\pi)^3}(\partial_i \ln P(k))(\partial_j \ln P(k)). \tag{4.23}$$

A similar expression to equation (4.23) was previously obtained by Tegmark (1997) using a different derivation.

4.4.2 Higher-order correlations

The non-Gaussian regime may be explored via the perturbed multivariate PDF, equation (4.10). The gradient of the log-likelihood $\langle \mathcal{L}_i \rangle$, is again identically zero, while the Fisher matrix becomes

$$\begin{aligned}\mathcal{F}_{ij} = &-\int d\rho_0\,(1-X)(\partial_i \ln\rho_0)(\partial_j \ln\rho_0)\\ &+2\int d\rho_0\, X_{(i}\partial_{j)}\ln\rho_0 - \int d\rho_0\, X_i X_j/(1-X).\end{aligned} \tag{4.24}$$

If the initial PDF is Gaussian, $\ln\rho_0$ is an even function of variables and X, given by equation (4.12), is odd. Expanding the last term this expression reduces to

$$\mathcal{F}_{ij} = \mathcal{F}_{0,ij} + \langle X_i X_j\rangle_G, \tag{4.25}$$

which is accurate up to X^4. The brackets $\langle\cdots\rangle_G$, denote averaging over the Gaussian distribution.

Again the analysis is simplified if one works in a Fourier representation, assuming spatial invariance. In this case the bivariance is

$$\begin{aligned}D(\boldsymbol{k}_1,\boldsymbol{k}_2,\boldsymbol{k}_3) &= \langle\delta(\boldsymbol{k}_1)\delta(\boldsymbol{k}_2)\delta(\boldsymbol{k}_3)\rangle_c\\ &= (2\pi)^3 B(\boldsymbol{k}_1,\boldsymbol{k}_2,\boldsymbol{k}_3)\delta_D(\boldsymbol{k}_1+\boldsymbol{k}_2+\boldsymbol{k}_3),\end{aligned} \tag{4.26}$$

which selects only those combinations of wavevectors that form closed triangles. The quantity $B(\boldsymbol{k}_1,\boldsymbol{k}_2,\boldsymbol{k}_3)$ will henceforth be referred to as the bispectrum.

With equations (4.21) and (4.26) the perturbation term, X, reduces to

$$X = \frac{1}{6}\int \frac{d^3k_1}{(2\pi)^3}\frac{d^3k_2}{(2\pi)^3}\,Q(\boldsymbol{k}_1,\boldsymbol{k}_2)\delta(\boldsymbol{k}_1)\delta(\boldsymbol{k}_2)\delta(-\boldsymbol{k}_1-\boldsymbol{k}_2), \tag{4.27}$$

where

$$Q(\boldsymbol{k}_1, \boldsymbol{k}_2) = \frac{B(\boldsymbol{k}_1, \boldsymbol{k}_2, -\boldsymbol{k}_1 - \boldsymbol{k}_2)}{P(k_1)P(k_2)P(|\boldsymbol{k}_1 + \boldsymbol{k}_2|)}. \tag{4.28}$$

This term derives from the ϕ^3-order term in the perturbation of the general PDF. The ϕ-order term vanishes under spatial invariance, since the bispectrum vanishes faster than the variance on large scales. This final constraint will always be true for a realistic PDF since the Jensen inequalities (Kendal & Stuart, 1969) state that

$$\langle x^a \rangle < \langle y^b \rangle^{a/b}, \tag{4.29}$$

where x is an arbitrary random variables and $a > b$ are real numbers. This implies that

$$\frac{\langle \delta^3 \rangle}{\langle \delta^2 \rangle} < \langle \delta^2 \rangle^{1/2}, \tag{4.30}$$

so that the ratio of the bispectrum to the power will always vanish faster than the variance.

The log-likelihood in the nonlinear regime is

$$\mathcal{L} = \mathcal{L}_0 + X + \frac{1}{2}X^2, \tag{4.31}$$

where $\mathcal{L}_0$ is the linear likelihood function (4.22), and X is given by (4.27). This expression can then be used to find the maximum likelihood values of parameters for systems in which the covariance matrix is close to diagonal.

The $\langle X_i X_j \rangle_G$ term in equation (4.25) is calculated making use of the cumulant expansion theorem to expand the 6-point correlation function into its connected parts. For the case of a Gaussian average only the two point terms are non-zero so that

$$\langle \delta_1 \delta_2 ... \delta_6 \rangle = \langle \delta_1 \delta_2 \rangle_c \langle \delta_3 \delta_4 \rangle_c \langle \delta_5 \delta_6 \rangle_c + \text{perms}. \tag{4.32}$$

Of these terms only six survive due to spatial invariance. Equation (4.32) essentially states that to the order we are working to, the covariance of bispectrum triangles is zero. Matarrese *et al.* (1997) , who use a Gaussian likelihood for the bispectrum, calculate the covariance matrix of the bispectrum to higher order and show that correlations between triangles appear through the pentaspectrum.

The non-Gaussian Fisher matrix can subsequently be written,

$$\begin{aligned} \mathcal{F}_{ij} &= \mathcal{F}_{0,ij} + \frac{V}{6} \int \frac{d^3k_1 \; d^3k_2}{(2\pi)^3 (2\pi)^3} Q_i(\boldsymbol{k}_1, \boldsymbol{k}_2) Q_j(\boldsymbol{k}_1, \boldsymbol{k}_2) \\ &\quad \times P(k_1) P(k_2) P(|\boldsymbol{k}_1 + \boldsymbol{k}_2|), \end{aligned} \tag{4.33}$$

where the subscripts i and j denote differentiation with respect to the parameters. This is the second major result of this chapter, and is independent of the nature of the non-Gaussianity, other than statistical spatial invariance of the field.

With equations (4.33) and (4.25) the question of information flow can now be addressed. Since the diagonal terms $\langle X_i^2 \rangle_G$ are positive, the addition of the bispectrum term can only add information. This is because the dominant effect, to this order, is the additional information brought by the higher-order moments. Nonlinear evolution will also change the shape of the PDF and degrade parameter information, but this is seen to be a higher-order effect.

4.5 The parameter entropy function

The Fisher information matrix provides a compact way of determining both marginal and conditional errors on a given set of parameters. However, in some circumstances it is useful to have more information about the detailed shapes of likelihood surfaces in parameter space. This may be achieved by generalising the definition of the entropy from §4.4 so that

$$S(\theta) = \langle \mathcal{L}(\theta) \rangle = -\int d\rho' \ln \rho, \tag{4.34}$$

where a prime denotes that a quantity is evaluated at its true (maximum likelihood) value. With this function one can map out the likelihood distribution of parameter space.

An advantage of the parameter entropy is that it can be calculated directly from the covariance and bivariance functions, without having to take parameter derivatives. This may be a noisy process if the spectra are generated numerically, *i.e.* directly from a Boltzmann solver. Noise in the Fisher matrix can spuriously break parameter degeneracies, and the entropy is one way to avoid this. Noise may also prevent the Fisher matrix from being positive definite, and hence unphysical. Strong correlations between parameters can also make the Fisher matrix ill-conditioned and numerically difficult to invert. The entropy clearly contains more information about the parameters and the shape of likelihood contours, which may be important for investigating degeneracies among parameters. Finally, the parameter entropy does not assume the parameter likelihood distribution is Gaussian, which is implicit in the Fisher matrix. A disadvantage of

the entropy is that evaluating the marginal parameter uncertainties can be difficult since the full distribution of S must be mapped out around its maximum in parameter space.

In the Gaussian case the entropy is given by

$$S_0 = -\int d\rho_0' \ln \rho_0. \tag{4.35}$$

In terms of the power spectrum this gives, up to an unimportant constant,

$$S_0 = \frac{V}{2}\int \frac{k^2 dk}{2\pi^2}\left(\frac{P'(k)}{P(k)} + \ln P(k)\right). \tag{4.36}$$

The nonlinear evolution of this quantity follows from the results of the last section. Expanding the non-Gaussian PDF as in equation (4.10) gives

$$S = S_0 + \int d\rho_0' X' \ln \rho_0 - \int d\rho_0' (1 - X') \ln(1 - X). \tag{4.37}$$

Again if ρ_0 is a Gaussian the second term in equation (4.37) vanishes. The final log term can be expanded to second order in X, $\ln(1-X) \approx -X - X^2/2$, yielding

$$S = S_0 - \langle XX' \rangle_G + \frac{1}{2}\langle X^2 \rangle_G. \tag{4.38}$$

This expression again simplifies using a Fourier representation and, with the results from the previous section, one finds

$$\langle X^2 \rangle_G = \frac{V}{6}\int \frac{d^3k_1}{(2\pi)^3}\frac{d^3k_2}{(2\pi)^3} Q^2(\boldsymbol{k}_1, \boldsymbol{k}_2) P'(k_1) P'(k_2) \times P'(|\boldsymbol{k}_1 + \boldsymbol{k}_2|) \tag{4.39}$$

and

$$\langle XX' \rangle_G = \frac{V}{6}\int \frac{d^3k_1}{(2\pi)^3}\frac{d^3k_2}{(2\pi)^3} Q(\boldsymbol{k}_1, \boldsymbol{k}_2) B'(\boldsymbol{k}_1, \boldsymbol{k}_2, -\boldsymbol{k}_1 - \boldsymbol{k}_2). \tag{4.40}$$

Equations (4.38), (4.39) and (4.40) are the third major new result of this chapter.

The parameter entropy evaluated at the maximum likelihood point, tells us about the order in the system and can be written

$$S = S_0 - \frac{1}{2}\langle X^2 \rangle_G, \tag{4.41}$$

where

$$S_0 = \frac{V}{2}\int \frac{k^2 dk}{2\pi^2} \ln P(k), \tag{4.42}$$

again up to an unimportant constant. In the case of gravitational instability, the power spectrum will always increase with time, so the linear entropy S_0, will also increase. As the field is Gaussian distributed, this corresponds to the maximum amount of disorder possible – that is the Gaussian requires the least information to specify it.

The effect of the non-Gaussian term in equation (4.41) always acts to *decrease* the entropy of the system, relative to the Gaussian case. While this may seem counter to our usual expectation that systems evolve towards higher entropy states, the effect of non-Gaussianity here introduces order, or structure, into the system, reducing the entropy.

4.6 Application to galaxy redshift surveys

To illustrate the effects of including higher-order statistics in the likelihood function it is useful to calculate the Fisher matrix and entropy for a simple analytic model. Since much can be derived from the nonlinear regime of galaxy redshift surveys, this is chosen as a suitable model, with application to the 2dF and Sloan Digital Sky Survey. Sufficient detail is included in the model so that it possesses most of the properties associated with galaxy redshift surveys. The random field of interest is therefore the biased, redshift space distorted mass density contrast $\delta^s = \delta n^s / n^s$.

Again, for simplicity, the analysis is performed in Fourier space. On large scales it is both more efficient and more accurate to exploit the natural symmetry of the survey and work in spherical harmonics (Heavens & Taylor, 1995; Tadros *et al.*, 1999; Taylor *et al.*, 2000). While this is important for linear analysis, it is not necessarily so for the nonlinear analysis. Nonlinear effects dominate on smaller scales where the Fourier representation can replace spherical harmonics to a high degree of accuracy. However, this simplification may begin to break down for the case where triangles of the bispectrum lead to the mixing of information from both large and small scales (see §4.7).

4.6.1 Gravitational instability

For a galaxy redshift survey, a major source of non-Gaussianity comes from non-linear evolution due to gravitational instability. For Gaussian initial conditions gravitational evolution may be modelled via perturbation theory. The skewness of the mass density field in perturbation theory is given by (Goroff *et al.*, 1986)

$$\begin{aligned} B(\boldsymbol{k}_1, \boldsymbol{k}_2, \boldsymbol{k}_3) &= (2\pi)^3[2J(\boldsymbol{k}_1, \boldsymbol{k}_2)P(k_1)P(k_2) + \text{cyc}(23, 13)] \\ &\quad \times \delta_D(\boldsymbol{k}_1 + \boldsymbol{k}_2 + \boldsymbol{k}_3), \end{aligned} \tag{4.43}$$

where

$$J(\boldsymbol{k}_1, \boldsymbol{k}_2) = 1 + \frac{1}{2}\mu_{12}\left(\frac{k_1^2 + k_2^2}{k_1 k_2}\right) + \kappa(\Omega_m)[\mu_{12}^2 - 1], \tag{4.44}$$

and where $\mu_{12} = \hat{\boldsymbol{k}}_1.\hat{\boldsymbol{k}}_2$. This expression can also be found from Fourier transforming the second-order perturbation solution discussed in chapters 2 and 3 (equation 2.11). The dependance of $J(\boldsymbol{k}_1, \boldsymbol{k}_2)$ on the density parameter is weak and comes in only through the function $\kappa(\Omega_m) = D_2/D_1^2 \approx -3/7\,\Omega_m^{-2/63}$, the ratio of first and second order growth functions (Peebles, 1980; Bouchet *et al.*, 1992). For simplicity the Einstein-de-Sitter value of $\kappa = -3/7$ (Bouchet *et al.*, 1992) is used.

The CDM-type model power spectrum is used, taking the form

$$\Delta^2(k) = \delta_H^2(k/H)^4 k^{n-1} T^2(k, h, \Omega_m), \tag{4.45}$$

where

$$\Delta^2(k) \equiv k^3 P(k)/2\pi^2 \tag{4.46}$$

and $T(k, h, \Omega_m)$ is the transfer function as given by (Bardeen *et al.*, 1986). The fiducial model has parameters

$$(\delta_H, h, \Omega_m, b_1, b_2) = (5 \times 10^{-5}, 0.65, 0.3, 0.002, 1, 0.5).$$

For simplicity spatial flatness ($\Omega = 1$) is assumed. Figure 4.1 shows the spectrum used for subsequent calculations.

4.6.2 Choosing bispectrum triangles

While the approach so far has been to retain as much information as possible, in practice it may not be possible to include all shapes of triangles in k-space due

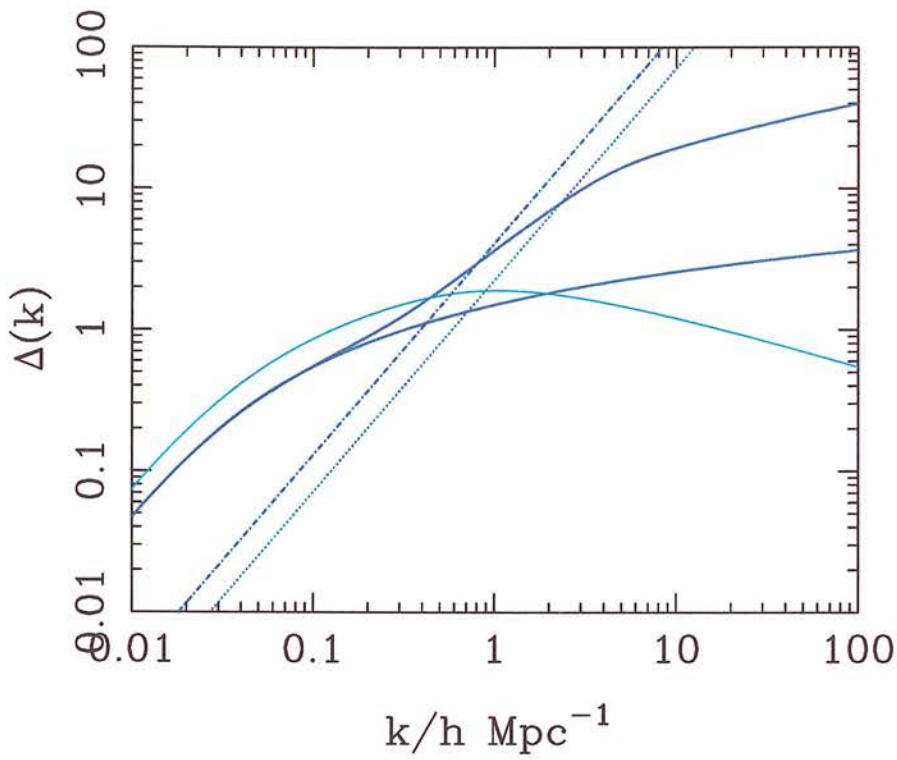

Figure 4.1: Fiducial matter power spectrum for a model galaxy redshift survey. The linear and nonlinear power in real-space (solid lines) are plotted alongside the angle averaged redshift power spectrum (light solid line) with small-scale damping included. The shot noise per mode for both of the model surveys are also plotted, see table 4.1; 2dF (dot-dash) and SDSS (dotted)

to CPU restrictions. It therefore makes sense to identify and study a subset of shapes that maximise the information content. This issue is discussed in more detail in §4.7. For simplicity only two distinct shapes are considered here: equilateral triangles and degenerate triangles. Degenerate triangles are constructed from two parallel wavevectors plus a third that is aligned anti-parallel with magnitude equal to the sum of the other two. A convenient subset of the degenerate category, and the configuration considered in this analysis, has the magnitude of the two smaller wavevectors being equal. Constraints are made by inserting an appropriate dimensionless operator into equations (4.33) and (4.38). For equilateral triangles we use:

$$\Delta_{\rm EQ} = \int \frac{d^3k}{4\pi}\, \delta_D(k_1 - k)\delta_D(k_2 - k)\delta_D(k_3 - k); \qquad (4.47)$$

whereas for the subset of degenerate (DG) triangles one possible constraint is

$$\Delta_{\rm DG} = \frac{1}{4}\int \frac{d\boldsymbol{k}}{4\pi}\delta_D(k_1 - k)\delta_D(k_2 - k/2)\delta_D(k_3 - k/2). \tag{4.48}$$

For the triangles of interest the bispectrum can be written

$$B(k) = \frac{12}{7}P^2(k) \qquad \text{Equilateral} \tag{4.49}$$

$$B(k) = 4P^2(k/2) - P(k/2)P(k) \qquad \text{Degenerate.} \tag{4.50}$$

The bispectra are plotted in figure 4.2, where the function

$$\Delta_B^2(k) \equiv \frac{k^3\sqrt{B(k)}}{2\pi^2} \tag{4.51}$$

is defined, which is useful to compare with $\Delta^2(k)$.

For an ideal, finite survey, in the absence of shot noise and redshift space distortions, the nonlinear Fisher matrix for equilateral triangles can conveniently be reduced to

$$\begin{aligned}\mathcal{F}_{ij} &= \frac{V}{2}\int\frac{k^2dk}{2\pi^2}\left[1 + \left(\frac{12}{7}\right)^2\frac{\Delta^2(k)}{6}\right] \\ &\quad\times [\partial_i \ln\Delta^2(k)][\partial_j \ln\Delta^2(k)].\end{aligned} \tag{4.52}$$

Similar expressions for the parameter entropy and for the case of degenerate triangles can be found in the appendix at the end of this chapter.

The effect of including nonlinear terms is two-fold. Firstly we see that the bispectrum introduces a second, positive term into the Fisher matrix, driving the parameter uncertainty down. In addition, the nonlinear correction to the likelihood allows one to push the wave-range to higher k, again driving down the uncertainty.

4.6.3 Poisson sampling of the density field

Assuming the measured galaxy population can be modelled as a random sampling of a smooth underlying field, the power- and bi-spectra transform according to

$$\begin{aligned}P(k) &\to P(k) + \frac{1}{n}, \\ B(\boldsymbol{k}_1, \boldsymbol{k}_2, \boldsymbol{k}_3) &\to B(\boldsymbol{k}_1, \boldsymbol{k}_2, \boldsymbol{k}_3) \\ &\quad + \frac{1}{n}[P(k_1) + P(k_2) + P(k_3)] + \frac{1}{n^2},\end{aligned} \tag{4.53}$$

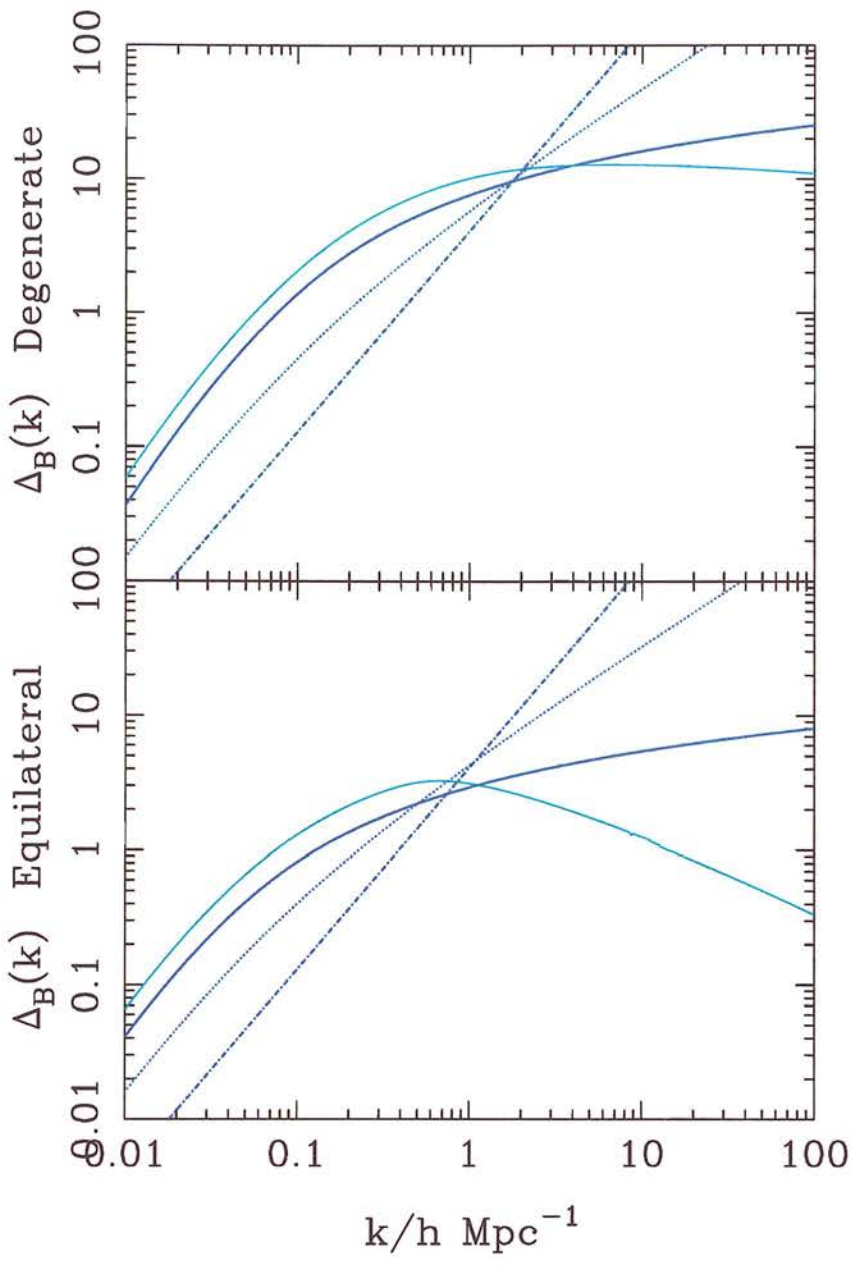

Figure 4.2: Fiducial bispectra for the redshift survey model for equilateral triangles (bottom panel) and degenerate triangles (top panel). The real space bispectra (heavy solid lines) are shown alongside the redshift space bispectra (light solid lines) with small scale damping. The $P(k)/n$ noise term (dotted) and the $1/n^2$ noise term (dot-dashed) are also shown for a 2dF-type survey.

where n is the mean number density of sources. If the noise varies across the survey, as is the case for flux-limited galaxy redshift surveys, this can be included

Survey	Mean Number Density (n)	Effective Volume (V)
2dF	3×10^{-3}	9×10^{7}
SDSS	10×10^{-3}	10×10^{7}

Table 4.1: Parameters for two model redshift surveys considered in this chapter.

in the models by the substitution $n = n(r)$ and $V \rightarrow \int d^3r$ in the Fisher and entropy estimates. The volume limited case is worked with here for simplicity and two models are considered, characterised by the number density n, and survey volume V, as given in Table 4.1. Noise levels for the surveys are plotted in Figures 4.1 and 4.2.

4.6.4 Bias and redshift space distortions

The use of redshift coordinates as radial distance introduces a distortion in the observed density field;

$$\delta^s(\boldsymbol{k}) = D(k\sigma\mu)(1 + \beta\mu^2)\delta(\boldsymbol{k}), \tag{4.54}$$

The factor $(1 + \beta\mu^2)$ is the linear effect, calculable from the transformation into redshift space as detailed in §4.6 (Kaiser, 1987). The factor $\beta = f_1(\Omega_m)/b_1$ and b_1 is the linear bias parameter. Small-scale effects giving rise to Fingers of God can be modelled by convolution of the density field with a random component along the line of sight (Peacock, 1992; Peacock & Dodds, 1994);

$$D(k\sigma\mu) = \frac{1}{\sqrt{1 + k^2\sigma^2\mu^2/2}}, \tag{4.55}$$

where $\mu = \hat{\boldsymbol{r}}.\hat{\boldsymbol{k}}$. Galaxy bias can be modelled by a local expansion of the density field (Fry and Gaztanaga 1993)

$$\delta_g = \sum_m \frac{b_m}{m!}\delta^m, \tag{4.56}$$

where the coefficients b_m are the bias parameters. The power spectrum for a biased, redshifted, and noisy galaxy survey is therefore

$$P_g^s(\boldsymbol{k}) = b_1^2 D^2(k\sigma\mu)(1 + \beta\mu^2)^2 P(k) + \frac{1}{n}. \tag{4.57}$$

Note that only the case of a deterministic bias is considered here, but this formalism can be easily generalised to include extra parameters for a stochastic biasing scheme (Pen, 1998; Dekel & Lahav, 1999).

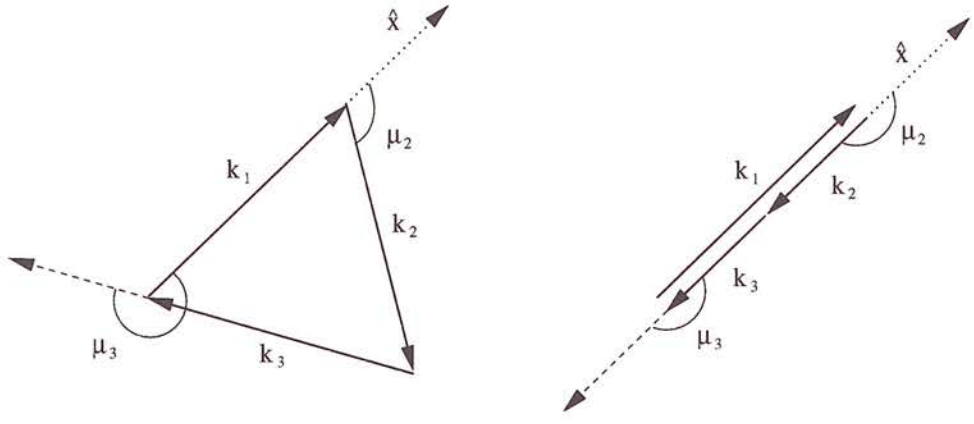

Equilateral Degenerate

Figure 4.3: Cartoon illustrating the definitions of the two types of triangle and showing how they line up in redshift space. The direction marked $\hat{\boldsymbol{x}}$ indicates the line of sight.

For equilateral triangles the angles between the line of sight and the wavevectors of the bispectrum triangles are (see figure 4.3)

$$\begin{aligned} \mu_1 &= \mu, \\ \mu_2 &= -\frac{1}{2}\mu + \frac{3}{2}\sqrt{1-\mu^2}, \\ \mu_3 &= -\mu_1 - \mu_2, \end{aligned} \tag{4.58}$$

where $\mu_i = \hat{\boldsymbol{r}}.\hat{\boldsymbol{k}}_i$. The corresponding redshifted bispectrum for equilateral triangles can be calculated using the machinery set out in (Heavens *et al.*, 1998; Verde *et al.*, 1998)

$$\begin{aligned} B_g^s(\boldsymbol{k}) &= D_2(k\sigma\mu)\Big[2b_1^3\mathrm{Ker}(k,\mu,\beta,b_1) + 3b_2(1+\beta+3/16\beta^2)\Big]P^2(k) \\ &\quad + \frac{1}{n}(D(k\mu_1)(1+\beta\mu_1^2)^2 + \mathrm{cyc})P(k) + \frac{1}{n^2}, \end{aligned} \tag{4.59}$$

where b_2 is the second-order bias term. The kernel $\mathrm{Ker}(k,\mu,\beta,b_1)$ is given by

$$\begin{aligned} \mathrm{Ker} &= 3\Big\{\frac{2}{7} + \frac{1}{4}\beta(9/7+b_1) + \frac{3}{112}\beta^2\Big[3-7b_1(2-b_1)\Big] \\ &\quad + \frac{1}{224}\beta^3\Big[\mu^2(3-4\mu^2)^2 + 7b_1(1-b_1^2)(9(1-\mu^2)+8\mu^4(3-2\mu^2))\Big] \\ &\quad - \frac{1}{256}\beta^4(b_1-1)(27-144\mu^2+384\mu^4-256\mu^6)\Big\}. \end{aligned} \tag{4.60}$$

The Finger of God effects are put in as for the power spectrum, in this case the

small scale damping factor is

$$D_2(k\sigma\mu) = \frac{1}{\sqrt{1+k^2\sigma^2\mu_1^2/2}}\frac{1}{\sqrt{1+k^2\sigma^2\mu_2^2/2}}\frac{1}{\sqrt{1+k^2\sigma^2\mu_3^2/2}} = \frac{1}{\sqrt{1+3/4k^2\sigma^2+9/64k^4\sigma^4+k^6\sigma^6\mu^2(3-4\mu^2)^2}}. \quad (4.61)$$

Similar expressions for degenerate triangles can be obtained. For the degenerate case the angles between the wavevectors of the bispectrum and the line of sight are

$$\begin{aligned}\mu_1 &= \mu,\\ \mu_2 &= -\mu,\\ \mu_3 &= -\mu.\end{aligned} \quad (4.62)$$

The redshifted bispectrum is then given by

$$\begin{aligned}B_g^s(\boldsymbol{k}) = {} & D_2(k,\mu)\Big[2b_1^3\mathrm{Ker}(k,\mu,\beta,b_1)+b_2b_1^2(1+\beta\mu^2)^2(2P(k)+P(k/2))\Big]P(k/2)\\ & +\frac{1}{n}b_1^2D_1(k,\mu_1)(1+\beta\mu_1^2)^2P(k)+\frac{1}{n}b_1^2D_1(k,\mu_2)(1+\beta\mu_2^2)^2P(k/2)\\ & +\frac{1}{n}b_1^2D_1(k,\mu_3)(1+\beta\mu_3^2)^2P(k/2)+\frac{1}{n^2},\end{aligned} \quad (4.63)$$

where in this case the kernel is

$$\begin{aligned}\mathrm{Ker} = {} & \frac{1}{2}\Big[4P(k/2)-P(k)\Big]+\frac{1}{2}\mu^2\Big[4(3+b_1)P(k/2)-3P(k)\Big]\beta\\ & +\frac{1}{2}\mu^4\Big[(4b_1-4b_1^2-3)P(k)+2(5b_1+b_1^2+6)P(k/2)\Big]\beta^2\\ & -\frac{1}{2}\mu^6\Big[(1-8b_1+8b_1^2)P(k)-4(1+b_1^2)P(k/2)\Big]\beta^3\\ & -b_1\mu^8\Big[(2-2b_1)P(k)+(1+b_1)P(k/2)\Big]\beta^4,\end{aligned} \quad (4.64)$$

and the damping term

$$D_2(k,\mu) = \frac{1}{\sqrt{(1+k^2\sigma^2\mu^2/8)(1+k^2\sigma^2\mu^2/2)}}. \quad (4.65)$$

The redshifted power and bi-spectra are shown in figures 4.1 and 4.2.

4.7 Results for a model galaxy redshift survey

4.7.1 Overview of parameter estimation

In this section the model outlined in §4.6, is applied to estimate parameter uncertainties from two model galaxy redshift surveys, based on the 2dF and

SDSS (see table 4.1 for survey parameters). The parameters of the model are $(h, \delta_H, \Omega_m, b_1, b_2)$, with fiducial values given in §4.6.1. The model enters the analysis via the redshifted galaxy power spectrum, equation (4.57), and the bispectrum for equilateral triangles, equation (4.59), and degenerate triangles, equation (4.63). These are used to estimate the function $Q(\boldsymbol{k}_1, \boldsymbol{k}_2, \boldsymbol{k}_3)$, given by equation (4.28), which is then used to calculate the nonlinear Fisher matrix, given by equations (4.33) and (4.23). The parameter entropy function is calculated from equations (4.36), (4.38), (4.39) and (4.40).

This section is laid out as follows. In §4.7.2 results are presented for the marginalised parameter uncertainties for the two surveys, as a function of the truncation wavenumber for the Fourier integrals. The basic result is that cosmological parameters may be estimated to accuracies of a few percent using redshift surveys independently of other measurements. In §4.7.3 correlation coefficients for all the parameters are shown, again as a function of wavenumber, illustrating that to second-order all of the degeneracies between parameters are lifted. An outline of how parameter estimation is improved using a simplified two-parameter model in §4.7.4. The relative information content of equilateral and degenerate triangles is explored in §4.7.5. We begin with an estimation of the parameter uncertainties from the full model.

4.7.2 Nonlinear parameter estimation from redshift surveys

Marginal errors may be obtained from inversion of the Fisher matrix so that the the 1σ error on parameter θ_i is approximately given by

$$\Delta\theta_i = \sqrt{(\boldsymbol{\mathcal{F}}^{-1})_{ii}}, \tag{4.66}$$

under the assumption that the likelihood distribution of parameters is roughly Gaussian. In figure 4.4 the results of the Fisher analysis are shown for the best attainable marginal uncertainties on the 5 independent parameters $\delta_H, h, \Omega_m, b_1$ and b_2 as a function of k. Here, and in subsequent figures, k is the maximum mode $k_{\rm max}$, in all integrations. A 5D joint estimation of parameter uncertainties with the Fisher matrix is only possible for a nonlinear likelihood since to linear order the Fisher matrix is singular due to degeneracies between parameters.

Results are given for two different redshift surveys, which are defined by the

volume of the survey V, and the mean number density of sources n. Formally this represents a volume-limited survey, but here effective values are used for a flux-limited sample. The volume and number density are chosen to resemble those of the 2dF redshift survey and the SDSS. The relevant parameters are found in Table 4.1.

Interestingly, the results show that the accuracy of the parameter estimation is similar for the 2dF and the SDSS, for all of the parameters out to quite high k. The reason for this is that the effective volumes of the two surveys are similar (see table 4.1), and the error scales like $1/\sqrt{V}$. Although the SDSS has a factor of ≈ 3 higher density of galaxies than the 2dF, this does not become important until the models become noise dominated per mode. From figures 4.1 and 4.2, it is seen that for both surveys, this is not until around $k = 1\,h\,\mathrm{Mpc}^{-1}$, well below the scale where the parameter estimation is valid.

Figure 4.4 (LHS) shows the marginalised uncertainties on the parameters δ_H, h and Ω_m. At $k = 0.1\,h\,\mathrm{Mpc}^{-1}$, normally the limit of linear analysis (Heavens & Taylor, 1995; Tadros *et al.*, 1999; Hamilton *et al.*, 2000), the predicted uncertainties lie around the $\approx 30\%$ level for both h and Ω_m. Estimates for δ_H, the horizon scale amplitude of matter perturbations, fare a little better at around 20%. Extending the analysis to $k = 0.3\,h\,\mathrm{Mpc}^{-1}$, near the limit of second-order perturbation theory, the uncertainty is found to fall by an order of magnitude to $\approx 2\%$ for all three parameters.

Figure 4.4 (RHS) also shows the marginalised parameter uncertainty for the bias parameters b_1 and b_2. For both surveys, truncated at $k = 0.1\,h\,\mathrm{Mpc}^{-1}$, it is found that b_2 is not detected at all, with b_1 detected at the $\approx 10\%$ level. However, if the analysis is pushed to $k = 0.3\,h\,\mathrm{Mpc}^{-1}$ the error on b_1 drops to around a percent, while b_2 is now measured to around 5% accuracy. While this looks encouraging for 2dF and the SDSS, a degree of caution should be urged in that a volume-limited survey has been assumed, with effective volume and noise levels chosen to mimic those of each survey. A more accurate assessment of the improved accuracy will require more detailed modeling and testing with N-body simulations, although the present study should provide a good indication of the measurement uncertainties.

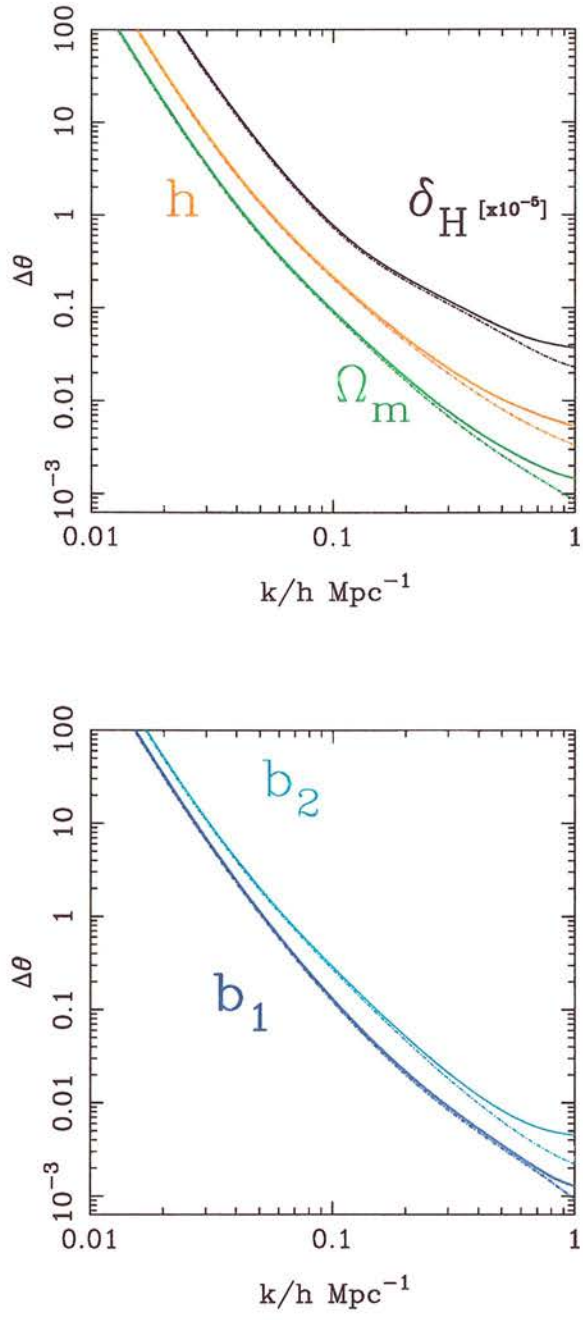

Figure 4.4: Marginalised error estimates on five parameters obtained from a Fisher analysis using the combined linear and nonlinear likelihood with equilateral and degenerate triangles. The results are shown for two sets of survey parameters resembling those of the 2dF (solid) and the SDSS (dot–dashed). Table 4.1 contains the survey parameters.

4.7.3 Lifting all the parameter degeneracies in redshift surveys

As well as the marginal uncertainties it is interesting to consider the correlations between parameters. The information about such correlations lies in the off-diagonal components of the Fisher matrix. Defining the correlation coefficient for parameters θ_i and θ_j as

$$r_{ij} = \frac{(\mathcal{F}^{-1})_{ij}}{\sqrt{(\mathcal{F}^{-1})_{ii}(\mathcal{F}^{-1})_{jj}}}, \tag{4.67}$$

one can quantify the degree of correlation as a function of maximum wavenumber. The results are plotted in figure 4.5 for all 10 of the correlation coefficients r_{ij}, in the 5D parameter space considered above. The indices on the correlation coefficients are given in table 4.2.

At low-k the Fisher matrix is dominated by the linear contribution to the likelihood and subsequently all of the parameters remain perfectly correlated/anti-correlated ($r_{ij} = \pm 1$). The reason for this is that in the linear regime, one can only measure the three composite parameters: $\beta = \Omega_m^{0.6}/b_1$, from redshift space distortions; $b_1\delta_H$ from the amplitude of linear galaxy clustering; and the spectral shape parameter, $\Gamma = \Omega_m h$, which determines the break scale in the matter power spectrum.

When the nonlinear terms begin to become important, at $k = 0.04\,h\,\mathrm{Mpc}^{-1}$, the r_{ij} deviate from ± 1 indicating the decoupling of the parameters. The reason for this universal removal of degeneracies lies in the lifting of the degeneracy between the bias parameters, b_1 and b_2. With a single triangle shape, one can only measure the combination $b_1/(1 + b_2/2J(\boldsymbol{k}_1, \boldsymbol{k}_2)b_1)$ (Matarrese *et al.*, 1997). With a second triangle shape this constraint is lifted. Figure 4.6 illustrates this, where the two degenerate likelihood contours for b_1 and b_2 are plotted for equilateral and degenerate triangles. The angle of intersection of these contours depends on the choice of triangles and is maximised by choosing very different shapes, motivating the choice of equilateral and degenerate triangles. With the bias degeneracy removed the degeneracies in β, Γ and $b_1\delta_H$ are all lifted.

While the parameters are no longer degenerate, many remain quite tightly correlated. The amplitude δ_H appears to become least correlated, becoming almost completely decoupled from the other four parameters. This is because to linear order it is only degenerate with b_1.

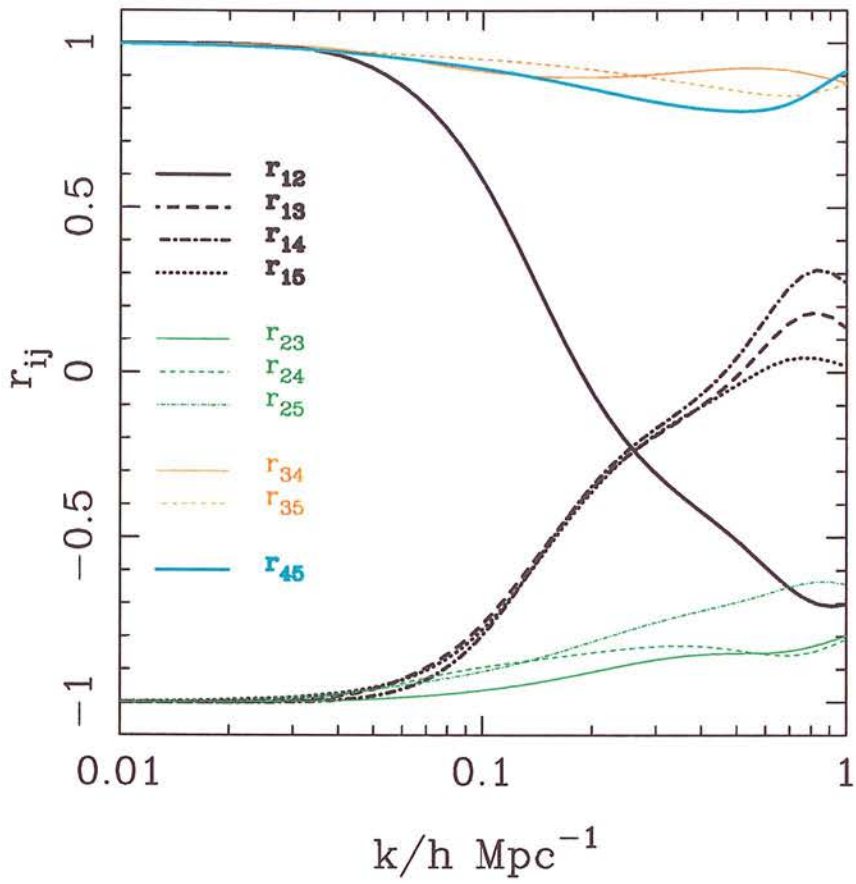

Figure 4.5: Correlation coefficients for every pair of parameters in the 5D marginalisation. The coefficients were calculated for the case of a 2dF-type survey and for a combined linear and nonlinear likelihood and both types of triangles. The key references table 4.2 for the index of each parameter.

As k gets larger, the r_{ij} coefficients begin to show deviations from a steady decline; in some cases this results in them actually growing larger. This occurs because the correlations between parameters ultimately depend upon shape and size of the 1-σ likelihood surface around its maximum. As this surface shrinks with increasing parameter information, it can change its shape, depending on the relative response to clustering information. This is what ultimately determines the correlation coefficient values.

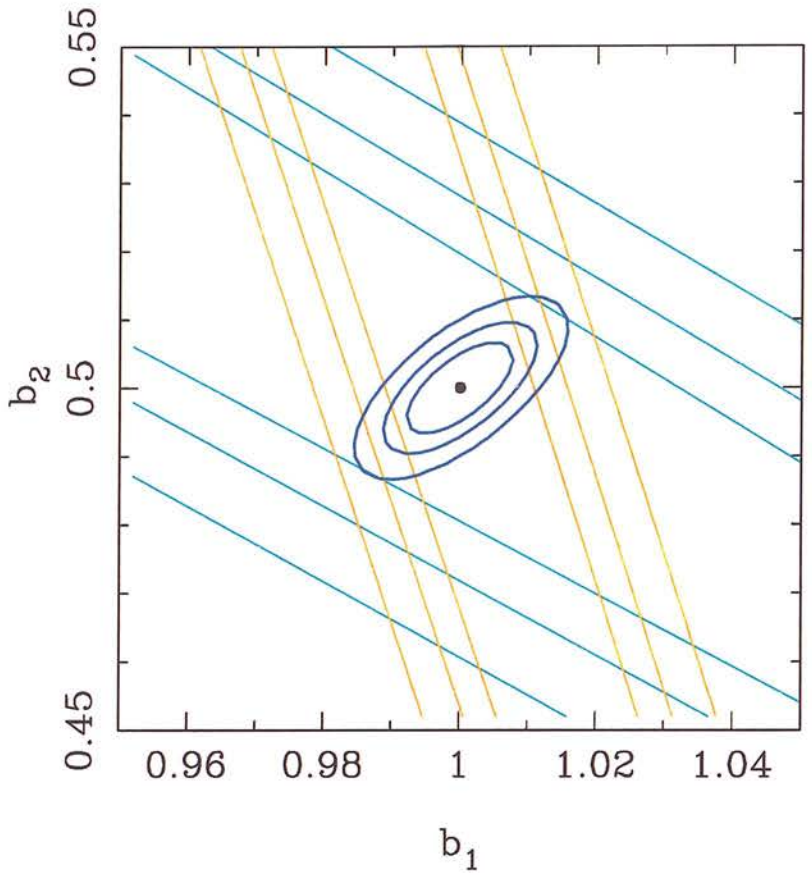

Figure 4.6: Lifting the degeneracy of the bias parameters using a combination of different triangle shapes for the bispectrum. The contours denote the 1, 2 and 3σ confidence regions for Gaussian entropy plus equilateral triangles and Gaussian plus degenerate triangles (faint lines) and for the combined effect (dark lines). The entropy has been marginalised over the amplitude δ_H. Redshift distortions have been ignored and the noise and volume are similar to those of the 2dF

index	parameter
1	δ_H
2	h
3	Ω_m
4	b_1
5	b_2

Table 4.2: Cosmological parameters and their index for the correlation coefficient.

4.7.4 A two-parameter model

While the Fisher matrix results show the value of including nonlinear effects in parameter estimation, it is useful to examine in some more detail how nonlinearity

increases parameter information. Rather than deal with all of the parameters, the analysis is restricted to just two. One is the linear bias factor b_1, whose measurement allows us to lift all the parameter degeneracies. The second is the parameter combination $\Gamma = \Omega_m h$. The advantage of restricting the analysis to these two parameters is that their Fisher matrix in the linear regime is not singular, and can be compared directly with the nonlinear regime. All other parameters are assumed to be known.

In figure 4.7 (top panel) the derivatives of the nonlinear, angle-averaged, redshifted function $Q(\boldsymbol{k}_1, \boldsymbol{k}_2)$, given by equation (4.28) are plotted with respect to each of the parameters. This effectively shows the information content of the modes, with respect to each parameter. Dark lines show the derivative with respect to Γ, while lighter ones with respect to b_1. Solid lines are for equilateral triangles, while dotted lines show the contribution from degenerate triangles. Figure 4.7 shows that degenerate triangles have a higher derivative, indicating that they contain more information that equilateral ones. This point shall be returned to in §4.7.5. The similarity of the shapes of the derivative also suggests that these parameters are strongly correlated.

Figure 4.7 (bottom panel) shows the marginal 1σ uncertainties on b_1 and Γ obtained from the Fisher analysis. It is immediately striking that inclusion of just a single triangle configuration has a significant effect on the errors. Even integrating out to relatively modest wavenumbers, $k \approx 0.2\,h\,\mathrm{Mpc}^{-1}$, there may be a 20 – 30 % reduction in the marginal uncertainty. This effect continues to grow as more modes are included. Using both triangle configurations has a much greater effect, reducing the errors by nearly an order of magnitude out at $k = 0.3\,h\,\mathrm{Mpc}^{-1}$.

In Figure 4.8 the entropy contours for a slice in the $b_1 - \Gamma$ plane are plotted, assuming the other parameters are known. The top-left plot shows the Gaussian contribution to the parameter entropy, where the maximum wavenumber is $k_{\mathrm{max}} = 0.2\,h\,\mathrm{Mpc}^{-1}$. The two parameters are highly correlated, and have uncertainties of $\Delta b_1 \approx 0.05$ and $\Delta\Gamma \approx 0.005$. The top-right plot show the effect of adding nonlinear information from equilateral triangles; a $\approx 30\%$ improvement. By adding only degenerate triangles to the Gaussian term, in the bottom left figure, the uncertainty reduces more dramatically. Finally, the bottom-right plot shows the combined effect of all of the terms.

Interestingly although the marginal errors are reduced, inclusion of the nonlinear

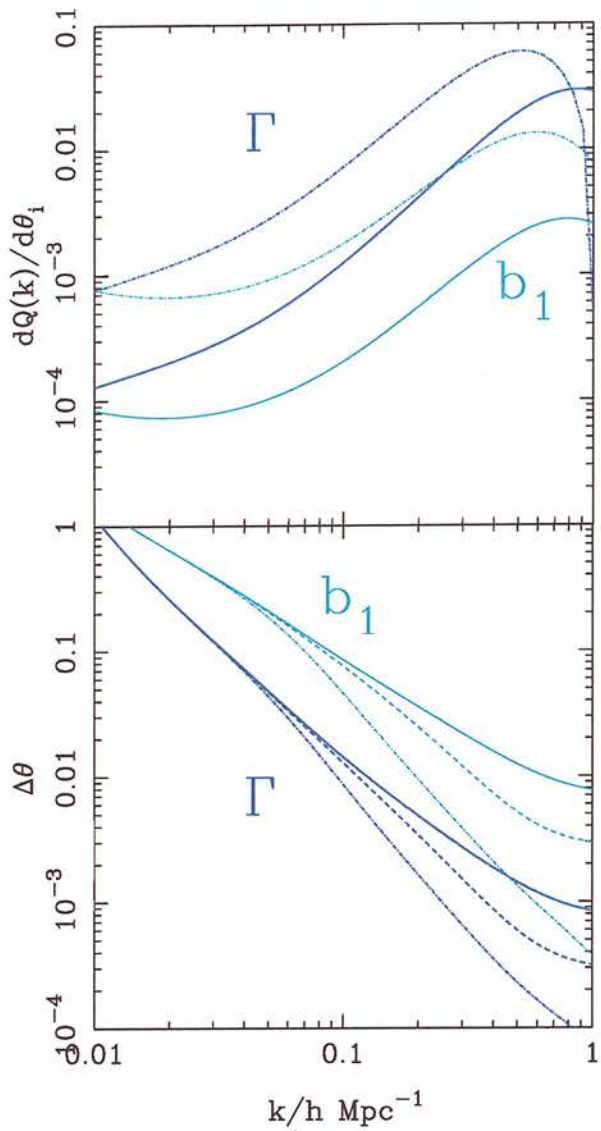

Figure 4.7: Parameter derivatives (top panel) and 1σ error levels for the joint estimation of b_1 and Γ in redshift space (bottom panel). The top panel shows the angle averaged derivative of the Q function from equation (4.28) for equilateral triangles (solid lines) and degenerate triangles (dotted lines) taken with respect to each of the parameters. The bottom panel shows the joint errors on the parameters when using the Gaussian likelihood (solid line), when adding in the contribution from equilateral triangles (dashed line) and when adding in both equilateral and degenerate triangles (dotted line). The survey parameters closely resemble those of the 2dF, as listed in table 4.1.

terms does not, in this case, make the two parameters b_1 and Γ become significantly less correlated, as suggested by the parameter derivatives in figure 4.7.

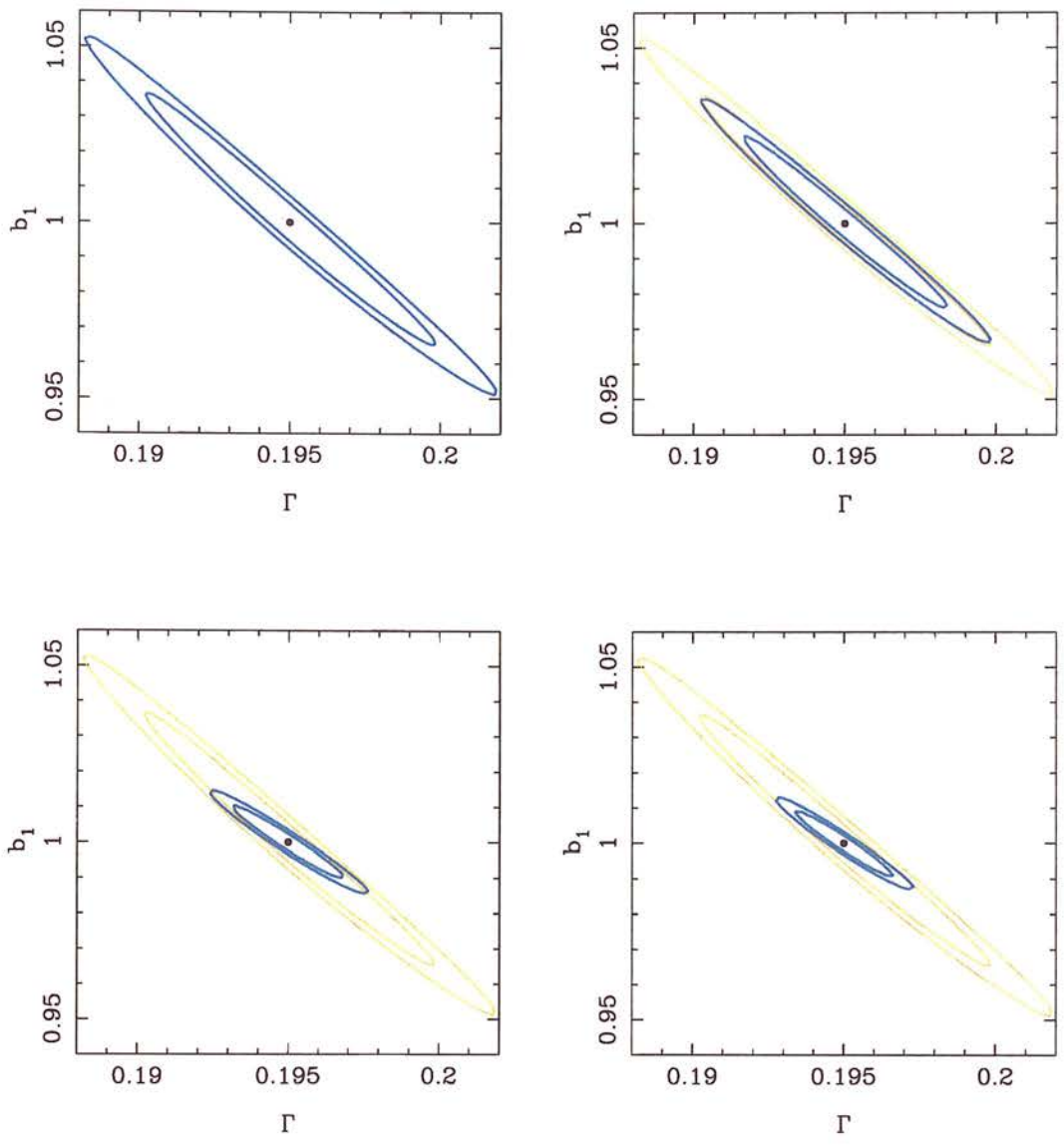

Figure 4.8: Entropy contours in the $b_1 - \Gamma$ plane. The contour levels correspond approximately to 1 and 2σ confidence limits. From top left to bottom right the plots show: the Gaussian entropy; the Gaussian entropy (light lines) and the contribution from equilateral triangles (dark lines); the Gaussian entropy (light lines) and the contribution from degenerate triangles; and the Gaussian entropy (light lines) with the sum of the contribution from the Gaussian part plus equilateral and degenerate triangles (dark lines). For all plots k_{max} was $0.2\,h\,\mathrm{Mpc}^{-1}$. The survey parameters closely resemble those of the 2dF.

This can also be seen from the entropy contours in figure 4.8 which are all rather elongated. The origin of this degeneracy is the effect both parameters have on

the power spectrum. The linear bias factor b_1, affects the amplitude of the power spectrum (ignoring its effects on redshift space distortions), while the shape parameter Γ shifts the break scale in wavenumber. If the power spectrum were a power-law, these effects would be degenerate. But since there is a break, this degeneracy is broken on scales below the break scale. Adding nonlinear information, while reducing the absolute error, does not reduce this correlation.

4.7.5 The information content of triangles

It is apparent from figures 4.6 and 4.7 that degenerate triangles seem to contain a great deal more information about cosmological parameters than equilaterals. As this result seems somewhat unintuitive, it is perhaps worth considering how the bispectrum triangles add information to the Fisher matrix.

The effect of different triangles can be partly understood from consideration of equation (4.33). For the non-Gaussian term, the Fisher matrix depends upon the derivatives of the function $Q(\boldsymbol{k}_1, \boldsymbol{k}_2)$ weighted by the product of $P(k_1)$, $P(k_2)$ and $P(|\boldsymbol{k}_1 + \boldsymbol{k}_2|)$. For equilateral triangles this factor is the cube of the power. However, for triangles where the magnitudes of the wavevectors are not equal, there is a mixing of power from different scales. This implies is that information contained in a given triangle configuration is related to the shape of the power spectrum. Although the parameter derivatives of $Q(\boldsymbol{k}_1, \boldsymbol{k}_2)$ are larger for degenerate triangles, indicating a larger information content (see figure 4.7), the power-weighting will ultimately determine which contributes the most information.

For monotonically rising $P(k)$, equilateral triangles are most significant because small scales (large k) contain most of the power. Conversely for power spectra that are decreasing functions of k, the maximum signal comes from large scales, hence for a given k_{max}, triangles that have a small side will give the most weight and provide the most information. In the CDM case the greatest power lies around the break scale, k_*. The result is therefore an admixture of the two competing effects; longwards of k_* the spectrum rises and equilateral triangles contain the most information, shortwards and it is triangles that contain a short side that win out. In the limit this means that for CDM there is a "maximal" triangle for parameter estimation that is degenerate, in the manner discussed in §4.6.2, with sides $k_*, k_{max}, k_{max} - k_*$. In practise, estimating parameters from degenerate triangles may be more difficult, as there will be fewer independent low-k modes

within finite survey volume.

4.8 Conclusions

A new method has been presented for including higher-order moments in the likelihood functions of cosmological fields in such a way that the parameter dependencies of the non-Gaussian terms may be used for estimating cosmological parameters. This non-Gaussian correction generalises likelihood analysis for application to fields that either contain intrinsic non-Gaussianity, or have become non-Gaussian due to nonlinear gravitational evolution. Such a generalisation is fundamentally important for cosmology since most of the interesting fields show non-Gaussian properties. The method has the advantage that the probability distribution of the field was dealt with explicitly, allowing the natural combination of linear and nonlinear regimes. In this respect the work differs significantly from existing techniques that separate out the nonlinear regime and apply a Gaussian PDF to the higher-order moments themselves (Matarrese *et al.*, 1997; Verde *et al.*, 1998), or that approximate the likelihood function using numerical simulations (Scoccimarro *et al.*, 1999; Scoccimarro *et al.*, 2000).

A general formalism was presented, for calculating the non-Gaussian Fisher matrix and the shape of the likelihood around its maximum, the parameter entropy function. A central result of this chapter has been to show that to lowest order, the dominant effect of adding nonlinearity, or more generally a non-Gaussianity, is to increase the the parameter information. This effect dominates over the degradation of parameter information due to the nonlinear evolution of the shape of the likelihood function.

Applying the analysis of nonlinearity to a simple model for a galaxy redshift survey, including the effects of shot noise, redshift space distortions and galaxy bias, it was found that nonlinear effects may be extremely useful for placing tight constraints upon cosmological parameters. Of crucial importance is the fact that even at second-order, degeneracies can be broken so that all of the cosmologically interesting parameters may be estimated independently. While going to higher-order may place tighter constraints on the nonlinear bias function through estimation of the series coefficients b_n, essentially redshift surveys offer up a great deal of their information without the need to turn to progressively more

intricate perturbative calculations. In addition, this analysis suggests that galaxy redshift surveys can be used in isolation to determine cosmological parameters. This greatly enhances their power as parameter estimation can be compared from independent surveys, such as the CMB, cosmic velocity fields and weak lensing surveys and combined further to reduce uncertainties.

The analysis relied upon a multivariate generalisation of the Edgeworth approximation for the probability distribution function. As such one should be careful to determine the range of applicability of second-order perturbation theory, and the series expansion of the likelihood function. It is well known from studies of 1-point distributions (Bernardeau & Kofman, 1995; Juszkiewicz *et al.*, 1995; Gaztañaga *et al.*, 2000; Taylor & Watts, 2000; Watts & Taylor, 2000) that the Edgeworth PDF has limitations – displaying unphysical features when the variance or skewness becomes too high. However, these effects do not automatically render the Edgeworth a bad approximation. Comparison with N-body simulations in redshift space (chapter 3 and Watts & Taylor 2000) has shown that peak of the distribution remains a good fit even when the extremities begin to behave badly. Fortunately it was found that a good deal of information comes from the nonlinear terms at relatively low-k and that the degeneracies between parameters are broken even for modest values of wavenumber. This is good news from a computational point of view as well since the number of modes available for analysis grows like k^3. While this is beneficial in some respects, it can also lead to computational problems if the number of modes gets too high. In this case data compression methods may need to be incorporated (Taylor *et al.*, 2000). An important future project would rigorously test the model of this chapter on N-body simulations in order to accurately determine the limitations, and address the specific issues associated with application to real datasets.

4.9 Appendix

In the absence of noise and redshift distortions the nonlinear Fisher matrix and entropy can be written in a particularly pleasing form. The Fisher matrix for equilateral triangles reduces to

$$\mathcal{F}_{ij} = \frac{V}{2}\int\frac{k^2dk}{2\pi^2}\left[1+\left(\frac{12}{7}\right)^2\frac{\Delta^2(k)}{6}\right][\partial_i \ln\Delta^2(k)][\partial_j \ln\Delta^2(k)], \qquad (4.68)$$

while the parameter entropy is given by

$$S = \frac{V}{2}\int \frac{k^2 dk}{2\pi^2}\left\{ \ln \Delta^2(k) + \frac{\Delta'^2(k)}{\Delta^2(k)} + \frac{1}{12}\left(\frac{12}{7}\right)^2 \Delta'^2(k)\left[\left(\frac{\Delta'^2(k)}{\Delta^2(k)}\right)^2 - \frac{2\Delta'^2(k)}{\Delta^2(k)}\right]\right\}. \tag{4.69}$$

For the case of degenerate triangles the Fisher matrix becomes

$$\begin{aligned}\mathcal{F}_{ij} &= \frac{V}{2}\int \frac{k^2 dk}{2\pi^2}\left\{\left[1 + \frac{8}{3}\frac{\left(\Delta^2(k/2)\right)^2}{\Delta^2(k)}\right][\partial_i \ln \Delta^2(k)][\partial_j \ln \Delta^2(k)]\right. \\ &\quad + \frac{1}{6}\Delta^2(k)\,[\partial_i \ln \Delta^2(k/2)][\partial_j \ln \Delta^2(k/2)] \\ &\quad \left. - \frac{32}{3}\Delta^2(k/2)\,\left(\partial_{[i} \ln \Delta^2(k/2)\,\partial_{j]} \ln \Delta^2(k/2)\right)\right\},\end{aligned} \tag{4.70}$$

and the parameter entropy is

$$\begin{aligned}S &= \frac{V}{2}\int \frac{k^2 dk}{2\pi^2}\left\{ \ln \Delta^2(k) + \frac{\Delta'^2(k)}{\Delta^2(k)} + \frac{1}{12}\Delta'^2(k/2)\left[\frac{\Delta'^2(k/2)\Delta'^2(k)}{[\Delta^2(k)]^2}\right.\right. \\ &\quad - \frac{1}{2}\frac{\Delta'^2(k/2)\Delta'^2(k)}{\Delta^2(k/2)\Delta^2(k)} + \frac{1}{16}\frac{\Delta'^2(k/2)\Delta'^2(k)}{[\Delta^2(k/2)]^2} - \frac{1}{2}\frac{\Delta'^2(k/2)}{\Delta^2(k)} \\ &\quad \left.\left. - \frac{1}{32}\frac{\Delta'^2(k)}{\Delta^2(k/2)} + \frac{1}{8}\frac{\Delta'^2(k/2)}{\Delta^2(k/2)} + \frac{1}{8}\frac{\Delta'^2(k)}{\Delta^2(k)}\right]\right\}.\end{aligned} \tag{4.71}$$

Chapter 5

Conclusions and further work

5.1 Summary and Conclusions

This thesis has addressed the effects of nonlinear evolution, bias and redshift distortions on the statistical properties of cosmic mass and galaxy density fields. The second and third chapters dealt with the 1-point probability distribution, the simplest member of the hierarchy of N-point distribution functions. The fourth chapter addressed the issue of parameter information flow in to the nonlinear regime by reconstructing the non-Gaussian likelihood function, essentially the N-point distribution of the field in the limit that N becomes very large.

Chapter 2 introduced a new calculation for the evolution of the 1-point distribution function for the mass density field. The calculation was based upon projection of the initial Gaussian distributions of linear fields, into the nonlinear regime using second order Eulerian perturbation theory and the Chapman-Kolmogorov equation. Comparison of the calculated PDF with N-body simulations and with other approximations yielded impressive results, indicating that second-order perturbation theory was able to provide a realistic description of the nonlinear density field so long as the variance was not pushed too far.

One advantage of the approach used in chapter 2 for reconstruction of the nonlinear PDF, was the ease with which it could be generalised. The formalism that was laid out could be extended to incorporate additional stochasticity in the transformation to the nonlinear regime. An application of this would be for the case where the bias between mass and galaxies was non-deterministic. This was discussed briefly in chapter 3. Additionally the Chapman-Kolmogorov approach

was able to allow for a range of probability distributions for the initial conditions. This matter was not pursued but remains an avenue for possible future work. Another issue that was not addressed was that of smoothing the final density field. In the perturbation theory approach, smoothing is implicit in the initial conditions in order to make the perturbation approximation valid. In reality, *i.e.* in simulations or for a real distribution of mass, nonlinearity in the density field can be smoothed away only after evolution under gravity. It is not clear how much of an effect this would make on the final PDF. A possible mechanism for including smoothing within the framework of the Chapman-Kolmogorov approach is discussed in Matarrese *et al.* (2000).

In chapter 3, the effect of redshift distortions and nonlinear galaxy biasing were incorporated into the 1-point PDF. The calculation exploited the relative simplicity of the method outlined in chapter 2. An analytical expression for the moment generating function was obtained first, allowing a straightforward calculation of the skewness in redshift space. This result differed slightly from a previous expression given by Hivon *et al.* (1995), although the discrepancy was not able to be traced. The skewness parameter and the the shape of the PDF itself were found to have a dependance on cosmological parameters. Most notably, the effect of second-order bias was quite pronounced, making the PDF appear sharply peaked with a rapid drop-off on the low density side of its maximum. A difference between the shapes of PDFs for models with constant $\beta = f/b_1$ was noted at second-order. It was proposed that this could be used to differentiate between different cosmological models in a real sample of galaxies.

The galaxy PDF was compared once again with N-body simulations for combinations of linear and nonlinear bias in real and redshift space. The second-order model was also compared with the Edgeworth expansion of the PDF, which made use of the calculation of the redshift space skewness. It was found that both models fitted the N-body data extremely well. Significant differences only occurred when the variance or skewness was pushed too high. For the Edgeworth expansion, unphysical "wiggles" dominated the low and high density tails of the distribution in some circumstances. This effect was associated with a breakdown in the series approximation. It was found to be most pronounced when the skewness was large, due to biasing, for example. In spite of these peculiar oscillations, the peak of the Edgeworth distribution remained a good fit to the simulations.

The work in chapter 4 addressed the issue of parameter information flow from the

linear to nonlinear regimes. This was investigated through the likelihood functions of general cosmic fields, the industry standard for estimating parameters from cosmological data sets. A problem with likelihood analysis is that it is routinely applied under the assumption that the multivariate probability distribution of the data is Gaussian, which is clearly a limiting approximation in cosmology. A major concern, and the principle motivation for this work, was that a great deal of information could be lost if the higher order moments were not integrated into the parameter estimation.

The likelihood functions for general non-Gaussian fields were constructed using a perturbative expansion of an arbitrary multivariate PDF, essentially a multivariate generalisation of the Edgeworth approximation. The parameter information contained within these distributions came in through the series of N-point correlation functions. Having developed the method up to the level of the 3-point correlation function, an example application was selected – the case of non-Gaussianity due to gravitational instability. A Fisher analysis was performed with the nonlinear likelihood on an analytical model for a galaxy redshift survey, demonstrating that higher order moments are indeed extremely important for estimating cosmological parameters accurately and independantly. It was found that all of the degeneracies between parameters in the model were broken when nonlinear terms were included to second-order. This allowed marginalised uncertainties of a few percent on parameters to be obtained when the survey characteristics were similar to those of the forthcoming 2dF or SDSS surveys. A significant dependance of the attainable errors on the shape of bispectrum triangles was also found.

5.2 Selected ideas for future work

Galaxy redshift surveys

This thesis has been entirely theoretically based. It therefore makes a great deal of sense to think about application of some of the new results to real data. Perhaps the most important application will be of the nonlinear likelihood analysis (as discussed in chapter 4) to galaxy redshift surveys. It was demonstrated that forthcoming surveys like the 2dF and SDSS, could be used to measure cosmological parameters down to the few percent level if nonlinear effects are taken into account. Existing surveys like the PSCz have so far been used to measure

parameters in the linear regime (Tadros *et al.*, 1999; Taylor *et al.*, 2000; Schmoldt *et al.*, 1999); it would be interesting to attempt the same in the nonlinear regime. Unfortunately the full data for both 2dF and SDSS will not be publicly available for some time. For this reason, application to existing data such as the PSCz first, would seem to be a wise thing to do; most of the developmental and adaptive work for application to data will be worked out prior to the release of the massive data sets.

From a general point of view, the important factor to consider is that estimation of a number of fundamental parameters may be made jointly only with the nonlinear likelihood function. An implication of this is that redshift surveys may, for the first time, be used independantly of other observations in order to constrain cosmological models. Furthermore, Fisher analysis has shown that the breaking of parameter degeneracies occurs at relatively modest cutoff scales in k. This is good news from a computational point of view since, in a Fourier representation, the number of modes available for analysis grows with k^3. While the additional modes may ultimately help to reduce error bars, the cost in terms of CPU time may begin to become prohibitive if too many are used. For the analysis of chapter 4 this is good news from a stability point of view as well; the Edgeworth series is known to break down if the field is smoothed at too high a k, as discussed above and in chapter 4.

Inevitably, however, computational problems are bound to arise in cosmology as smaller scales are probed and as data sets push towards the petabyte level. The long term answer, of course, lies with data compression. But the standard tools of this particular trade, for example Karhunen-Loève eigenvalue methods (Tegmark *et al.*, 1997; Vogeley & Szalay, 1996), have so far only been worked out and applied in the large-scale, Gaussian regime. Clearly there is a need to develop new methods for application of data compression methods to nonlinear data sets.

Highly nonlinear regime

A further outstanding problem remains in the exploration of the highly nonlinear regime. The work in this thesis has dealt with fields that are just starting to become nonlinear. The analysis in chapter 4 concentrated upon the extra information brought in by the 3-point correlation function without addressing the

change in shape of the PDF and power spectrum that occurs at higher order. There is undoubtedly a lot to be learnt from the highly nonlinear distribution of galaxies, in particular there is much to be learnt about biasing – a metaphor for our ignorance of galaxy formation. While in principle a perturbative approach to incorporating nonlinearities may work as one moves to higher order, the considerable difficulties arising from dealing with successively more intricate perturbation theory calculations make this a doubtful proposition.

A better approach may be to concentrate upon the 2-point function and on non-perturbative approximations such as the halo model (Seljak, 2000; Ma & Fry, 2000; Peacock & Smith, 2000). Within the halo model, the nonlinear power spectrum can be reconstructed with a remarkable degree of accuracy. One finds that the shape of the power spectrum on small scales is heavily dependant upon the properties of the halos. As an example of a robust nonlinear model for the mass distribution, the lognormal random field (Coles & Jones, 1991) is nicely complementary to this picture – it is completely specified by 2-point statistics whilst remaining an excellent fit to the distribution of gravitationally evolved systems. This was demonstrated in chapter 2, where it proved to provide an extremely good approximation to the 1-point PDF of numerical simulations even when the variance was quite large. Bernardeau & Kofman (1995) demonstrated that the lognormal is robust down to very small smoothing scales.

Using the halo model in conjunction with the lognormal approximation would therefore open up a range of interesting opportunities for delving into the highly nonlinear regime of gravitational clustering. There are exciting prospects here not only for measuring cosmological parameters but also for modelling and measuring the detailed properties of dark matter halos and the placement of galaxies within them.

Bibliography

Adler, R. J., 1981. *The geometry of random fields.* Wiley, Chichester.

Aldering, G., Perlmutter, S., Knop, R. A., Nugent, P., Goldhaber, G., Groom, D. E., Kim, M. Y., Pennypacker, C. R., Deustua, S., Quimby, R., Goobar, A., Pain, R., Fabbro, S., Hook, I. M., Lidman, C., Kim, A., Schaefer, B. E., Ellis, R., Irwin, M., Walton, N., Ruiz-Lapuente, P., Fruchter, A. S., Panagia, N., Supernova Cosmology Project Collaboration, 1998. In *American Astronomical Society Meeting*, volume 193, page 3904.

Alimi, J., Blanchard, A., Schaeffer, R., 1990, Ap. J. Lett., **349**, L5.

Amendola, L., 1996, MNRAS, **283**, 983.

Balbi, A., Ade, P., Bock, J., Borrill, J., Boscaleri, A., de Bernardis, P., Ferreira, P. G., Hanany, S., Hristov, V. V., Jaffe, A. H., Lee, A. T., Oh, S., Pascale, E., Rabii, B., Richards, P. L., Smoot, G. F., Stompor, R., Winant, C. D., Wu, J. H. P., 2000, astro-ph/0005124.

Balian, R., Schaeffer, R., 1989, Astron. Astrophys., **220**, 1.

Banday, A. J., Zaroubi, S., Górski, K. M., 2000, Ap. J., **533**, 575.

Bardeen, J. M., Bond, J. R., Kaiser, N., Szalay, A. S., 1986, Ap. J., **304**, 15.

Bernardeau, F., 1992, Ap. J., **392**, 1.

Bernardeau, F., 1994, Astron. Astrophys., **291**, 697.

Bernardeau, F., 1996, Astron. Astrophys., **312**, 11.

Bernardeau, F., 1998, Astron. Astrophys., **338**, 767.

Bernardeau, F., Kofman, L., 1995, Ap. J., **443**, 479.

Binney, J., Tremaine, S., 1987. *Galactic dynamics.* Princeton, NJ, Princeton University Press, 1987, 747 p.

Bond, J. R., Cole, S., Efstathiou, G., Kaiser, N., 1991, Ap. J., **379**, 440.

Bondi, H., Gold, T., 1948, MNRAS, **108**, 252.

Bouchet, F. R., Juszkiewicz, R., Colombi, S., Pellat, R., 1992, Ap. J. Lett., **394**, L5.

Bouchet, F. R., Strauss, M. A., Davis, M., Fisher, K. B., Yahil, A., Huchra, J. P., 1993, Ap. J., **417**, 36.

Bouchet, F. R., Colombi, S., Hivon, E., Juszkiewicz, R., 1995, Astron. Astrophys., **296**, 575.

Bower, R. G., Coles, P., Frenk, C. S., White, S. D. M., 1993, Ap. J., **405**, 403.

Burkert, A., 1995, Ap. J. Lett., **447**, L25.

Carlberg, R. G., Yee, H. K. C., Ellingson, E., Abraham, R., Gravel, P., Morris, S., Pritchet, C. J., 1996, Ap. J., **462**, 32.

Carroll, S. M., Press, W. H., Turner, E. L., 1992, Ann. Rev. Astron. Astrophys., **30**, 499.

Casimir, H. B. G., 1948, Proc. Kgl. Ned. Akad. Wet., **60**, 793.

Catelan, P., Lucchin, F., Matarrese, S., Moscardini, L., 1995, MNRAS, **276**, 39.

Coles, P., 1993, MNRAS, **262**, 1065.

Coles, P., Jones, B., 1991, MNRAS, **248**, 1.

Colless, M., 1998. In *Wide Field Surveys in Cosmology, 14th IAP meeting, Paris. Publisher: Editions Frontieres.*, page 77.

Colombi, S., 1994, Ap. J., **435**, 536.

Colombi, S., Bernardeau, F., Bouchet, F. R., Hernquist, L., 1997, MNRAS, **287**, 241.

Couchman, H. M. P., 1991, Ap. J. Lett., **368**, L23.

de Bernardis, P., Ade, P. A. R., Artusa, R., Bock, J. J., Boscaleri, A., Crill, B. P., De Troia, G., Farese, P. C., Giacometti, M., Hristov, V. V., Iacoangeli, A., Lange, A. E., Lee, A. T., Masi, S., Martinis, L., Mason, P. V., Mauskopf, P. D., Melchiorri, F., Miglio, L., Montroy, T., Netterfield, C. B., Pascale, E., Piacentini, F., Richards, P. L., Ruhl, J. E., Scaramuzzi, F., 1999, New Astronomy Review, **43**, 289.

de Lapparent, V., Geller, M. J., Huchra, J. P., 1986, Ap. J. Lett., **302**, L1.

de Sitter, W., 1930, Bull. Astron. Inst. Netherlands, **185**, 157.

Dekel, A., Lahav, O., 1999, Ap. J., **520**, 24.

Doroshkevich, A. G., Ryabenkin, V. S., Shandarin, S. F., 1973, Astrofizica, **9**, 257.

Eddington, A. S., 1930, MNRAS, **90**, 668.

Eddington, A. S., 1931, MNRAS, **92**, 3.

Efstathiou, G., Ellis, R. S., Peterson, B. A., 1988, MNRAS, **232**, 431.

Felten, G. E., Isaacman, R., 1986, Rev. Mod. Phys., **58**, 689.

Firmani, C., D'Onghia, E., Avila-Reese, V., Chincarini, G., Hernández, X., 2000, MNRAS, **315**, L29.

Fixsen, D. J., Cheng, E. S., Gales, J. M., Mather, J. C., Shafer, R. A., Wright, E. L., 1996, Ap. J., **473**, 576.

Flores, R. A., Primack, J. R., 1994, Ap. J. Lett., **427**, L1.

Friedmann, A., 1922, Z. Phys, **10**, 377.

Fry, J. N., 1984, Ap. J., **279**, 499.

Fry, J. N., 1985, Ap. J., **289**, 10.

Fry, J. N., 1994, Phys. Rev. Lett., **73**, 215.

Fry, J. N., Gaztañaga, E., 1993, Ap. J., **413**, 447.

Gamow, G., 1946, **70**, 572.

Gamow, G., 1949, **74**, 505.

Gaztañaga, E., 1992, Ap. J. Lett., **398**, L17.

Gaztañaga, E., 1994, MNRAS, **268**, 913.

Gaztañaga, E., Fosalba, P., Elizalde, E., 2000, Ap. J., **539**, 522.

Goroff, M. H., Grinstein, B., Rey, S. ., Wise, M. B., 1986, Ap. J., **311**, 6.

Gunn, J. E., 1995. In *American Astronomical Society Meeting*, volume 186, page 4405.

Guth, A. H., 1981, Phys. Rev. D, **23**, 347.

Guth, A. H., Pi, S. ., 1982, Phys. Rev. Lett., **49**, 1110.

Hamilton, A. J. S., 1985, Ap. J. Lett., **292**, L35.

Hamilton, A. J. S., 1998. In *The evolving universe*, page 185.

Hamilton, A. J. S., Tegmark, M., Padmanabhan, N., 2000, MNRAS, **317**, L23.

Hanany, S., Ade, P., Balbi, A., Bock, J., Borrill, J., Boscaleri, A., de Bernardis, P., Ferreira, P. G., Hristov, V. V., Jaffe, A. H., Lange, A. E., Lee, A. T., Mauskopf, P. D., Netterfield, C. B., Oh, S., Pascale, E., Rabii, B., Richards, P. L., Smoot, G. F., Stompor, R., Winant, C. D., Wu, J. H. P., 2000, astro-ph/0005123.

Harrison, E. R., 1970, Phys. Rev. D, **1**, 2726.

Hawking, S. W., 1982, Phys. Rev. Lett., **B115**, 339.

Heath, D. J., 1977, MNRAS, **179**, 351.

Heavens, A. F., Taylor, A. N., 1995, MNRAS, **275**, 483.

Heavens, A. F., Taylor, A. N., 1997, MNRAS, **290**, 456.

Heavens, A. F., Matarrese, S., Verde, L., 1998, MNRAS, **301**, 797.

Hivon, E., Bouchet, F. R., Colombi, S., Juszkiewicz, R., 1995, Ap. J., **298**, 643.

Hoyle, F., 1948, MNRAS, **108**, 372.

Hoyle, F., Szapudi, I., Baugh, C. M., 2000, MNRAS, **317**, L51.

Hu, W., 2000, Ap. J., **529**, 12.

Hu, W., Sugiyama, N., 1995, Phys. Rev. D, **51**, 2599.

Hu, W., Tegmark, M., 1999, Ap. J. Lett., **514**, L65.

Hubble, E., 1929. In *Proc. N.A.S.*, volume 15, page 168.

Hui, L., Kofman, L., Shandarin, S. F., 2000, Ap. J., **537**, 12.

Jungman, G., Kamionkowski, M., Kosowsky, A., Spergel, D. N., 1996, Phys. Rev. D, **54**, 1332.

Juszkiewicz, R., 1981, MNRAS, **197**, 931.

Juszkiewicz, R., Bouchet, F. R., Colombi, S., 1993, Ap. J. Lett., **412**, L9.

Juszkiewicz, R., Weinberg, D. H., Amsterfamski, P., Chodorowski, M., Bouchet, F., 1995, Ap. J., **442**, 39.

Kaiser, N., 1984, Ap. J. Lett., **284**, L9.

Kaiser, N., 1987, MNRAS, **227**, 1.

Kendal, M. G., Stuart, A., 1969. *"The Advanced Theory of Statistics, Vol. 2.* Griffin, London.

Kim, R. S., Strauss, M. A., 1998, Ap. J., **493**, 39.

Klypin, A., Kravtsov, A. V., Valenzuela, O., Prada, F., 1999, Ap. J., **522**, 82.

Kofman, L., Bertschinger, E., Gelb, J. M., Nusser, A., Dekel, A., 1994, Ap. J., **420**, 44.

Kolb, E. W., Turner, M. S., 1990. *The early universe.* Frontiers in Physics, Reading, MA: Addison-Wesley, 1990.

Lacey, C., Cole, S., 1993, MNRAS, **262**, 627.

Lahav, O., Rees, M. J., Lilje, P. B., Primack, J. R., 1991, MNRAS, **251**, 128.

Lange, A., Ade, P., Bock, J., Bond, J., Borrill, J., Boscaleri, A., Coble, K., Crill, B., de Bernardis, P., Farese, P., Ferreira, P., Ganga, K., Giacometti, M., Hivon, E., Hristov, V., Iacoangeli, A., Jaffe, A., Martinis, L., Masi, S., Mauskopf, P., Melchiorri, A., Montroy, T., Netterfield, C., Pascale, E., Piacentini, F., Pogosyan, D., Prunet, S., Rao, S., Romeo, G., Ruhl, J., Scaramuzzi, F., Sforna, D., 2000, astro-ph/0005004.

Lemaître, G., 1927. In *Ann. Soc. Sci. Bruxelles*, volume 47A, page 49.

Liddle, A. R., Lyth, D., 1993, Phys. Rep., **231**, 1.

Linde, A. D., 1990. *The physics of elementary particles and inflationary cosmology.* Moscow, Izdatel'stvo Nauka, 1990, 280 p. In Russian.

Loveday, J., Efstathiou, G., Peterson, B. A., Maddox, S. J., 1992, Ap. J. Lett., **400**, L43.

Ma, C., Fry, J. N., 2000, Ap. J. Lett., **531**, L87.

Martel, H., 1991, Ap. J., **377**, 7.

Martel, H., Freudling, W., 1991, Ap. J., **371**, 1.

Matarrese, S., Verde, L., Heavens, A. F., 1997, MNRAS, **290**, 651.

Matarrese, S., Verde, L., Jimenez, R., 2000, Ap. J., **541**, 10.

Meszaros, P., 1974, Astron. Astrophys., **37**, 225.

Mo, H. J., White, S. D. M., 1996, MNRAS, **282**, 347.

Moore, B., 1994, **370**, 629.

Moore, B., Ghigna, S., Governato, F., Lake, G., Quinn, T., Stadel, J., Tozzi, P., 1999, Ap. J. Lett., **524**, L19.

Mould, J. R., Huchra, J. P., Freedman, W. L., Kennicutt, R. C., Ferrarese, L., Ford, H. C., Gibson, B. K., Graham, J. A., Hughes, S. M. G., Illingworth, G. D., Kelson, D. D., Macri, L. M., Madore, B. F., Sakai, S., Sebo, K. M., Silbermann, N. A., Stetson, P. B., 2000, Ap. J., **529**, 786.

Moutarde, F., Alimi, J. ., Bouchet, F. R., Pellat, R., Ramani, A., 1991, Ap. J., **382**, 377.

Nusser, A., Dekel, A., Yahil, A., 1995, Ap. J., **449**, 439.

Peacock, J. A., 1992, MNRAS, **258**, 581.

Peacock, J. A., 1999. *Cosmological physics.* Cosmological physics. Publisher: Cambridge, UK: Cambridge University Press.

Peacock, J. A., Dodds, S. J., 1994, MNRAS, **267**, 1020.

Peacock, J. A., Heavens, A. F., 1990, MNRAS, **243**, 133.

Peacock, J. A., Smith, R. E., 2000, MNRAS, **318**, 1144.

Peebles, P. J. E., 1980. *"The large-scale structure of the universe".* Princeton University Press, Princeton N.J.

Peebles, P. J. E., 1999, Ap. J., **510**, 523.

Peebles, P. J. E., Yu, J. T., 1970, Ap. J., **162**, 815.

Pen, U., 1998, Ap. J., **504**, 601.

Penzias, A. A., Wilson, R. W., 1965, Ap. J., **142**, 419.

Press, W. H., Schechter, P., 1974, Ap. J., **187**, 425.

Primack, J. R., 2000. In *4th International Symposium on Sources and Detection of Dark Matter in the Universe, Marina del Rey, California, Feb 2000.*

Refregier, A., 1999. In *ASP Conf. Ser. 181: Microwave Foregrounds*, page 219.

Riess, A. G., Filippenko, A. V., Challis, P., Clocchiatti, A., Diercks, A., Garnavich, P. M., Gilliland, R. L., Hogan, C. J., Jha, S., Kirshner, R. P., Leibundgut, B., Phillips, M. M., Reiss, D., Schmidt, B. P., Schommer, R. A., Smith, R. C., Spyromilio, J., Stubbs, C., Suntzeff, N. B., Tonry, J., 1998, Astron. J., **116**, 1009.

Rocha, G., Magueijo, J., Hobson, M., Lasenby, A., 2000. astro-ph/0008070.

Rubin, V. C., Ford, W. K. J., 1970, Ap. J., **159**, 379.

Sachs, R. K., Wolfe, A. M., 1967, Ap. J., **147**, 73.

Schmoldt, I. M., Saar, V., Saha, P., Branchini, E., Efstathiou, G. P., Frenk, C. S., Keeble, O., Maddox, S., McMahon, R., Oliver, S., Rowan-Robinson, M., Saunders, W., Sutherland, W. J., Tadros, H., White, S. D. M., 1999, Astron. J., **118**, 1146.

Scoccimarro, R. ., Couchman, H. M. P., Frieman, J. A., 1999, Ap. J., **517**, 531.

Scoccimarro, R., Colombi, S., Fry, J. N., Frieman, J. A., Hivon, E., Melott, A., 1998, Ap. J., **496**, 586.

Scoccimarro, R., Feldman, H. A., Fry, J., Frieman, N., 2000. astro-ph/0004087.

Seljak, U., 2000, MNRAS, **318**, 203.

Seljak, U., Zaldarriaga, M., 1996, Ap. J., **469**, 437.

Sheth, R. K., Tormen, G., 1999, MNRAS, **308**, 119.

Silk, J., 1968, Ap. J., **151**, 459.

Smith, M. S., Kawano, L. H., Malaney, R. A., 1993, Ap. J. Suppl., **85**, 219.

Smoot, G. F., Bennett, C. L., Kogut, A., Wright, E. L., Aymon, J., Boggess, N. W., Cheng, E. S., de Amici, G., Gulkis, S., Hauser, M. G., Hinshaw, G., Jackson, P. D., Janssen, M., Kaita, E., Kelsall, T., Keegstra, P., Lineweaver, C., Loewenstein, K., Lubin, P., Mather, J., Meyer, S. S., Moseley, S. H., Murdock, T., Rokke, L., Silverberg, R. F., Tenorio, L., Weiss, R., Wilkinson, D. T., 1992, Ap. J. Lett., **396**, L1.

Starobinskii, A. A., 1979, ZhETF Pis ma Redaktsiiu, **30**, 719.

Starobinskii, A. A., 1982, Phys. Rev. Lett., **B117**, 175.

Stirling, A. J., Peacock, J. A., 1996, MNRAS, **283**, L99.

Strauss, M. A., Willick, J. A., 1995, Phys. Rep, **261**, 271.

Sunyaev, R. A., Zel'dovich, I. B., 1980, Ann. Rev. Astron. Astrophys., **18**, 537.

Sunyaev, R. A., Zel'dovich, Y. B., 1970, Astrophys. Space Sci., **7**, 20.

Szapudi, I., Szalay, A. S., Boschan, P., 1992, Ap. J., **390**, 350.

Szapudi, I., Meiksin, A., Nichol, R. C., 1996, Ap. J., **473**, 15.

Tadros, H., Ballinger, W. E., Taylor, A. N., Heavens, A. F., Efstathiou, G., Saunders, W., Frenk, C. S., Keeble, O., McMahon, R., Maddox, S. J., Oliver, S., Rowan-Robinson, M., Sutherland, W. J., White, S. D. M., 1999, MNRAS, **305**, 527.

Taylor, A., Ballinger, W., Heavens, A., Tadros, H., 2000. astro-ph/0007048.

Taylor, A. N., Hamilton, A. J. S., 1996, MNRAS, **282**, 767.

Taylor, A. N., Watts, P. I. R., 2000, MNRAS, **314**, 92.

Tegmark, M., 1997, Phys. Rev. Lett., **79**, 3806.

Tegmark, M., Taylor, A. N., Heavens, A. F., 1997, Ap. J., **480**, 22.

Tegmark, M., Eisenstein, D. J., Hu, W., de Oliveira-Costa, A., 2000, Ap. J., **530**, 133.

van de Weygaert, R., Bertschinger, E., 1996, MNRAS, **281**, 84.

van den Bosch, F. C., Swaters, R. A., 2000. astro-ph/0006048.

van Kampen, E., 2000. astro-ph/0008453.

van Kampen, N. G., 1992. *"Stochastic processes in physics and chemistry"*. North-Holland, Amsterdam.

Verde, L., Heavens, A. F., Matarrese, S., Moscardini, L., 1998, MNRAS, **300**, 747.

Viana, P. T. P., Liddle, A. R., 1996, MNRAS, **281**, 323.

Vishniac, E. T., 1983, MNRAS, **203**, 345.

Vogeley, M. S., Szalay, A. S., 1996, Ap. J., **465**, 34.

Wagoner, R. V., Fowler, W. A., Hoyle, F., 1967, Ap. J., **148**, 3.

Walker, T. P., Steigman, G., Kang, H., Schramm, D. M., Olive, K. A., 1991, Ap. J., **376**, 51.

Watts, P., Taylor, A., 2000. astro-ph/0006192.

Weinberg, S., 1972. *Gravitation and cosmology: Principles and applications of the general theory of relativity.* New York: Wiley, 1972.

White, S. D. M., 1979, MNRAS, **186**, 145.

White, S. D. M., Frenk, C. S., Davis, M., 1983, Ap. J. Lett., **274**, L1.

White, S. D. M., Davis, M., Frenk, C. S., 1984, MNRAS, **209**, 27P.

Wright, E. L., Meyer, S. S., Bennett, C. L., Boggess, N. W., Cheng, E. S., Hauser, M. G., Kogut, A., Lineweaver, C., Mather, J. C., Smoot, G. F., Weiss, R., Gulkis, S., Hinshaw, G., Janssen, M., Kelsall, T., Lubin, P. M., Moseley, S. H., Murdock, T. L., Shafer, R. A., Silverberg, R. F., Wilkinson, D. T., 1992, Ap. J. Lett., **396**, L13.

Zel'dovich, Y. B., 1970, Astron. Astrophys., **5**, 84.

Zel'dovich, Y. B., 1972, MNRAS, **160**, 1.

Zwicky, F., 1933, Helv. Phys. Acta, **6**, 110.